11-13-2009

Eulerian-Lagrangian Two Phase Debris Flow Model

Cora E. Martinez
Florida International University, cora.martinez@fiu.edu

DOI: 10.25148/etd.FI09121601

FLORIDA INTERNATIONAL UNIVERSITY

Miami, Florida

EULERIAN-LAGRANGIAN TWO PHASE DEBRIS FLOW MODEL

A dissertation submitted in partial fulfillment of the

requirements for the degree of

DOCTOR OF PHILOSOPHY

in

CIVIL ENGINEERING

by

Cora E. Martínez Franklin

2009

To: Dean Amir Mirmiran
College of Engineering and Computing

This dissertation, written by Cora E. Martínez Franklin, and entitled Eulerian-Lagrangian Two Phase Debris Flow Model, having been aproved in respect to style and intellectual content, is referred to you for judgment.

We have read this dissertation and recommend that it be approved.

_____
George Dulikravich

_____
Hector R. Fuentes

_____
Luis Prieto-Portar

_____
Francisco R. García-Martínez

_____
Fernando Miralles-Wilhelm, Major Professor

Date of Defense: November 13, 2009

The dissertation of Cora Martínez is approved.

_____
Dean Amir Mirmiran
College of Engineering and Computing

_____
Dean George Walker
University Graduate School

Florida International University, 2009

DEDICATION

To my loving husband, Romel, and our four beautiful daughters

ACKNOWLEDGMENTS

I would like to gratefully and sincerely thank Dr. Fernando Miralles-Wilhelm, for his guidance, understanding, patience, and most importantly, his friendship during my graduate studies. Dr. Miralles gave me the encouragement and opportunity to pursue my Ph.D. at FIU, and his continuous support helped me overcome many obstacles and finally finish this dissertation.

I wish also express my sincere appreciation and special thanks to Dr. Reinaldo Garcia, his guidance and assistance helped me improve my knowledge in the area of fluid mechanics and debris flows, and conducted me to the successful completion of this dissertation.

I would also like to express my deepest appreciation to the advisory committee members, Dr. Hector Fuentes, Dr. George Dulikravich, and Dr. Luis Prieto-Portar, for their support and genuine interest in refining this research.

I am very grateful to Dr. Fernando Miralles-Whihelm and to the Department of Civil & Environmental Engineering at FIU for fully funding my Ph.D. studies, and for allowing me to work as an Academic Advisor for the last two years, this contact with the students refreshed my mind and made me feel useful and productive.

I would also like to thank my fellow lab-mates and graduate students at the hydrologic lab at FIU, for their friendship and kind support, my special thanks go to Noemi González for her fruitful discussions and suggestions, which facilitated the opportunity for me to pursue this work.

I am also very grateful to many friends here in Miami who have helped me during these five years. I need to express my sincere thanks to many wonderful women that have

taken care of my kids many times; thanks to my first neighbors at the 113 path, thanks to the school moms, thanks to the swimming team moms, thanks to the gym team moms, thanks to my actual neighbors, thanks all of them for their friendship and understanding, you have been part of these journey.

A special thank-you goes to Efigenia Leon, who has been with me and my family for seven years. Without her help at home it would be completely impossible for me to finish this work, I cannot be more grateful for having Efi with us.

A penultimate gratitude is for my remarkable parents. They both have been a role model to me, for persistence and personal accomplishments; they deserve far more credit than I can ever give them.

Finally, I wish to thank my family; my four amazing daughters, Corina, Camila, Cristina and Carmen, for their unconditional love and infinite patient, I feel very proud of been your mom; and my devoted husband, Romel, for been the best father I could never imagine, thanks for bringing joy and happiness to our home every day, I am truly blessed and grateful for your unlimited love and support.

ABSTRACT OF THE DISSERTATION

EULERIAN-LAGRANGIAN TWO PHASE DEBRIS FLOW MODEL

by

Cora E. Martínez Franklin

Florida International University, 2009

Miami, Florida

Professor Fernando Miralles-Wilhelm, Major Professor

The main objective of this work is to develop a quasi three-dimensional numerical model to simulate stony debris flows, considering a continuum fluid phase, composed by water and fine sediments, and a non-continuum phase including large particles, such as pebbles and boulders. Large particles are treated in a Lagrangian frame of reference using the Discrete Element Method, the fluid phase is based on the Eulerian approach, using the Finite Element Method to solve the depth-averaged Navier–Stokes equations in two horizontal dimensions. The particle's equations of motion are in three dimensions. The model simulates particle-particle collisions and wall-particle collisions, taking into account that particles are immersed in a fluid. Bingham and Cross rheological models are used for the continuum phase. Both formulations provide very stable results, even in the range of very low shear rates. Bingham formulation is better able to simulate the stopping stage of the fluid when applied shear stresses are low. Results of numerical simulations have been compared with data from laboratory experiments on a flume-fan prototype. Results show that the model is capable of simulating the motion of big particles moving in the fluid flow, handling dense particulate flows and avoiding overlap among particles.

An application to simulate debris flow events that occurred in Northern Venezuela in 1999 shows that the model could replicate the main boulder accumulation areas that were surveyed by the USGS. Uniqueness of this research is the integration of mud flow and stony debris movement in a single modeling tool that can be used for planning and management of debris flow prone areas.

TABLE OF CONTENTS

LIST OF FIGURES

1 INTRODUCTION

1.1 Background

Debris flow is a frequent phenomenon in mountainous regions. It occurs when masses of poorly sorted sediments, rocks and fine material, agitated and mixed with water, surge down slopes in response to water flow and gravitational attraction. Modeling debris flows has gained increasing interest in recent years, due to the potential damage that these flows can generate, particularly in urbanized alluvial fans. However, hydrodynamic modeling of debris flow surges is much more challenging than that of water flows, mainly due to the multi-phase character of the flow, which includes not only water, but also a wide range of interacting solid particles, that goes from very fine sediments such as silt and clay, to large particles such as boulders; timber and other debris (see Figures 1 to 6). Many field observations attest to the heterogeneity of debris flows (Pierson 1986, Iverson 1997b).

As described by Pierson (1986), a typical surge of debris flow has a steep front or "head" with the densest slurry, the highest concentration of boulders and the greatest depth. This is followed by a progressively more dilute and shallower tail (Figure 1).

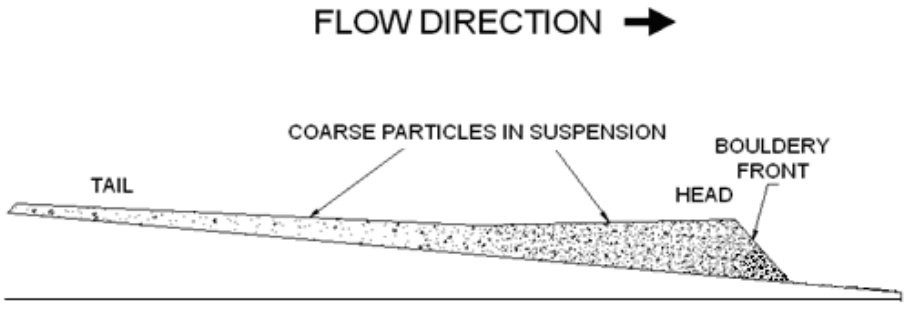

Figure 1. Schematic representation of a heterogeneous debris flow surge

In the dynamics of debris flow, both solid and fluid forces greatly influence the motion of the fluid-sediment mixture. This interaction of solid and fluid forces distinguishes debris flows from other similar environmental events, such as rock avalanches or water flows, where only solid grain forces or fluid forces dominate the physics, respectively. Interaction of solid and fluid forces not only distinguishes debris flows physically but also gives them an unique destructive power. Like avalanches of solids, debris flows can occur with little warning as a consequence of slope failure and can exert great impulsive impact loads on objects they encounter (Figures 2 and 3). Like water floods, debris flows are fluid enough to travel long distances on modest slopes and to inundate vast areas (Figure 4). Large debris flows can exceed 10^9 m^3 in volume and release more than 10^{16} J of potential energy, but even commonplace flows of 10^3 m^3 can denude vegetation, clog drainage ways, damage structures, and endanger humans (Iverson 1997b).

Figure 2. Building destroyed by debris flow; Vargas, Venezuela; December 1999 (Foto R. Garcia, 2000)

Figure 3. Debris flow deposits around a building, Vargas, Venezuela; December 1999 (Foto R. Garcia, 2000)(Foto R. Garcia, 2000)

To cite particularly catastrophic example, in December 1999, the northern coastal region of Venezuela suffered numerous debris flows, which were triggered by excess rainfall (close to 1000 mm in 3 days).The sediment volume mobilized was estimated in more than 2 $x10^7$ m^3 (Garcia and Lopez 2005), and was enough to inundate coastal communities, to generate severe property destructions, form a new coast line and cause close to 10000 deaths (Figures 2 to 6).

Figure 4. Buildings and houses partially buried by sediment in Caraballeda, Vargas, Venezuela; December 1999 (Foto R. Garcia, 2000)

Figure 5. Aerial view of Carmen de Uria alluvial fan, Vargas, Venezuela; December 1999 (Foto R. Garcia, 2000)

Figure 6. Front view of Carmen de Uria alluvial fan, Vargas, Venezuela; December 1999 (Foto R. Garcia, 2000)

Similar events happen frequently world wide, specially in the cities developed on steep alluvial fans.

Since debris flows are very dangerous natural hazards that affect humans and properties, the phenomenon has attracted the attention of scientists and engineers in recent years. Reviews presented by Coussot and Meunier (1996), and Iverson (1997b), exhaustively describe the physical aspects of debris flow motion and clearly divide previous debris flow research into two distinct categories. The first, based upon the pioneering work of Johnson (1965), assumes that debris flow behaves as a viscoplastic continuum. This model describes a single-phase material that remains rigid unless stresses exceed a threshold value: the plastic yield stress. Where stresses exceed the yield stress, material flows like a viscous fluid.

Various rheological models have been proposed, derived from experimental results or from theoretical considerations, such as the Bingham model (Bingham and Green 1919); Herschel-Bulkley model (Herschel and Bulkley, 1926); Coulomb-viscous model (Johnson 1970); biviscous model (Dent and Lang 1983); and quadratic model (O'Brien and Julien 1985). The Bingham plastic model is the most commonly used in practice. For slurry flows, such as silt-clay slurries, where viscous forces control the flow behavior, this kind of model has been used with reasonable accuracy.

The second approach has focus on the mechanics of granular materials. Based upon the findings of Bagnold (1954) and Takahashi (1978, 1980, 1981), two-phase models have been developed by several authors, such as Takahashi (1991), Iverson (1997a, 1997b) and Pitman and Le (2005). These models explicitly account for solid and fluid volume fractions and mass changes respectively. They include separate solid and

fluid stress tensors, which means that a constitutive relation must be defined for each phase. Finally, these models include a solid-fluid interaction force, which is not explicitly present in single-phase models. Recent investigations with gravel and sand mixtures demonstrate that this kind of grain-flow model is best applied to this type of flows (Parsons *et al*. 2001).

Despite of the considerable progress over the past few years, the flow dynamics and internal processes of debris flows are still challenging in many aspects. In particular, there are many factors related to the movement and interaction of individual boulders and coarse sediments that have not been fully addressed in previous works. In fact, there is a deficit on particle oriented models in comparison with many continuum models presented in the literature. Asmar *et al.* (2003) introduce the Discrete Element Method (DEM) to simulate the motion of solid particles in conjunction with the traditional Eulerian approach to model the liquid phase of debris flows. DEM is a numerical method to model dry granular flows where each particle is traced individually in a Lagrangian frame of reference by solving Newton's equation of motion. DEM is widely used now in diverse fields since Cundall and Strack published their first paper in 1979. However, extending DEM into two-phase flow is not straightforward. In this case it is necessary to include the fluid-particle momentum exchange and, when the particle volume is significant, it is important to model the particle volume fraction in both the momentum and continuity equations of the fluid.

1.2 Objectives

This thesis research describes the development of a quasi three-dimensional mathematical-numerical model to simulate stony debris flows, considering a continuum

fluid phase and large sediment particles, such as boulders, as a non-continuum phase. Large particles are treated in a Lagrangian frame of reference using DEM, and the fluid phase composed by water and fine sediments is modeled with an Eulerian approach using the depth-averaged Navier–Stokes in 2 dimensions. Particle' equations of motion are fully three-dimensional. The model includes the following features:

a) A capability to simulate the motion of big particles moving in the fluid flow.

b) Handling of dense particulate flows avoiding overlap among particles.

c) Use of different rheological models for the continuum fluid phase.

d) Modeling of formation of particle blockages and snout effects.

e) Modeling of particle-particle collisions and wall-particle collisions, taking into account that particles are immersed in fluid.

The model is tested with analytical results found in the literature and with laboratory experiments. This work also illustrates the application of the model to a real mud and debris flow event.

2 LITERATURE REVIEW

2.1 Homogeneous Models

In spite of the existence of particles, the mixture of debris flows is usually treated in a simplified manner, as the movement of a continuum (O'Brien and Julien 1998, Phillips and Davies 1991, Coussot and Piau 1994). For slurry flows, where the fluid matrix is a poorly sorted mixture of clay, silt and sand, and dispersive effects of the sand-sized sediment are minor in comparison to the cohesive properties of silt and clay, the assumption of a homogeneous model is often appropriate. As viscous forces control the flowing behavior of slurries, the primary assumption is that the continuous matrix is responsible for the yield strength and viscous behavior, whereas interparticle and particle-fluid interactions are ignored. In these cases, visco-plastic rheological models can reflect properly the constitutive relationship of this kind of flows.

In general, the extent of debris flows is most predominant than the depth in scale, and translation is most predominant than rotation. Therefore, it is reasonable to assume that the governing equations, mass continuity and momentum, can be integrated along the depth. In a fixed Cartesian coordinate system (x,y,z) with z pointing upward opposite to the direction of gravity, the governing equations can be reduced to depth-averaged relationships in the x-y plane.

Continuity equation:

$$\frac{\partial H}{\partial t}+\frac{\partial(\bar{u}H)}{\partial x}+\frac{\partial(\bar{v}H)}{\partial y}=0 \tag{1}$$

Momentum equations:

$$\frac{1}{g}\frac{\partial \overline{u}}{\partial t}+\frac{\overline{u}}{g}\frac{\partial \overline{u}}{\partial x}+\frac{\overline{v}}{g}\frac{\partial \overline{u}}{\partial y}+\frac{\partial \eta}{\partial x}+S_{fx}=0 \tag{2}$$

$$\frac{1}{g}\frac{\partial \overline{v}}{\partial t}+\frac{\overline{u}}{g}\frac{\partial \overline{v}}{\partial x}+\frac{\overline{v}}{g}\frac{\partial \overline{v}}{\partial y}+\frac{\partial \eta}{\partial y}+S_{fy}=0 \tag{3}$$

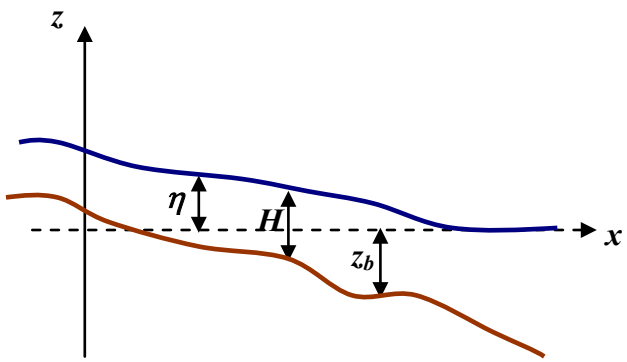

Figure 7. Free surface flow profile down a slope

where x and y are the horizontal coordinates, t is the time, η is the free-surface elevation, H is the water depth, z_b is the bottom elevation; $\eta=H+z_b$ (see Figure 7), $\overline{u}$ and $\overline{v}$ are the vertically averaged velocities in x and y directions respectively, g is the gravitational acceleration and S_{fx} and S_{fy} are the depth integrated stress terms that depend on the rheological model to be used (see Appendix A for derivation of these terms when two different rheological formulations are used).

2.2 Rheological Models

Bingham and Green (1919) proposed one of the pilot rheological models for visco-plastic materials experimenting with paint. They found the paint to be plastic and had a finite yield stress value that must be exceeded prior to motion. Various slurry flows commonly encountered in nature have shown to have a similar behavior and they have been represented with reasonable accuracy by the Bingham model (Wildemuth and Williams 1985; Mainali and Rajaratnam 1994). The material is assumed to exhibit a linear stress-strain relationship with the applied shear stress as follows

$$\tau = \begin{cases} 0 \quad if \quad \tau < \tau_y \\ \tau_y + \mu\dot{\gamma} \quad if \quad \tau \geq \tau_y \end{cases} \tag{4}$$

where τ is the shear stress, τ_y is the yield stress, μ is the viscosity and $\dot{\gamma}$ is the shear rate.

Besides the Bingham model, there are other rheological models that can represent with accuracy slurry flows. It has been found that yielded mud may experience shear thinning (Wan 1982, O'Brien and Julien, 1988), i.e. its viscosity decreases gradually with the increase of shear rate. Muds with high solid concentrations generally experience more severe shear thinning than those with low solid concentrations, then in those cases a Herschel-Bulkley model (Herschel and Bulkley, 1926) seems to be more appropriate in depicting this particular behavior. The stress-strain relationship is nonlinear, commonly showing convexity to the shear stress

$$\tau = \begin{cases} 0 \quad if \quad \tau < \tau_y \\ \tau_y + K\dot{\gamma}^m \quad if \quad \tau \geq \tau_y \end{cases} \tag{5}$$

where K and m are empirical parameters . For natural mud suspensions, m approaches 1/3 (Coussot, 1997).

For highly concentrated sediment-water mixtures, where interparticle friction is not negligible, Johnson (1970) proposed a modification of the Bingham model. He divided the yield strength of the Bingham model into cohesion and friction components and developed the Coulomb-viscous model

$$\tau = \begin{cases} 0 \quad if \quad \tau < \tau_y \\ \tau_y + \mu\dot{\gamma} \quad if \quad \tau \geq \tau_y \end{cases} \tag{6}$$

with

$$\tau_y = \tau_{yc} + \sigma_n \tan\phi \tag{7}$$

where the value of the rheological parameters: the cohesive yield stress τ_{yc} , the normal stress σ_n, the internal friction angle ϕ, and the viscosity μ, vary with mixture properties such as solid concentration, clay type, particle shape and size distribution.

Other rheological model that takes into account dispersive stresses was proposed by O'Brien and Julien (1985). Using basic fluid mechanics principles to describe hyperconcentrated flows, they postulated a quadratic model covering yield stress, viscous stress, dispersive stress and turbulent stress as

$$\tau = \begin{cases} 0 & if \quad \tau < \tau_y \\ \tau_y + \mu\dot{\gamma} + \zeta\dot{\gamma}^2 & if \quad \tau \geq \tau_y \end{cases} \tag{8}$$

where ζ is the inertial shear-stress coefficient.

Later, based on laboratory experiments, O'Brien and Julien (1988) found the viscosity and yield stress to be functions of the volumetric sediment concentration $\bar{c}$ of silts, clays, and in some cases, fine sands. The following exponential relationships were proposed

$$\mu = \alpha_1 e^{\beta_1 \bar{c}} \tag{9}$$

$$\tau_y = \alpha_2 e^{\beta_2 \bar{c}} \tag{10}$$

in which α_1, β_1, α_2 and β_2 are empirical coefficients defined by experimentation for some known mixtures. For water–clay mixtures the following coefficients are commonly used: $\alpha_1 = 0.621 \times 10^{-3}$, $\beta_1 = 17.3$, $\alpha_2 = 0.002$ and $\beta_2 = 34.2$. Units are *Pa.s* for viscosity and *Pa* for yield stress (O'Brien and Julien, 1988).

Many authors have proposed Bingham, Herschel-Bulkley or quadratical models to simulate debris flow. However, all these models, as they have been proposed, assume a critical or yield shear stress that may create instabilities in model applications. For close to zero shear rates, these models have a viscosity discontinuity where it changes from a finite value to infinity, that constitutes a phase change where the initially liquid fluid becomes a solid, rendering the fluid governing equations invalid. The biviscous model and the Cross rheological formulation do not present such as discontinuity.

When using the Cross model the relationship between stress and shear rate is simply

$$\tau = \mu_{eff}\dot{\gamma} \tag{11}$$

where μ_{eff} is the effective viscosity, a continuous variable that changes from a large value at very low shear rates to the fluid dynamic viscosity at higher shear rates.

The general Cross model gives viscosity as a function of shear rate as (Barnes *et.al,*. 1989):

$$\mu_{eff} = \mu_{\infty} + \frac{\mu_0 - \mu_{\infty}}{1 + (K_B\dot{\gamma})^m} \tag{12}$$

where μ_0 and μ_{∞} are viscosity at very low and very high shear rates, respectively, and K_B and m are constants parameters. The effective viscosity can be conveniently defined in terms of the Bingham fluid parameters (yield stress and dynamic viscosity) as it is proposed by Shao and Lo (2003). Taking m as unity the effective viscosity can be rewritten as:

$$\mu_{eff} = \frac{\mu_0 + \mu_{\infty}K_B\dot{\gamma}}{1 + K_B\dot{\gamma}} \tag{13}$$

$$\text{with } K_B = \frac{\mu_0}{\tau_y}, \mu_{\infty} = \mu \text{ and } \mu_0 = 10^3\mu \tag{14}$$

When considering the biviscous model, as described by O'Donovan and Tanner (1984), stress in the fluid can be described as

$$\tau = \begin{cases} \mu_0 \dot{\gamma} & if \quad \tau < \tau_y \\ \tau_y + \mu \dot{\gamma} & if \quad \tau \geq \tau_y \end{cases} \tag{15}$$

Which is a linearization of the Cross model. See Figure 8 for comparison of the rheological models mentioned above.

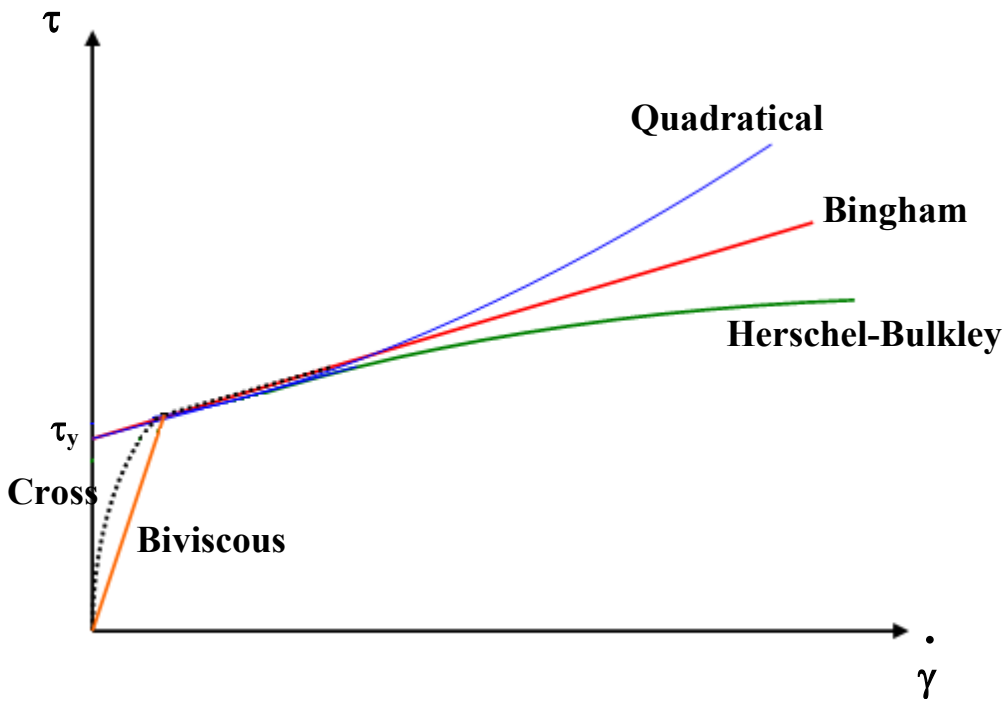

Figure 8. Comparison of different flow rheological models

2.3 Non-Homogeneous Models

Grain-flow models, based on the physics of grain-grain and grain-fluid interactions, are a different type of model to describe debris flows which are friction-dominated grain flows and behave differently than mud-slurry flows.

When talking about *granular mass flows*, the word "granular" highlights the importance of momentum transport by large solid grains, mixed with less dense

intergranular fluid. The word "mass" implies that a finite, contiguous body of solid and fluid moves almost in unison, and the word "flow" indicates that the grain-fluid body deforms irreversibly as it moves downslope (Iverson and Vallance, 2001).

High volumetric grain concentrations distinguish granular mass flows from phenomena such as slurry-mud flows. Particles that are silt-sized and smaller can be viewed as part of the fluid (slurry), larger particles constitute the granular solids and the concentration of these large particles partially defines the kind of flow regime, which can be friction-dominated or collision- dominated (see Figure 9).

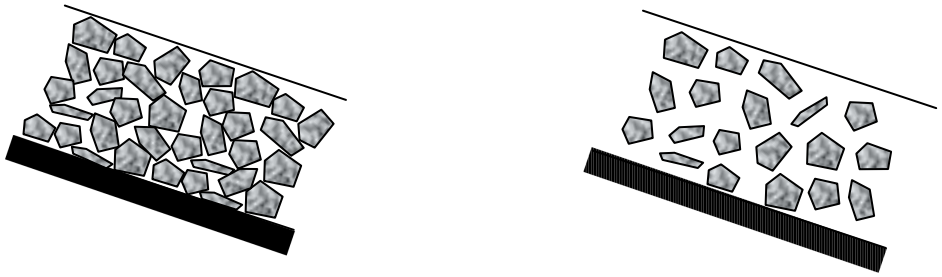

(a) **(b)**

Figure 9. Schematic cross sections of gravity driven flows down inclined planes. (a) Friction-dominated flow (b) Collision-dominated flow.

A numerical criterion, identified by Savage (1984), distinguishes flow regimes on the basis of a dimensionless parameter, N_s, that characterizes stresses in steady, uniform flows

$$N_s = \frac{\rho_s \dot{\gamma}^2 d^2}{(\rho_s - \rho_f) g H} \tag{16}$$

where ρ_s and ρ_f are the mass densities of the solid grains and fluid, respectively, $\dot{\gamma}$ is the bulk (continuum) shear rate, d is the grain diameter, g is the gravitational acceleration and H is the flow depth. Roughly, N_s represents the ratio of grain collision stresses to gravitational grain contact stresses that produce intergranular friction. On the basis of diverse data, Savage and Hutter (1989) inferred that if $N_s > 0.1$, grain collision stresses may affect flow dynamics significantly. For those flows with small values of N_s (friction dominated) Iverson and Denlinger (2001) suggest that the Coulomb (1776) friction equation with zero cohesion is the best model for describing stresses in granular mixtures:

$$\tau = \sigma \tan \phi \tag{17}$$

where τ is the intergranular shear stress, σ is the total compressive normal stress and ϕ is the intergranular Coulomb friction angle. The Coulomb equation differs from rheological equations typically applied in homogeneous models because it implies no dependence of stress on shear rate. The equation predicts essentially the same intergranular shear stress if normal stress on shear planes is the same, regardless of shear rate. Iverson and Vallance (2001) indicate that the Coulomb equation yields good predictions even when flow is rapid or partially liquefied by high fluid pressure.

For gravity-driven flows with a free upper surface, the compressive normal stress on planes at depth h is given by:

$$\sigma = (\rho_s - \rho_f) C_s g h \cos\theta - p \tag{18}$$

where C_s is grain concentration, θ the angle of surface inclination and p the pore fluid pressure. Iverson and Vallance (2001) also indicate that equation (18) is valid regardless of whether grains contact one another statically or dynamically collide. However, it has been demonstrated that bulk normal stresses in rapid, collision–dominated flows (N_s>0.1) depend on shear rate, whereas this dependence is absent in slower, friction dominated flows (Bagnold, 1954).

Bagnold's experiments also assessed the role of viscous stresses in granular mixtures. Bagnold distinguished contributions of grain collision and viscous stresses in steady, uniform, shear flows on the basis of a dimensionless parameter, N_B, defined as:

$$N_B = \left[\frac{C_s^{1/3}}{C_*^{1/3} - C_s^{1/3}} \right] \frac{\rho_s \dot{\gamma} d^2}{\mu} \tag{19}$$

Bagnold's number, N_B, depends on the same properties used to calculate Savage's number N_s, but also depends on C_s, the volume fraction of granular solids, C_*, the maximum (close-packed) value of C_s, and μ, the viscosity of the intergranular fluid. Values of N_B smaller than ~ 40 indicate a macroviscous regime where both normal and shear stresses are proportional to the shear rate $\dot{\gamma}$. Values of N_B larger than ~ 450 indicate a collision-dominated flow regime, in which normal and shear stresses are both proportional to $\dot{\gamma}^2$ (Bagnold, 1954).

The term in brackets in (19) highlights the important influence of grain concentration C_s on the stress regime. In the dense flow limit $(C_s \to C_*)$ the term in

brackets approaches ., indicating that collisional stresses greatly surpass viscous stresses. However, in highly concentrated geophysical flows with free upper surfaces, gH generally exceeds $\dot{\gamma}^2 d^2$ very significantly, then N_s<0.1, and Coulomb friction due to gravitational stress may surpass all other forms of shear resistance (Iverson and Denlinger, 2001).

Evaluation of stress regimes in debris flows in terms of N_s and N_B is not a straightforward task. Debris flows have definite starting and ending points in space and time, and their motion is clearly unsteady. Abrupt surge fronts form at the heads of most flows, followed by thinner, tapering tails. Changes in grain concentration C_s, grain-size d and flow depth H during unsteady motion allow variations in N_s and N_B throughout the extent and duration of the flow. Experimental data and field observations indicate that high non-uniform fluid pressures commonly exists in the bodies of debris flows, but not at surge fronts or deposit margins. Therefore, Coulomb friction generally dominates flow resistance at surge fronts, and viscous resistance and grain collisions gain significance in flow interiors (Iverson and Denlinger, 2001).

Lack of rate-dependent stresses implied by Coulomb friction does not eliminate rate dependence in a mixture of Coulomb solids and fluid, provided the fluid has nonzero viscosity. The degree of rate dependence in such mixtures depends on the degree to which fluid pressures reduce intergranular Coulomb friction and transfer shear stresses to the fluid phase. The conclusion is that only Coulomb friction theory is not appropriate to model stresses in mixtures of solids and fluid, the development of a mixture theory that takes into account fluid stresses is necessary.

2.4 Governing Equations for the Mixture Theory

The basic mixture theory has its origins in the pioneering model of Savage and Hutter (1989) for mass avalanches of cohesionless granules (sand, grains, rocks or snow). They began with mass and momentum balance laws based on a Coulomb constitutive description of dry granular material. Assuming a small depth-to-length aspect ratio in typical flows Savage and Hutter developed a thin layer model for granular flows down inclined planes. That work was later extended to two dimensions (Hutter *et al*., 1993), and to flows over more general topography (Pudasaini & Hutter, 2003). Iverson (1997b) and Iverson & Denlinger (2001) argue that the presence of interstitial fluid, as it is the case of debris flows, alters the behavior of dry flows and then equations describing the fluid phase and its constitutive behavior must be included. In this case, separate but coupled equations must describe mass and momentum conservation for the debris flow's solid and fluid constituents, and the solid and fluid equations should apply at all locations simultaneously.

The mixture theory equations of motion presented by Iverson and Denlinger (2001) read

$$\left.\begin{aligned} &\frac{\partial(\rho_S C_s)}{\partial t} + \nabla\cdot(\rho_S C_s \mathbf{v}_s) = 0 \\ &\frac{\partial(\rho_f C_f)}{\partial t} + \nabla\cdot(\rho_f C_f \mathbf{v}_f) = 0 \end{aligned}\right\} \tag{20}$$

$$\left.\begin{aligned} &\rho_s C_s\left(\frac{\partial \mathbf{v}_s}{\partial t} + \mathbf{v}_s\cdot\nabla\mathbf{v}_s\right) = \nabla\cdot\mathbf{T}_s + \rho_s C_s\mathbf{g} + \mathbf{f} \\ &\rho_f C_f\left(\frac{\partial \mathbf{v}_f}{\partial t} + \mathbf{v}_f\cdot\nabla\mathbf{v}_f\right) = \nabla\cdot\mathbf{T}_f + \rho_f C_f\mathbf{g} - \mathbf{f} \end{aligned}\right\} \tag{21}$$

where (20) represents the mass conservation equations and (21) the momentum conservation equations. There, **v** denotes a velocity vectors and **T** denotes a stress tensors. Subscript *s* refers to the solid phase and subscript *f* refers to the fluid phase. C_f refers to volume fraction of fluid, then mass continuity equations are coupled because the volume fractions must obey $C_s + C_f = 1$. In the momentum equations **f** is a vector that represents the interaction force per unit volume that results from momentum exchange between the solid and fluid constituents. Momentum equations are coupled through this force.

By adding together the solid and fluid mass conservation equations and the solid and fluid momentum equations, Iverson derives conservation laws for the mixture which involve depth averaging. Guided by experimental results, several approximations are then made which include:

i) Solid velocity is approximated to the fluid velocity.

ii) The mixture stress is taken as the sum $\mathbf{T}_s + \mathbf{T}_f$. Solid phase stresses obey the Coulomb rule with no cohesion and fluid phase stresses are considered to obey the conventional linear law of Newtonian fluids.

iii) The viscous components of the fluid stress are often ignored compared with the solid stress contributions.

iv) Basal pore fluid pressure obeys an advective-diffusion equation where advection is usually neglected. The solution proposed is a time series expansion depending on time and the depth of fluid.

Equations (20) and (21) show explicitly the advantages of two-phase models over single-phase models. They account for solid and fluid volume fractions, so it is possible to follow the evolution of each phase through space and time. They include separate solid and fluid stress tensors, which means that a constitutive relation must be defined for each phase. Equations also include the solid-fluid interaction force, which is implicit in single-phase models though the stress terms.

However, unfortunately, when using the solid phase velocity as an estimate of the fluid velocity and neglecting the influence of fluid stresses, most of these advantages are lost and the two-phase model reduces basically to a single-solid-phase model similar to that proposed by Savage and Hutter (1989).

Recently, Pitman and Le (2005) presented a model formulation with a set of equations describing a two-fluid model for debris flows, where velocities for both solid and fluid phases can be determined, as well as fluid depth and fraction of solid particles at any time and point in the space. Several forces are considered, including solid and fluid stresses, gravity, buoyancy and drag. However, they recognize the effort required computing solutions numerically and propose simplified models, and do not provide any comparison with experiments to demonstrate whether the equations adequately describe physical flows.

Despite the advantages of two-phase models over single-phase models, there are still many aspects that remain unresolved. In particular, it is known that debris flow is clearly unsteady, the flow regime can change in space and time from a friction dominated regime to a collision dominated regime or simply to a viscous dominated regime. Flow in the head behaves differently from the tail, since regimes are different, making very

difficult to model the whole flow extent with the same constitutive law. Also, many factors related with the movement and interaction of individual boulders and coarse sediments cannot be addressed with continuous two-phase models. The above discussion indicates that particle oriented models applied to the solid phase could adequately address some of these model deficiencies and challenges.

2.5 Discrete Element Method

The Discrete Element Method (DEM) or Distinct Element Method is a numerical method based on the Lagrangian approach to simulate the motion of granular materials at the level of particles (elements). The principle of DEM is to track, in a time stepping simulation, the trajectory and rotation of each element in a system to evaluate its position and orientation, and then to calculate the interactions between the elements themselves and also between the elements and their environment. The interactions will then subsequently affect the elements positions.

The Distinct Element Method was developed by Cundall (1971) for the analysis of rock mechanics problems. Then, Cundall and Strack (1979) extended the method to general granular media and showed that DEM could be applied to simulate real granular asse

mblies. After this important paper, DEM has been used in different fields including chemical, civil, mechanical, environmental and aeronautical engineering, among others. The DEM model is described in detail by Asmar *et al.* (2002) to model 3D granular flows.

However, very few studies using DEM for solid-liquid systems can be found in the literature. In the field of debris flow, Asmar *et al.* (2003), and Miyazawa *et al*. (2003) are two important works that propose DEM to simulate the solid phase of the flow, and Navier-Stokes equations to simulate the fluid phase. Asmar *et al.* (2003) presented a simplified mathematical model to simulate debris flows. However, the programming of the fluid phase was not performed and an explicit procedure to solve for the fluid unknowns, in conjunction with the tracking of solid particles, is not proposed. Miyazawa et al. (2003) presented a one-dimensional flow formulation to simulate debris flow through a grid type sabo dam, where DEM is applied in 3D to track movement of large boulders. In their work it is not clear how the DEM technique is combined with the traditional Eulerian approach to solve the equations. Other reported work proposes, but does not implement, the Smoothed Particle Hydrodynamics method, SPH, to model the fluid phase and DEM to model the solid phase (Clearly and Prakash, 2004).

When DEM is applied to simulate granular materials, two different methods to calculate the particle trajectories can be used: hard-particle model and soft-particle model. The hard-particle model works in rapid, not so dense granular flows where the system exhibits instantaneous binary collisions. In this regime, conservation of linear and angular momentum for each collision is applied. The soft-particle technique is used in slow, dense granular flows where particles have enduring contacts and multiparticle collisions occur. In these flows a dynamic analysis is performed via explicit solution of Newton's equation of motion for every particle. In the analysis, the particle positions are recorded first, from these the particle interactions are determined and then the subsequent dynamics are evaluated including all forces acting on each particle. From the equations of

motion accelerations are determined, which are then numerically integrated to obtain velocities and displacements at the next time step. This soft-particle approach is considered the most appropriate to model debris flows (Asmar *et al*. 2003; Miyazawa *et al.* 2003; Clearly and Prakash 2004).

The linear dynamics equations of motion for the particles (in vector notation) are as follows

$$m_i \frac{d\mathbf{v}}{dt} = \sum \mathbf{F}_E + \sum \mathbf{F}_N + \sum \mathbf{F}_T \tag{22}$$

Where m is the mass of particle i, $\mathbf{v}$ denotes in this case velocity vector of particle i, $\sum \mathbf{F}_E$ is the sum of the external forces (no contact forces), $\sum \mathbf{F}_N$ is the sum of the normal contact forces and $\sum \mathbf{F}_T$ is the sum of the tangential contact forces.

The external forces acting on the particles depend on the particular case to be modeled. When particles are submerged in a fluid these forces could include gravitational force, buoyancy force, fluid drag force and fluid lift force. While external particle forces can be easily added to the model, contact forces on the other hand are wholly dependent on the choice of the contact mechanics to be used.

Two major approaches are widely used in DEM. The first approach is a detailed methodology based on contact mechanics equations such as developed by Hertz (1882), Mindlin (1949), and Thornton and Randall (1988). The second approach is a simplified model that uses a conventional spring-dashpot-slider system to represent particle interactions as shown in Figure 10.

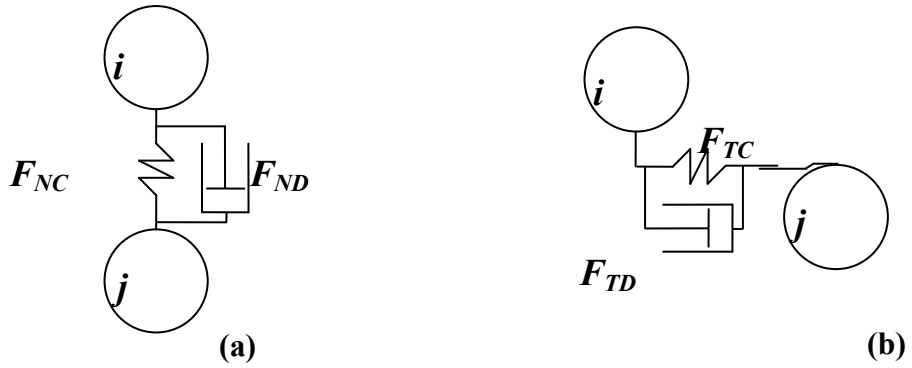

Figure 10. Schematic representation of contact forces (a) Normal (b) Tangential

The contact forces considered in this simplified model are elastic, cohesion, friction and damping forces. When particles are submerged in a fluid cohesion can be neglected and consideration not only of local damping, but also of global damping in the equations of motion could be considered.

Then, according to Figure 10

$$\mathbf{F}_N = \mathbf{F}_{NC} + \mathbf{F}_{ND} \tag{23}$$

$$\mathbf{F}_T = \mathbf{F}_{TC} + \mathbf{F}_{TD} \tag{24}$$

The normal contact force F_{NC} represents the repulsive force between any two particles that are in contact, it is calculated using a simple Hook's linear spring relationship. The normal damping force F_{ND} represents the dissipation of a portion of kinetic energy during the contact. It can be defined to have a required ratio between relative normal velocities before and after collision.

The tangential contact force F_{TC} represents the friction force between particles in contact. This force is limited by the Coulomb frictional limit at which point the surface contact shears and the particles begin to slide over each other. Before sliding linear or nonlinear formulations can be used, after sliding the tangential force is proportional to the normal contact force through the coefficient of friction.

The tangential damping force F_{TD} represents the portion of energy dissipated during tangential contact and it can be defined to have a required ratio between relative tangential velocities before and after collision. The calculation of this force could be omitted if sliding occurs since damping is introduced due to friction during motion.

Once forces are evaluated, particle *i* motion is calculated from equation (22). The acceleration of the particle $\frac{d\mathbf{v}}{dt}$ is computed from the net force, which is then integrated for velocity and displacement.

In order to determine the orientation of the particles in space, a similar procedure as described before is done in DEM, but in this case using the rotational equations of motion for the particles as follows

$$I_i \frac{d\boldsymbol{\omega}}{dt} = \sum \mathbf{M} \tag{25}$$

where ***I*** is the moment of inertia of particle ***i***, ω is the angular velocity and ***M*** is the moment produced by tangential forces acting on the particle. The angular acceleration of the particle $\frac{d\boldsymbol{\omega}}{dt}$ is computed from (25), which is then integrated for angular velocity and angle vector.

The time step Δt is a constant value that is chosen to ensure the stability and accuracy of the numerical simulation, particularly the integration. In DEM this critical time for a simple elastic model is defined by

$$T_{cr} = \frac{2}{\omega_c} \tag{26}$$

$$\omega_c = \sqrt{\frac{m}{k}} \tag{27}$$

where ω_c is the natural frequency of a simple spring-mass system, k is the maximum stiffness and m the minimum particle mass. For a stable condition the time step must be smaller than this critical time.

Cundall (1978) suggests that 10% of critical time is probably safe for most of the DEM problems, but 20%-50% may be used with caution for loosely packed systems.

3 RESEARCH METHODOLOGY

3.1 Governing Equations

The flow domain is divided in computational cells with triangular base and height *H*, the actual depth of fluid, as shown in Figure 11.

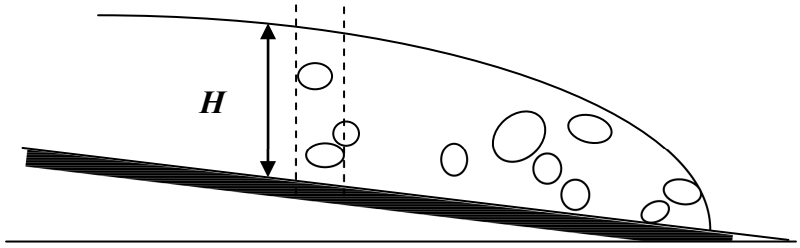

Figure 11. Schematic representation of debris flow with large solid particles

The fluid is assumed to be non-Newtonian and incompressible, and the vertically averaged continuity and momentum equations in Cartesian coordinates result as follows (see derivation in the Appendix).

Continuity:

$$\frac{\partial H}{\partial t}+\frac{\partial(\overline{u}H)}{\partial x}+\frac{\partial(\overline{v}H)}{\partial y}=0 \tag{28}$$

x-Momentum:

$$\frac{1}{g}\frac{\partial \overline{u}}{\partial t}+\frac{\overline{u}}{g}\frac{\partial \overline{u}}{\partial x}+\frac{\overline{v}}{g}\frac{\partial \overline{u}}{\partial y}+\frac{\partial \eta}{\partial x}+\frac{F_{Dx}}{\rho g}+S_{fx}=0 \tag{29}$$

y-Momentum

$$\frac{1}{g}\frac{\partial \overline{v}}{\partial t}+\frac{\overline{u}}{g}\frac{\partial \overline{v}}{\partial x}+\frac{\overline{v}}{g}\frac{\partial \overline{v}}{\partial y}+\frac{\partial \eta}{\partial y}+\frac{F_{Dx}}{\rho g}+S_{fy}=0 \tag{30}$$

Similarly to equations (1) to (3), H is the water depth, η is the free-surface elevation, $\bar{u}$ and $\bar{v}$ are the vertically averaged velocities in x and y directions respectively, g is the gravitational acceleration and ρ is fluid density.

$\mathbf{F}_D$ represents the fluid-solid interaction force exerted on the fluid by particles through the fluid drag force. Following the approach of Xu & Yu (1997), this force is evaluated as

$$\mathbf{F}_D = \frac{\sum_{i=1}^{n} \mathbf{F}_{FDi}}{\Delta V} \tag{31}$$

where $\mathbf{F}_{FD}$ is the fluid drag force on each particle i, ΔV is the volume of the computational cell and n is the number of particles in the cell. In this manner, the fluid interface force $\mathbf{F}_D$ in a computational cell is equal to the sum of the fluid drag forces acting on the discrete particles into the cell. F_{Dx} and F_{Dy} are the components of the fluid interface force in x and y direction respectively.

S_{fx} and S_{fy} are the depth integrated stress terms that depend on the rheological formulation used to model the slurry.

When a quadratical formulation is used, with Bingham theory and Manning's formula, as proposed by O'Brien and Julien in 1985, the stress terms for the fluid can be expressed as

$$S_{fx} = \frac{\tau_y}{\rho g H} + \frac{3\mu\bar{u}}{\rho g H^2} + \frac{N^2 \bar{u}^2}{H^{4/3}} \tag{32}$$

$$S_{fy} = \frac{\tau_y}{\rho g H} + \frac{3\mu\bar{v}}{\rho g H^2} + \frac{N^2 \bar{v}^2}{H^{4/3}} \tag{33}$$

The properties of the fluid, dynamic viscosity μ and yield stress τ_y, are determine as functions of the volume sediment concentration *Cv*, using the relationships proposed by O'Brien and Julien (1988) and given in equations (9) and (10). *N* is the Manning roughness coefficient related with the roughness of bottom surface.

Using a quadratical formulation combined with the Cross rheological model, the stress terms for the fluid are expressed as (see derivations in Appendix A):

$$S_{fx} = \frac{\mu_{eff}\dot{\gamma}}{\rho g H} + \frac{N^2 \overline{u}^2}{H^{4/3}} \quad \text{with} \qquad \dot{\gamma} = \frac{3\overline{u}}{H} \tag{34}$$

$$S_{fy} = \frac{\mu_{eff}\dot{\gamma}}{\rho g H} + \frac{N^2 \overline{v}^2}{H^{4/3}} \quad \text{with} \qquad \dot{\gamma} = \frac{3\overline{v}}{H} \tag{35}$$

where μ_{eff} is the effective viscosity of the fluid defined by (13) and (14). The properties of the fluid required to determine the effective viscosity are the dynamic viscosity μ and yield stress τ_y,

In reference to the solid phase, spherical particles of different sizes will be considered. The trajectories will be tracked using Newton's second law (22) and the forces considered are gravity, buoyancy, fluid drag force and collision forces.

Recalling equation (22):

$$m_i \frac{d\mathbf{v}}{dt} = \sum \mathbf{F}_E + \sum \mathbf{F}_N + \sum \mathbf{F}_T$$

$\sum \mathbf{F}_E$ is the sum of the external forces (no contact forces), with $\mathbf{F}_E$ given by

$$\mathbf{F}_E = \mathbf{F}_B + \mathbf{F}_{FD} \tag{36}$$

The expression to compute the net force acting on the particle due to gravitational effects is

$$\mathbf{F}_B = \frac{4}{3}\pi R^3(\rho - \rho_p)\mathbf{g} \tag{37}$$

where R is the particle radius and ρ_p is the particle density.

The expression for the drag on a particle in a viscous fluid is given by

$$\mathbf{F}_{FD} = \frac{1}{2}\pi R^2 C_d \rho |\mathbf{u} - \mathbf{v}|(\mathbf{u} - \mathbf{v}) \tag{38}$$

where C_d is the drag coefficient, **u** is the fluid velocity vector at the location of the particle, and **v** is the velocity vector of the particle.

Several expressions for the drag coefficient of a sphere in a viscous fluid are found in the literature. One of these is the correlation given by Clift and Gauvin (1971):

$$C_d = \frac{24}{\mathrm{Re_p}}\left[1 + 0.15\mathrm{Re_p}^{0.687}\right] \qquad \text{for } 1 < \mathrm{Re_p} < 1000 \tag{39}$$

where $\mathrm{Re_p}$ is the particle Reynolds number defined by

$$\mathrm{Re}_{\mathrm{p}} = \frac{2\rho R|\mathbf{u}-\mathbf{v}|}{\mu_{eff}} \tag{40}$$

This expression for the drag coefficient is accurate up to Re_{p} equal to 1000. For higher Reynolds numbers, it is observed that the drag coefficient of a sphere becomes constant and approximately equal to 0.44.

Figure 12 shows the correlation for the drag coefficient used in the calculations of the particle drag force.

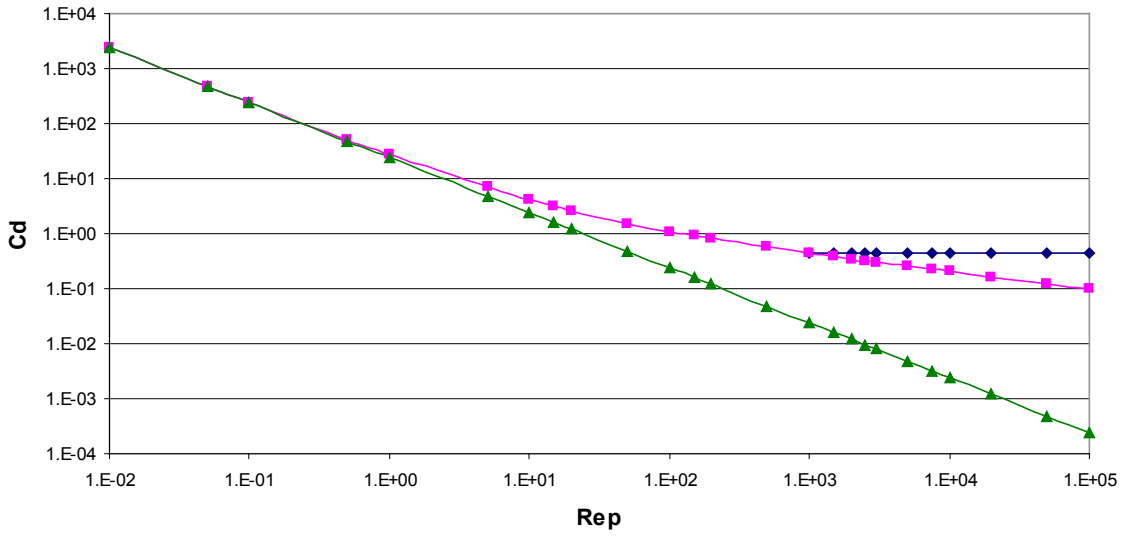

Figure 12. Drag Coefficient vs particle Reynolds number

Going back to equation (22), the last two terms represent the collision forces or contact forces among particles $\sum \mathbf{F}_N$ is the sum of the normal contact forces and $\sum \mathbf{F}_T$ is the sum of the tangential contact forces. Based on the simplified model that uses a spring-dashpot-slider system to represent particle interactions (Asmar *et al.* 2003;

Miyazawa *et al.* 2003), the normal contact force and the tangential contact force are evaluated as in (23) and (24), see Figure 10.

$$\mathbf{F}_N = \mathbf{F}_{NC} + \mathbf{F}_{ND}$$

$$\mathbf{F}_T = \mathbf{F}_{TC} + \mathbf{F}_{TD}$$

The normal contact force F_{NC} is calculated using a Hook's linear spring relationship,

$$\mathbf{F}_{NC} = K_N \delta_N \tag{41}$$

where K_N is the normal contact stiffness and δ_N is the displacement between particles *i* and *j*.

The displacement δ_N is mimicked via a computational overlap (see Figure 13), so that $\delta_N = (R_i + R_j) - \Delta_{ij}$, where Δ_{ij} is the distance between the centers of particle *i* and *j*. When Δ_{ij} is greater than $(R_i + R_j)$ particles are not in contact.

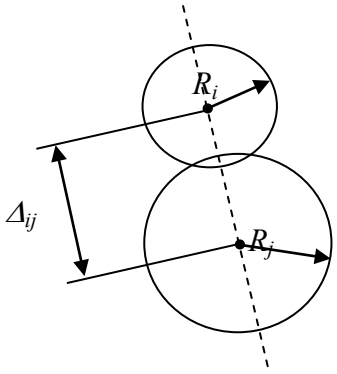

Figure 13. Schematic representation of contact between two particles

The maximum overlap is dependent on the stiffness K_N. Typically, average overlaps of 0.1-1.0% are desirable, requiring stiffness of the order 10^5-10^7 N/m.

The normal damping force F_{ND} is also calculated using a linear relation given by

$$\mathbf{F}_{ND} = C_N v_N \tag{42}$$

where v_N is the normal component of the relative velocity between particles and C_N is the normal damping coefficient. This constant C_N is chosen to give a required coefficient of restitution β, defined as the ratio of the normal component of the relative velocities before and after collision.

$$C_N = 2\lambda\sqrt{m_{ij} K_N} \tag{43}$$

where λ is the coefficient of critical damping and is calculated as

$$\lambda = -\frac{\ln(\beta)}{\sqrt{\pi^2 + \ln^2(\beta)}} \tag{44}$$

and

$$m_{ij} = \frac{m_i m_j}{m_i + m_j} \tag{45}$$

where m_i and m_j are masses of particle i and j respectively. Derivation of the critical damping coefficient could be found in Nagurka and Huang, 2006.

The tangential contact force, $\mathbf{F}_{TC,}$ represents the friction force and it is limited by the Coulomb frictional limit, at which point the particles begin to slide over each other.

Prior to sliding, the tangential contact force is calculated using a linear spring relationship,

$$\mathbf{F}_{TC} = K_T \delta_T \tag{46}$$

where K_T is the tangential stiffness coefficient, and δ_T is the total tangential displacement between the surfaces of particles i and j since their initial contact. This displacement is calculated from the components of relative velocity tangent to the contact surface. Values suggested for K_T / K_N varies from 2/3 to 1 (Cundall and Strack, 1979). When $K_T \delta_T$ exceeds the frictional limit force $\mu_f F_{NC}$, particle sliding occurs. The sliding condition is defined as

$$\mathbf{F}_{TC} = \mu_f \mathbf{F}_{NC} \tag{47}$$

where μ_f is the dynamic friction coefficient.

The tangential damping force $\mathbf{F}_{TD}$ is not included in this model, the calculation of this force could be neglected since once sliding occurs, damping is introduced due to friction during motion.

In this work, the rotation of the particles is not considered. The effect of particle rotation and the corresponding lift produced could be modeled by solving for the angular velocity of the particles in equation (25), including the torque exerted on them by the fluid and by the contact with other particles.

The torque exerted by the viscous fluid on solid particles is produced by fluid shear stresses and can be expressed in terms of the velocity gradients as follows (Sandeep, 1996):

$$M_x = \pi a^3 \mu \left(\frac{\partial v}{\partial z} + \frac{\partial w}{\partial y} \right) \tag{48}$$

$$M_y = \pi a^3 \mu \left(\frac{\partial u}{\partial z} + \frac{\partial w}{\partial x} \right) \tag{49}$$

$$M_z = \pi a^3 \mu \left(\frac{\partial u}{\partial y} + \frac{\partial w}{\partial x} \right) \tag{50}$$

Since the fluid phase governing equations are depth integrated, gradients along *z* direction are equal to zero in the formulation, as well as the velocity in this direction, *w*. Then the first two components of the torque are not detectable by the numerical model. Last component is the torque in direction perpendicular to the sloping surface, which is essentially negligible.

Regarding the torque exerted by contact forces, debris flow observations say that big boulders usually move protruding from the surface of the flow, barely in contact with the bottom surface The Bingham fluid model shows how the yield stress of the fluid produce a plug layer close to the surface, big boulders are supported by the strength of this plug and buoyancy, been transported long distances without significant contact with other bodies (Takahashi, 1991). As the flow depth is reduced, the process of boulder deposition starts and contact forces become more relevant. It has been reported that the lacking of rotation in the simulation of the deposition process allows the formation of clusters more easily than in the case where rotation of particles is included, however there is not significant difference in the final position of the particles.

. It is one of the main interests of this work to study the transportation of big solid particles by debris flow, in order to be able to predict zones of deposition.

3.2 Numerical Solution of the Governing Equations

3.2.1 Fluid Governing Equations

Fluid governing equations (28-30) are solved by the Galerkin Finite Element method using three-node triangular elements. The unknown variables, *u*, *v*, and *H*, are given as a function of the unknowns evaluated at the nodes (48), where the vectors $\vec{U}(t)$, $\vec{V}(t)$, and $\vec{H}(t)$ represent the variables at the nodes for each time *t*, and the matrix N allows for the internal interpolation based on linear shape functions defined for triangular elements with three nodes (49).

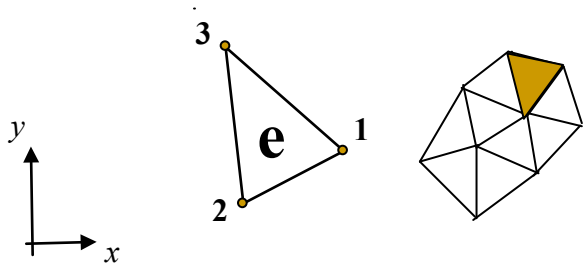

Figure 14. Finite Element Discretization

$$\left.\begin{aligned} \overline{u}(x,y,t) &= [N]\vec{U}(t) \\ \overline{v}(x,y,t) &= [N]\vec{V}(t) \\ \overline{H}(x,y,t) &= [N]\vec{H}(t) \end{aligned}\right\} \tag{51}$$

$$[N] = \begin{bmatrix} N_1 & N_2 & N_3 \end{bmatrix} \tag{52}$$

The spatial derivatives are expressed as

$$\frac{\partial \overline{u}}{\partial x} = [B_x]\vec{U} \tag{53}$$

$$\frac{\partial \overline{u}}{\partial y} = [B_y]\vec{U} \tag{54}$$

where matrix B_x and B_y contain the derivative of matrix N with respect to x and y respectively.

$$[B_x] = \left[\frac{\partial N_1}{\partial x} \quad \frac{\partial N_2}{\partial x} \quad \frac{\partial N_3}{\partial x} \right] \tag{55}$$

$$[B_y] = \left[\frac{\partial N_1}{\partial y} \quad \frac{\partial N_2}{\partial y} \quad \frac{\partial N_3}{\partial y} \right] \tag{56}$$

The discretized governing equations can be expressed in matrix form as follows

$$\left.\begin{aligned} [M]\dot{\vec{H}} &= -\vec{F}_h \\ [M]\dot{\vec{U}} &= -\vec{F}_u \\ [M]\dot{\vec{V}} &= -\vec{F}_v \end{aligned}\right\} \tag{57}$$

where the vector of unknowns (time derivatives) multiply matrix M for each equation, and the right hand side vector include all the other terms in the equation. Matrix M is given by

$$[M] = \int N^T N dA \tag{58}$$

To solve (58), a four-step time stepping scheme and a selective lumping method, is performed, as described by Garcia-Martinez *et al*. (2006). This scheme improves previous finite elements models, allowing larger time steps and enhancing its capability to simulate complex debris flow events without requiring an artificial diffusion term.

Stability leads to the following Courant-Friederich-Lewy (CFL) condition

$$\frac{\Delta t}{\Delta x} \leq \frac{4}{3}\left(\frac{3}{gH}\right)^{1/2}(1-\varepsilon)^{1/2} \tag{59}$$

where ε is the selective lumping parameter.

3.2.2 Particle Governing Equations

Forces on each solid particle are evaluated at each time step, and the acceleration of the particle $\frac{d\mathbf{v}}{dt}$ is computed from the particle governing equation (22). Particle acceleration is then integrated to find velocity and displacement as follows

$$\mathbf{v}^{t+\Delta t} = \mathbf{v}^{t} + \frac{d\mathbf{v}^{t}}{dt}\,\Delta t \tag{60}$$

$$\mathbf{r}^{t+\Delta t} = \mathbf{r}^{t} + \frac{1}{2}(\mathbf{v}^{t} + \mathbf{v}^{t+\Delta t})\,\Delta t \tag{61}$$

Knowing the position of particles at time $t+\Delta t$ contacts are identified and relative displacements among particles are calculated.

The time step Δt to ensure stability and accuracy of the numerical integration is determined by the minimum critical time, as said in previous chapter, equation (26).

The time step for the whole simulation, including fluid and solid phase, is chosen such as equations (26) and (59) are satisfied.

The following diagram describes the complete numerical procedure more explicitly

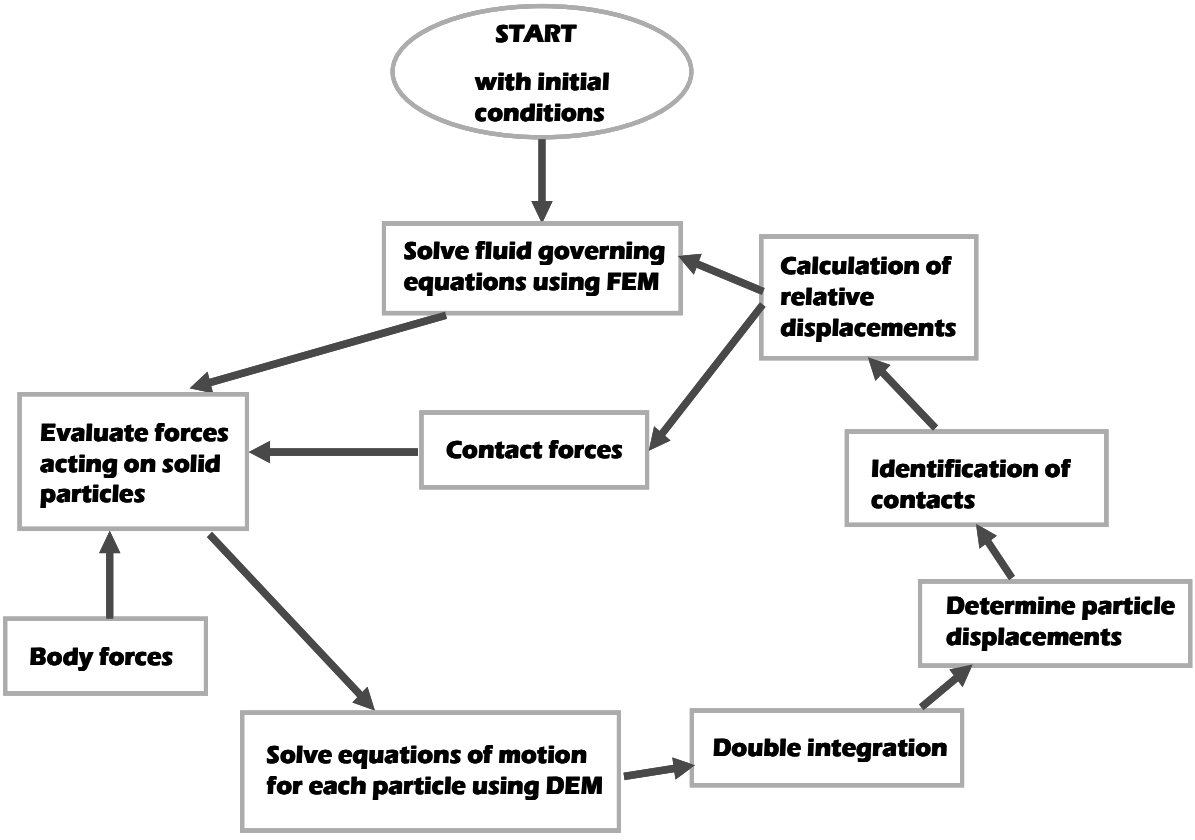

Figure 15. Calculation cycle describing the numerical solution of the problem

4 MODEL VERIFICATION USING ANALYTICAL AND EXPERIMENTAL DATA

4.1 Fluid Phase Numerical Solution Verification

The first modeling step was the implementation of different rheological models for the simulation of mud flows. This modeling would account for the representation of the fluid phase of the debris flow. The numerical model was run using RiverFLO-2D software, a finite modeling system for detailed analysis of river hydrodynamics, sediment transport and bed evolution (García-Martínez *et al.* 2006). In the software, two rheological quadratical formulations were implemented, the first, including Bingham theory and Manning's formula, as proposed by O'Brien and Julien in 1985, and the second, combining Cross formulation and the Manning's formula as proposed in Martinez *et al*. 2006.

In order to compare with simple results, an analytical solution, proposed by Huang and Garcia (1997), was studied and implemented in a computer program. This implementation provided enough data for verification and testing of the new rheological formulations proposed.

4.1.1 Analytical Solution for Bingham mudflows, Huang and Garcia 1997

Consider a 2D, unsteady, gradually varied, laminar mudflow, which originates from a finite-volume source, on a slope at an angle of θ with respect to the horizontal.

The boundary layer approximations are assumed to be valid, flow depth is small relative to the flow length, and depth changes relatively slowly along length. Then the equations of motion are reduced to the following form

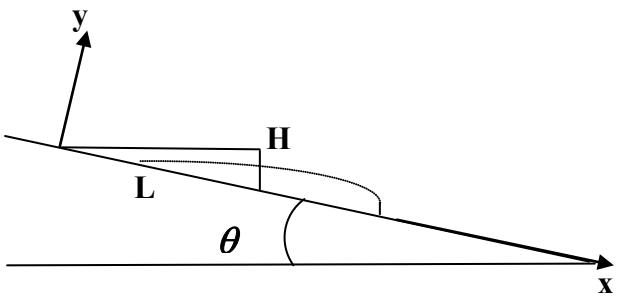

Figure 16. One-dimensional dam break on a sloping surface

$$\frac{\partial u}{\partial x}+\frac{\partial v}{\partial y}=0 \tag{62}$$

$$\rho\left(\frac{\partial u}{\partial t}+u\frac{\partial u}{\partial x}+v\frac{\partial u}{\partial y}\right)=-\frac{\partial p}{\partial x}+\rho gSin\theta+\frac{\partial \tau}{\partial y}=0 \tag{63}$$

$$\frac{\partial p}{\partial y}=-\rho gCos\theta \tag{64}$$

Where ρ is fluid density, g is acceleration of gravity, p is pressure and (u,v) are the flow velocity components in (x,y) directions respectively. The boundary conditions are in this case:

$$u=v=0 \quad at \quad y=0 \tag{65}$$

$$p=0, \quad \tau=0 \qquad at \quad y=h \tag{66}$$

Then, equations (64) and (66) indicate that pressure in the mudflow is hydrostatic and given by:

$$p=\rho g(h-y)\cos\theta \tag{67}$$

Huang and Garcia consider the two layer-model shown in Figure 17:

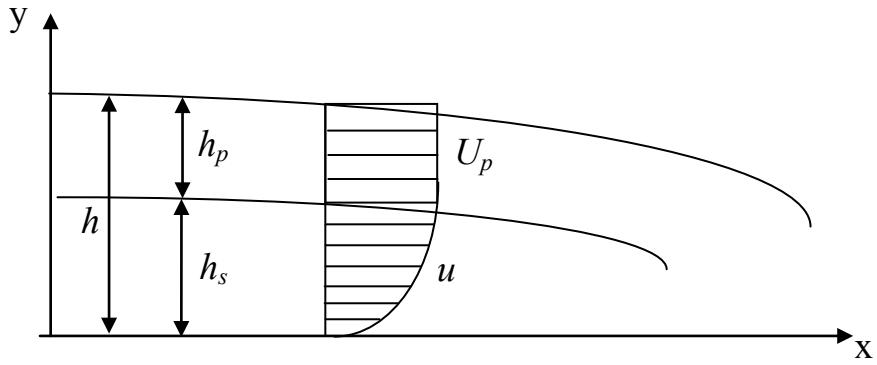

Figure 17. Two layer model proposed by Huang and Garcia, 1997

The flow is divided into a plug layer, with uniform velocity U_p and depth h_p, and a shear layer with varying velocity u and depth h_s. For the case of steady, uniform flow, the velocity distribution is given by

$$\begin{aligned} u &= U_p \quad h_s \le y \le h \\ u &= U_p\left(\frac{2y}{h_s} - \frac{y^2}{h_s^2}\right) \quad 0 \le y \le h \end{aligned} \tag{68}$$

and the flow rate per unit width is

$$q = U_p \frac{(3h - h_s)}{3} \tag{69}$$

Assuming that (68) is also valid for non-uniform boundary layer flows without committing serious errors (with U_p changing with x and time t), the following depth-

integrated momentum and continuity equations are obtained taking into account the surface boundary condition

$$v = \frac{\partial h}{\partial t} + U_p \frac{\partial h}{\partial x} \qquad at \quad y = h \tag{70}$$

Continuity

$$\frac{\partial h}{\partial t} + \frac{\partial q}{\partial x} = 0 \qquad with \qquad q = U_p \left(h - \frac{h_s}{3} \right) \tag{71}$$

Momentum balance in the shear layer

$$\frac{\partial}{\partial t}\left(\frac{2}{3}U_p h_s\right) + \frac{\partial}{\partial x}\left(\frac{8}{15}U_p^2 h_s\right) - U_p\left(\frac{\partial h_s}{\partial t} + \frac{\partial}{\partial x}\left(\frac{2}{3}U_p h_s\right)\right) = g h_s\left(\sin\theta - \frac{\partial h}{\partial x}\cos\theta\right) - \frac{2\mu U_p}{\rho h_s} \tag{72}$$

Momentum balance in the plug layer

$$\frac{\partial U_p}{\partial t} + \frac{\partial}{\partial x}\left(\frac{U_p^2}{2} + gh\cos\theta\right) = g\sin\theta - \frac{\tau_y}{\rho(h - h_s)} \tag{73}$$

These three equations could be solved numerically to look for the unknowns h, U_p and h_s**.** However; studying the relative magnitudes of the terms in these equations, it is possible to derive first-order solutions for the outer and inner regions of the flow. Refer to Appendix B for complete derivation of these equations.

The Outer Solution (Figure 18) describes the profile back at any time t. The corresponding equation (74) allows to solve for the depth of the fluid h* at any time t* and location x*.

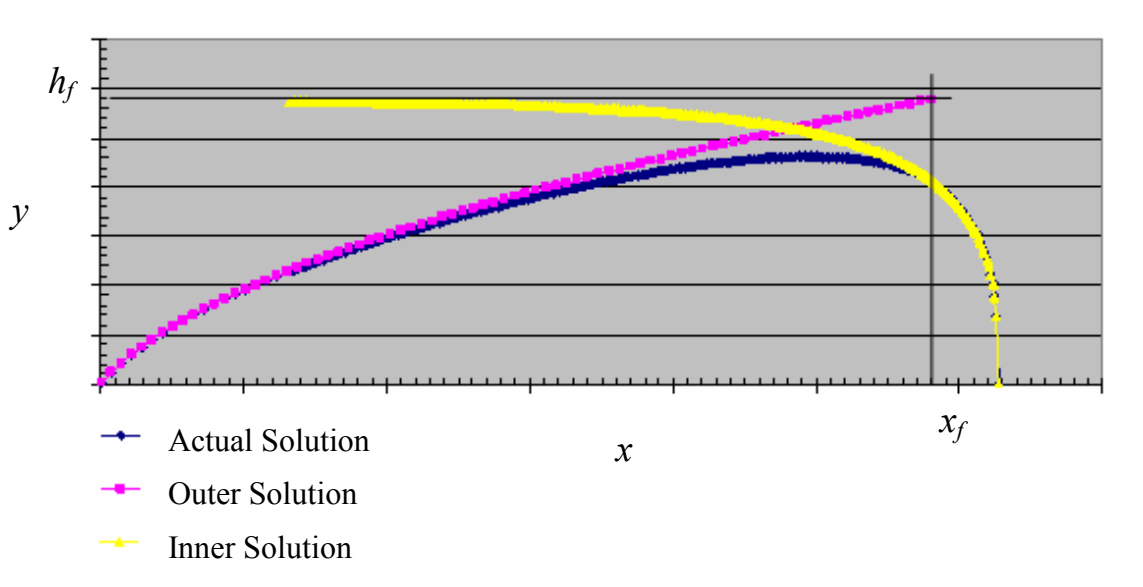

Figure 18. Outer and Inner Solution proposed by Huang and Garcia, 1997

$$x^* = (3h^{*2} - 3h^*\lambda)t^* + h^* \tag{74}$$

Equation (74) can be expressed in dimensional form with the help of (75).

$$(h^*, h_s^*, U_p^*, x^*, t^*, \varepsilon, \lambda, Fr) = (\frac{h}{h_0}, \frac{h_s}{h_0}, \frac{U_p}{U_0}, \frac{x}{l}, \frac{t}{U_0 l}, \frac{h_0}{l}, \frac{h_y}{h_0}, \frac{U_0}{\sqrt{gh_0}}) \tag{75}$$

The Outer solution holds up to the shock location (x_f, h_f). This location is determined invoking mass conservation, giving as a result the following nonlinear equation that can be used to solve for h_f.

$$t^* = \frac{1 - h_f^{*2}}{4h_f^{*3} - 3h_f^{*2}\lambda - \lambda^3} \tag{76}$$

Equation (74) gives then x_f.

The Inner Solution (Figure 18) describes the free surface profile of the shock front and it is found solving the following differential equation for h_i.

$$\frac{\partial h_i^*}{\partial \xi^*} = \left[1 - \frac{\lambda}{h_i^*} - \frac{\sqrt{(h_f^* - \lambda)^4 + 4h_i^* \lambda (h_f^* - \lambda)^2} + (h_f^* - \lambda)^2}{2h_i^{*2}} \right] \tan\theta \tag{77}$$

Since the right hand side of (77) is independent on ξ^*, the location of the profile is unknown. The right place will be given under the condition of mass conservation given by

$$\int_{-\infty}^{0} (h_f^* - h_i^*) d\xi^* = \int_{0}^{\delta^*} h_i^* d\xi^* \tag{78}$$

where δ* is defined as the distance from x_f * to the leading edge of the shock. Equations (77) and (78) can be expressed in dimensional form with the help of (79)

$$(h_i^*, h_{si}^*, \xi^*, U_i^*, U_{pi}^*, t_i^*) = \left(\frac{h}{h_0}, \frac{h_s}{h_0}, \frac{x^* - x_f}{\varepsilon}, \frac{u}{U_0}, \frac{U_p}{U_0}, \frac{t}{U_0 l}\right) \tag{79}$$

A numerical procedure was implemented in order to find automatically the entire profile of the mudflow released from a finite source, at any time *t*.

The input data includes dimensions of the mass source, *H* and *L*, or *H* and θ, and the properties of the fluid: density ρ, viscosity μ and yield stress τ_y.

For any time t the procedure is as follows:

Outer solution:

1.- Using equation (76), solve for h_f (Newton-Raphson method).

2.- Using equation (74) solve for x_f.

3.- From x=0 to x=x_f use equation (74) to determine the depth h of the fluid (Newton-Raphson method).

Inner solution:

4.- Apply Runge-Kutta to equation (77) to determine the profile h_i. The equation can be use in dimensional form.

5.- Apply numerical integration to find the right location for the inner solution. Start with the profile centered with respect to x_f and then iterate until the mass balance is achieved.

Composite solution:

6.- For x < x_f , determine the solution by adding the inner and outer solution and then subtracting their common matching term h_f. For x > x_f the solution equals the inner solution.

The following example is given by Huang and Garcia in their work (1997). The data presented is

$$\theta = 15^o, \quad x_f = 56.7cm, \quad h_f = 5.77cm, \quad h_y = 0.8\,cm$$

Using these values the corresponding input data for the developed program is:

$$\theta = 15^o, \quad h_0 = 10cm, \quad \tau_y = 29.7Pa, \quad \mu = 0.08Pa.s, \quad \rho = 1462Kg/m^3, t = 0{,}0027s$$

The results obtained using the program are:

$h_f = 5.77cm, \quad x_f = 57.99cm$ with the following free surface profile

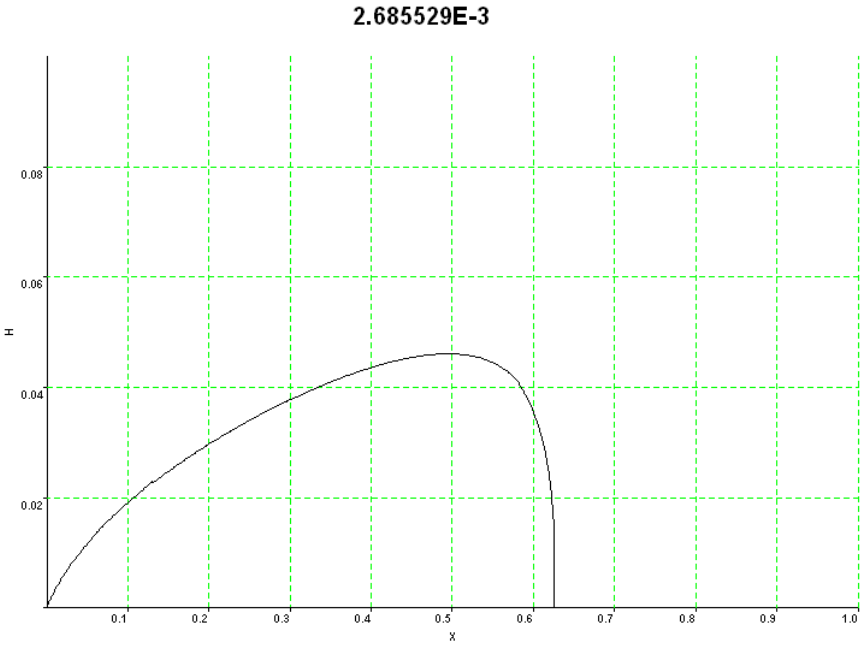

Figure 19. Flow profile at time t = 2.7 E-3 s

This solution is in very good agreement with Huang and Garcia's results. The program was then used to solve for other times *t* and results are showed in the following figures.

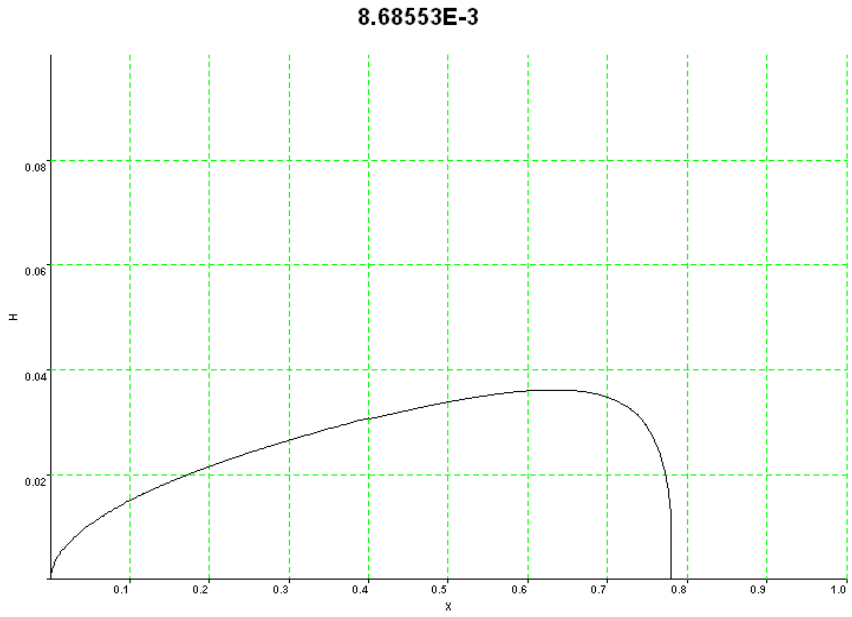

Figure 20. Flow profile at time t = 8.7 E-3 s

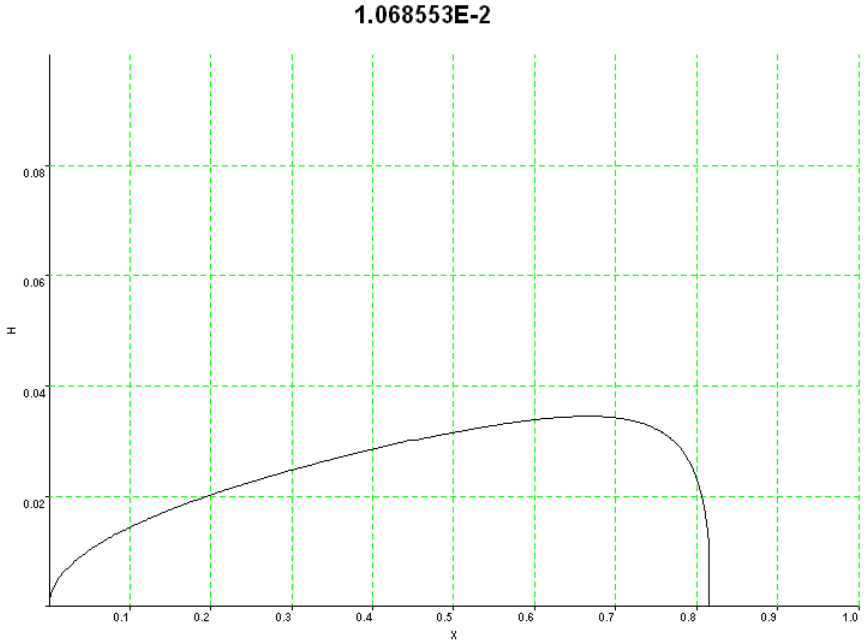

Figure 21. Flow profile at time t = 1.07 E-2 s

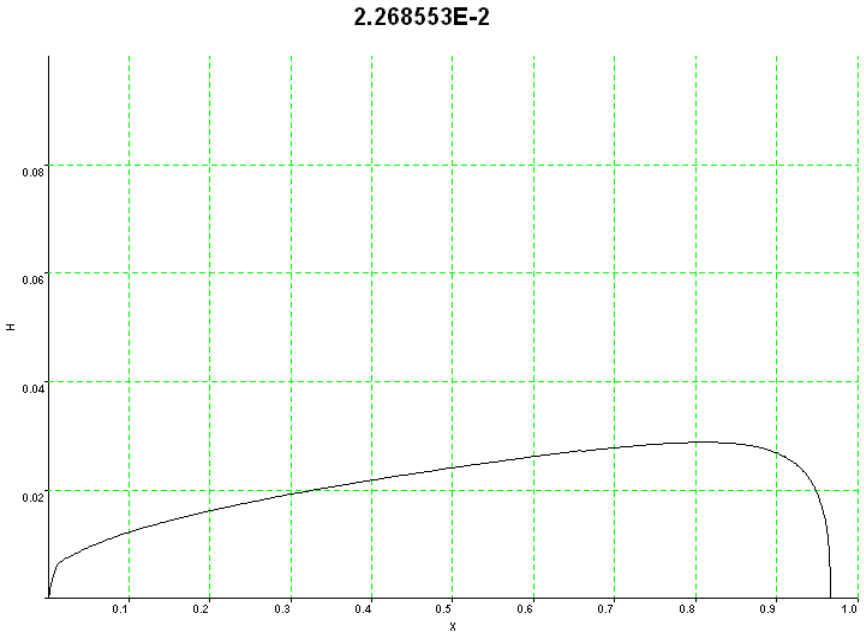

Figure 22. Flow profile at time t = 2.27 E-2 s

4.1.2 Finite Element Method (FEM) Numerical Solution testing and verification

The proposed test problem represents flow from a source of finite size, with initial triangular shape, a dam break of mud-slide on an sloping surface, as shown in Figure 16. The fluid is a Kaolinite suspension with C_v =0.135 and the flow is considered unsteady, gradually varied, and laminar. The empirical relationships (9) and (10) are used for the calculation of the fluid rheological properties,

$$\mu = \alpha_1 e^{\beta_1 \bar{c}} \qquad \tau_y = \alpha_2 e^{\beta_2 \bar{c}}$$

in which α_1, β_1, α_2 and β_2 are $\alpha_1 = 0.621\text{x}10^{-3}$, $\beta_1 = 17.3$, $\alpha_2 = 0.002$ and $\beta_2 = 34.2$. Units are *Pa.s* for viscosity and *Pa* for yield stress (O'Brien and Julien, 1988).

We compare the finite element numerical solution with the analytical solution proposed by Huang and Garcia (1997). We also compare the results with experimental data presented by Huang and Garcia in their work of 1998.

Although the example is one dimensional, we use 2D triangular elements to discretize the channel, as shown in Figure 23. The Cross rheological model is used first in the Finite Element Formulation.

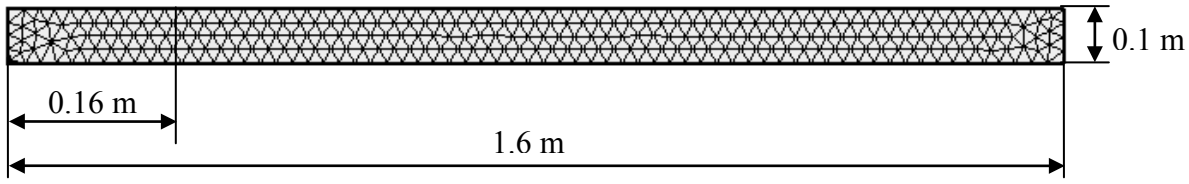

Figure 23. Two-dimensional finite element mesh for the dam break test

The following figures show the flow profile and spreading rate for the following conditions: θ=11^o and initial triangular area A=24.7cm^2 (L = 0.16 m).

Figures 24 and 25 show the free surface profiles for times 2.0 and 2.5 s, respectively. As it is depicted in the plots, the numerical solution is very close to the analytical solution, with the exception of the advancing front where the numerical solution is not able to capture the discontinuity between the fluid and the dry channel bottom. This smearing is a typical inaccuracy tied to numerical diffusion.

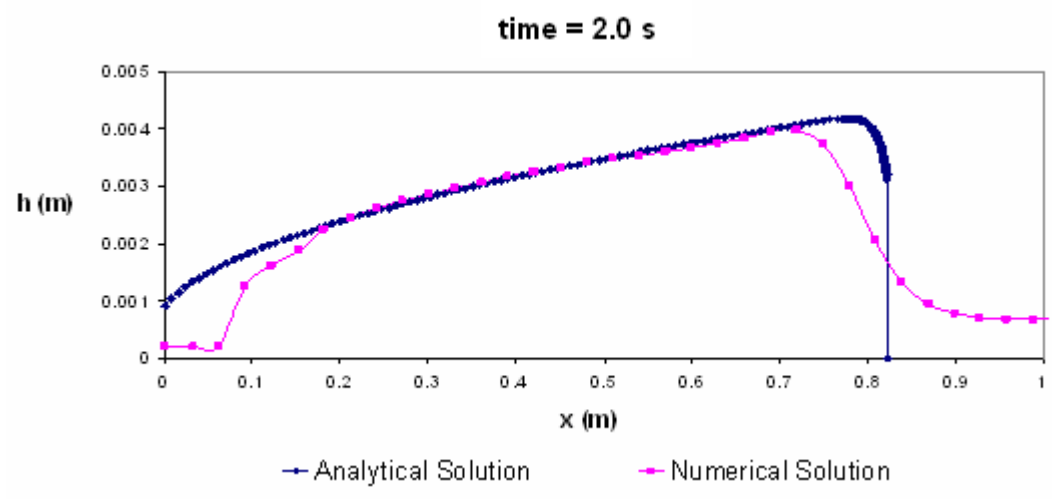

Figure 24. Comparison of numerical and analytical solutions for time = 2.0 s

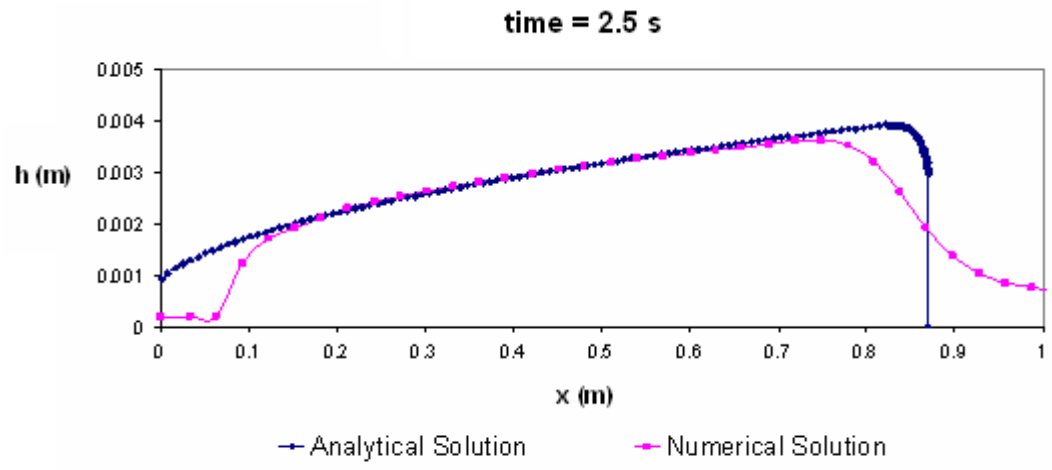

Figure 25. Comparison of numerical and analytical solutions for time = 2.5 s

Figure 26 shows free surface profiles for time 2.0 s using a refined mesh. In the new mesh (NM) elements are three times smaller than those in the old mesh (OM). In addition, the selective lumping parameter, related with the finite element solution of the governing equations, has been increased from 0.9 to 0.925.

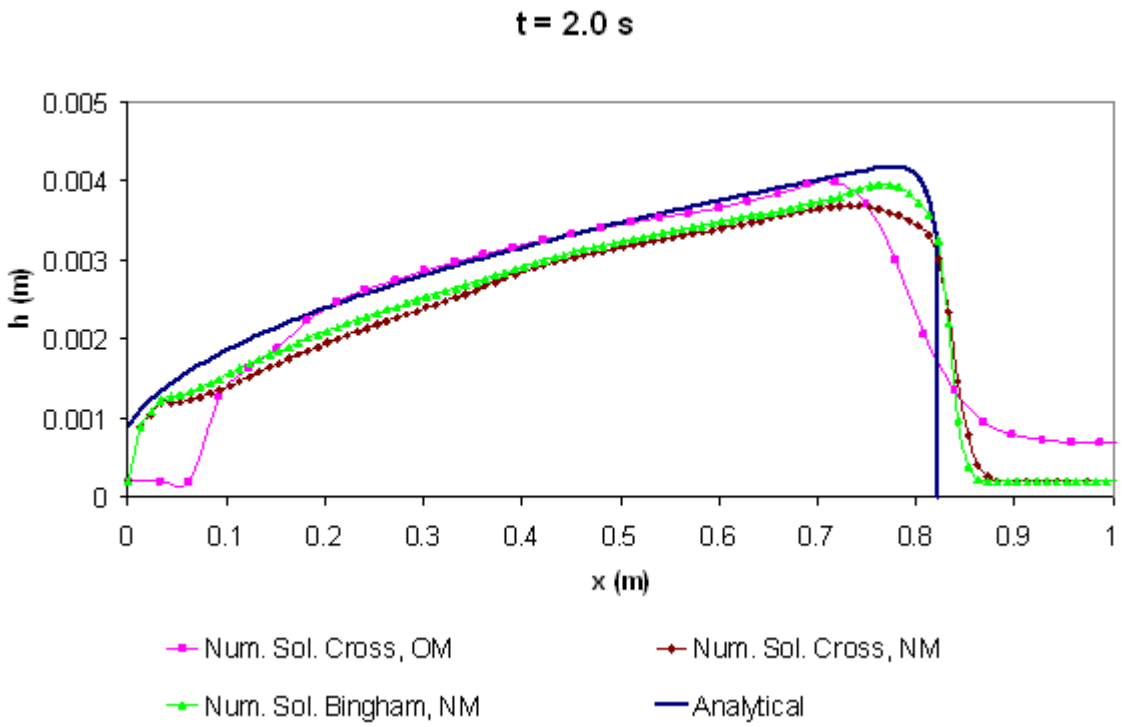

Figure 26. Free surface profiles, comparison of numerical and analytical solutions for time 2.0 s

As depicted in the figure, the mesh refinement contributes to reduce the numerical diffusion and improves substantially the solution in the advancing front. Increasing the selective lumping parameter also enhances the numerical solution, making it closer to the analytical solution. Bingham rheological formulation is compare with Cross rheological formulation, the Bingham profile shows a steeper front that Cross profile.

Figure 27 shows the spreading rate of the flow. This relation is obtained plotting the position of the advancing front at different times *t*. In the plot, numerical results using FEM are compared with the Analytical Solution as well as Experimental Data given by Huang and Garcia (1998). It is noticeable that the numerical solution using Cross

formulation is in very good agreement with the experimental data for early stages of the solution, where the approximate analytical solution is not as accurate.

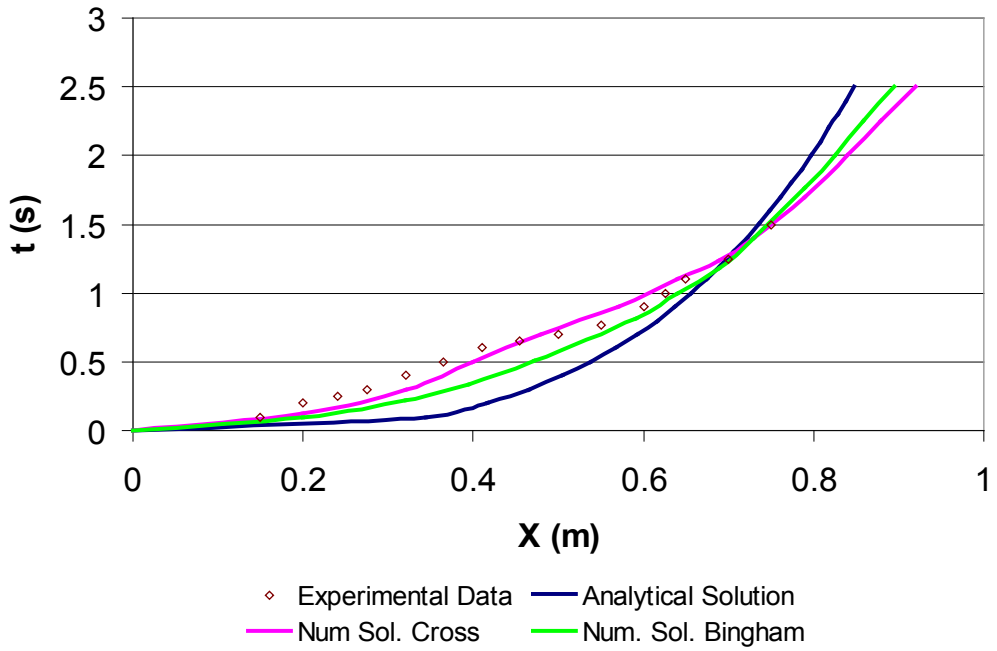

Figure 27. Spreading relation, comparison of numerical solutions with analytical solution and experimental data.

As time increases, the fluid velocity decreases, but the stoppage of the fluid is not totally reached with any of the numerical solutions. However, Bingham formulation tends to be more accurate than Cross formulation for later stages.

After a certain time, numerical solutions tends to increase and deviate from the analytical solution. This tendency is obviously caused by the numerical treatment of the wet-dry interface. Mesh refinement and the increment of the selective lumping parameter are able to reduce somehow the artificial diffusion presented in the wet-dry interface, but not to the extent that would be desirable.

Before different methodologies were studied in order to improve the solution in the profile front, other tests were performed to verify the effectiveness of the FEM solution. One of them was related with the analysis of a dam break problem, similar to the one discussed previously, but in this case over a wet slope, where a layer of fluid exists downstream from the mud-slide. This kind of test avoids the problem of the wet and dry interface and can focus the study in the accuracy of the FEM representation.

The analytical solution for wet-slopes is also presented by Huang and Garcia in his work of 1997, with some useful results for comparison. The downstream layer has a height h_2 equals to n times hy, where hy is the so called yield depth defined by

$$hy = \frac{\tau_y}{\rho g \sin\theta} \tag{80}$$

Figure 28 is a dimensionless plot of the wave shock depth (h_f/H) as a function of the shock coordinate (x_f/L), where H and L are the initial height and length of the triangular fluid source. The results are for λ=0.04, with $\lambda = h_y/L$, and for different values of h_2. The numerical solution, using FEM and Cross rheological model, shows an accurate approximation of the analytical solution in all the cases, which confirms the effectiveness of the FEM solution.

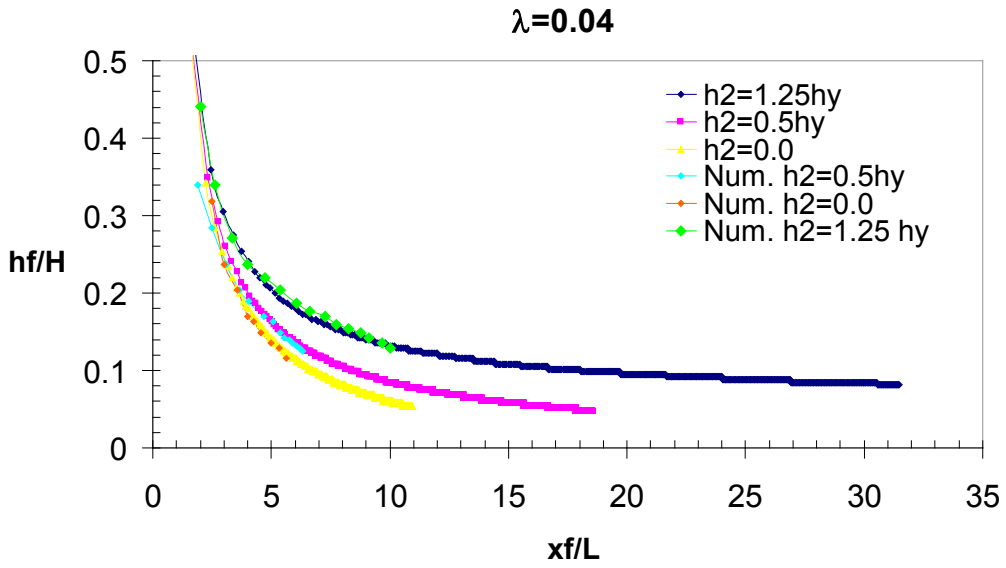

Figure 28. Kinematic-wave shock depth plotted as function of shock coordinate

Figure 29 shows free surface profiles at time 2.3 s on a wet slope, where h_2 equals 0.5*hy*. The FEM numerical solution, slightly smaller, is in very good agreement with the analytical solution.

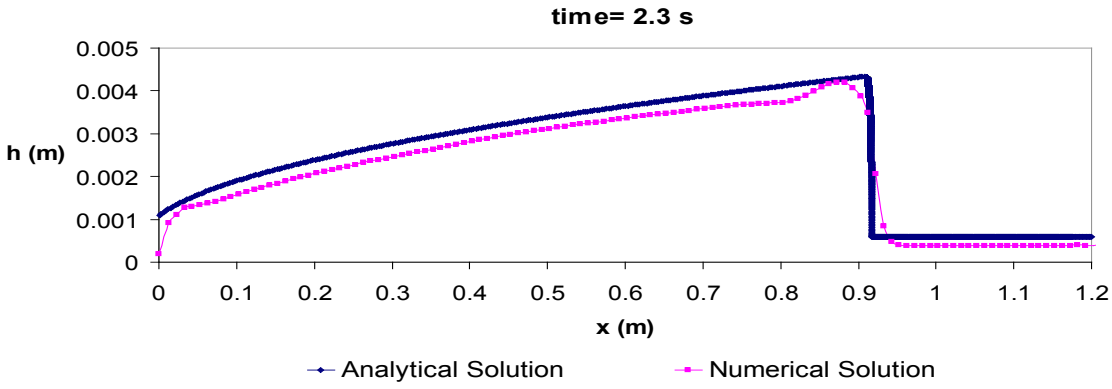

Figure 29. Free surface profiles on wet slope, h2= 0.5 hy. Numerical and analytical solution for time 2.3 s.

Similar analytical solutions were found in the literature for two-dimensional simple dam-break problems. These solutions were also used for verification of the FEM formulation.

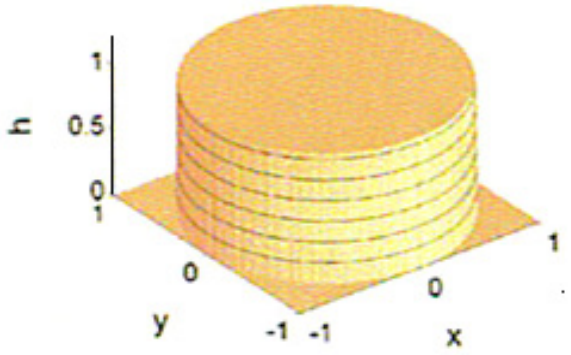

Figure 30. Two-dimensional dam break on a horizontal surface

Figure 30 shows a circular mud dam break on a horizontal plane, presented by Balmforth *et al.* in 2006. The initial condition of the problem is h*=h/H=1 for r*=r/L≤1, where H and L are the initial height and radius of the circular, confined, source of fluid. The dimensionless time t* is defined as

$$t^* = \frac{tL}{V} \tag{81}$$

where V is a characteristic velocity given by

$$V = \frac{\rho h H^3 \cos\theta}{\mu L} \tag{82}$$

with $\cos\theta = 1$.

The results are for a Bingham number (dimensionless yield stress) B=0.15, with B defined as

$$B = \frac{\tau_y H}{\mu V} \tag{83}$$

Figure 31 shows the results given by the Cross formulation (numerical solution) for the two-dimensional problem with initial conditions H = 3.2 cm, R = 16 cm, Cv = 26%. Comparing the profiles it is noticeable that the spreading of the numerical solution is larger than the analytical solution at advanced times; however, results are closer at short times.

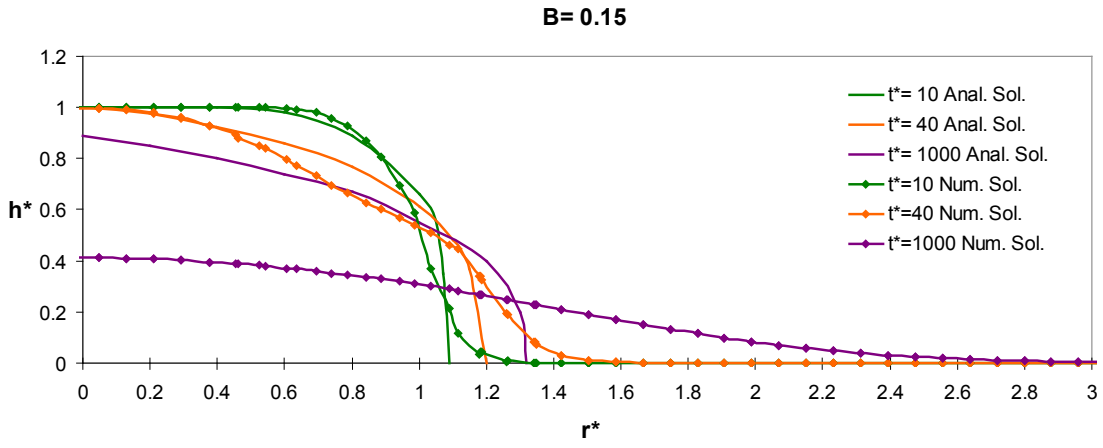

Figure 31. Axisymmetric dam break with initial condition h*=1 for r*<1. Numerical and analytical solutions for different times t*.

The numerical solution is stiffer than the analytical solution at early stages, but at the time increases, the spreading of the fluid is much larger with the numerical solution.

At this stage of the research it is known that some work has to be done in order to improve the wet and dry interface, in order to capture the discontinuity between wet

zones and dry zones. In addition, the solid phase has to be incorporated into the code to track the movement of large solid particles. These two issues will be assessed in the following sections.

4.1.3 Numerical Treatment of the Wet-Dry Interface

The capability of simulate the drying and wetting of the bed is crucial when solving mud dam-break problems. In this kind of events, most of the extension of the bed is initially dry and it gets progressively wet as the mud flow advances down the slope. Dry elements on sloping surfaces may cause numerical problems if handled incorrectly, because the gravity term in the governing equations can generate unrealistic flows when the bed surface is dry. Another major problem are the stress terms in the governing equations, this terms are divided by the fluid depth H. Dry elements has H equal to zero, which means that calculation over this elements will give non-defined results. In order to avoid these serious problems dry elements should be eliminated from the FEM calculation and the finite element mesh should be generated so that it will cover only the region that is expected to be wet.

The wet-dry algorithm implemented in this work is an improved version from one originally proposed by Kawahara and Umetzu (1986) and later proposed in the finite element context by Umetzu and Matsumoto (1999). The algorithm was developed and tested by Garcia *at al*. (2009) and it has been included successfully in many applications.

The wet-dry algorithm is as follows:

1.- At the beginning of each time step all elements are evaluated to see if they are wet, partially wet, or dry. A completely dry element is defined when all nodal depths are

less than a user-defined minimum depth or tolerance value H_{min}, that can not be zero in the case of mud-flows. A partially dry element has at least one node where depth H is less than H_{min}. A wet element has all nodal depths higher or equal than H_{min}.

2.- If the element is completely dry the governing equations for the element

$$\frac{\partial H}{\partial t} = \frac{\partial \overline{u}}{\partial t} = \frac{\partial \overline{v}}{\partial t} = 0 \tag{84}$$

These equations are discretized and solved using the finite element procedure described before. Also, for these dry elements velocity components are zet to zero for all nodes on the element.

3.- If an element is partially dry, the full equations are solved, but then velocities components are set to zero for all nodes on the element.

4.- Nodal depths are not modified for any element.

4.2 Solid-Phase Numerical Solution Verification

A computer program, based on the ideas of Graham G. W. Mustoe**,** Colorado School of Mines, was coded using Fortran 90 programming language to simulate the movement of the solid particles following the algorithm described in chapter 3. Several special cases were examined. These cases test the implementation of different force algorithms in isolation, as free motion, single contacts and multiple contact simulations.

Tests were performed using the canal described in Figure 16, with walls at the boundaries.

4.2.1 Test 1: Normal elastic force, vertical

To test for the particle-base interaction, the test simulates a free falling particle under gravity hitting the canal base. The canal is in horizontal position. Tangential forces and damping are set to zero. The stiffness constant used varies from 10^4 to 10^5 N/m. The particle, with radius 2.5 cm, is dropped from a height equal to 0.4 m.

Figure 32 shows the particle trajectories for two different stiffness constant, K1 = 10^5 and K2 = 10^4 N/m. The plot shows how the particle rebounds to its original height after each contact. There is no movement in the x-y directions, momentum and energy are conserved. Results are more accurate for the lower stiffness, this is related with the time step used. In order to improve results for K1 a lower time step should be used to allow more time stepts during time contact. Higher stiffness require the use of a lower time step.

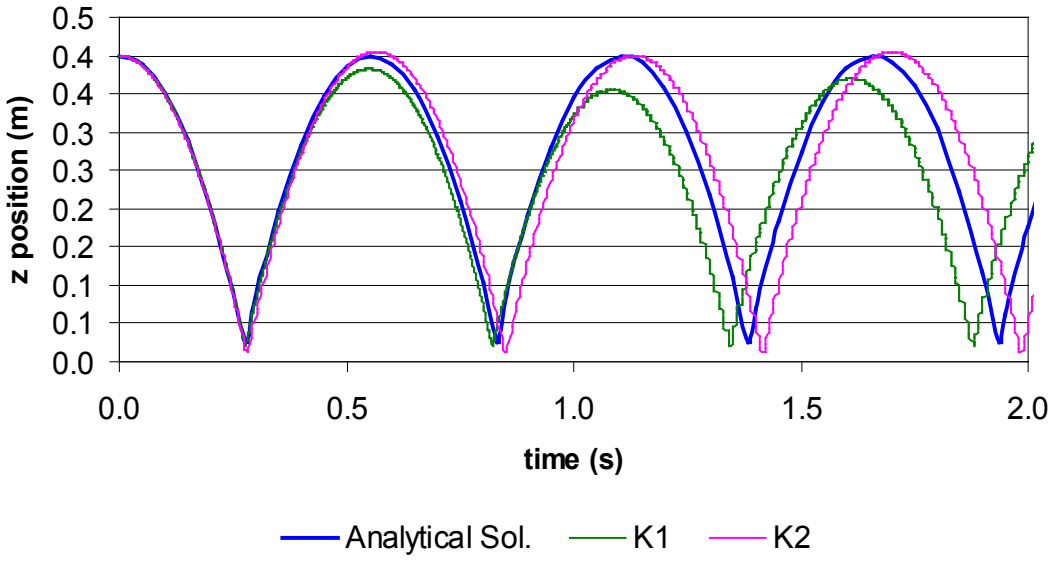

Figure 32. Test 1, *z* position of particle with time t

Figure 33 shows the particle velocity for the two different stiffness constant, K1 = 10^5 and K2 = 10^4 N/m. The plot shows how momentum is very well conserved after each rebound. Cinematic of the particle is not totally satisfied probably due to accumulation of numerical errors.

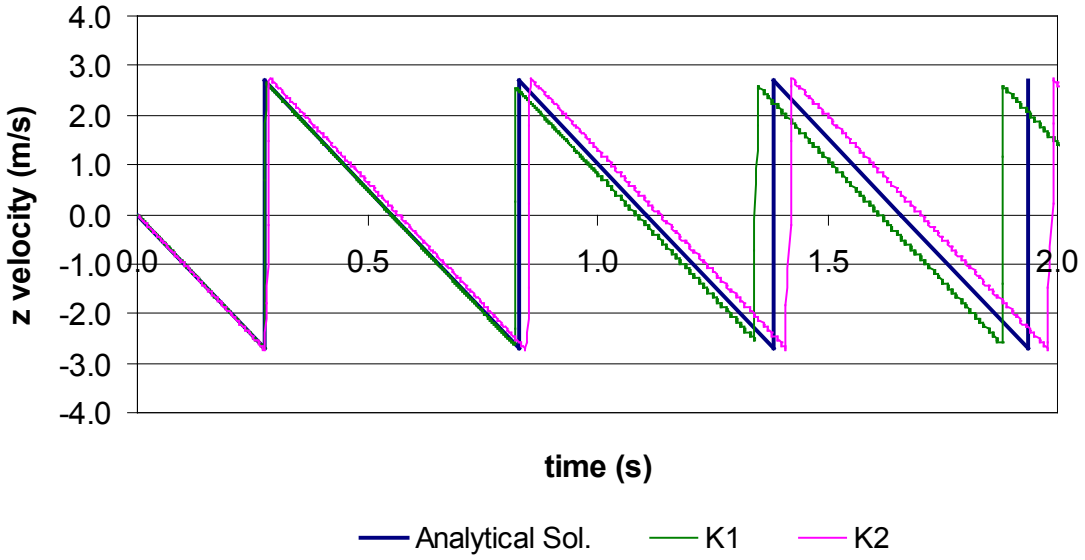

Figure 33. Test 1, *z* velocity of particle with time t

4.2.2 Test 2: Normal elastic force, horizontal

To test for the particle-wall interaction, the test simulates a particle moving with initial velocity in either *x* or *y* direction. Gravitational, tangential and damping forces are set to zero.

Figure 34. Test 2, schematic diagram

Figure 35 shows results for a particle with initial velocity in the y-direction. The initial velocity used is 0.45 m/s. Particle radius is 1.0 cm and the canal is 10 cm wide. Stiffness constant is set to K2 = 10^4 N/m. As can be seen, the particle rebounds horizontally between the two walls of the canal with no loss of energy. There is no movement in the x-z directions.

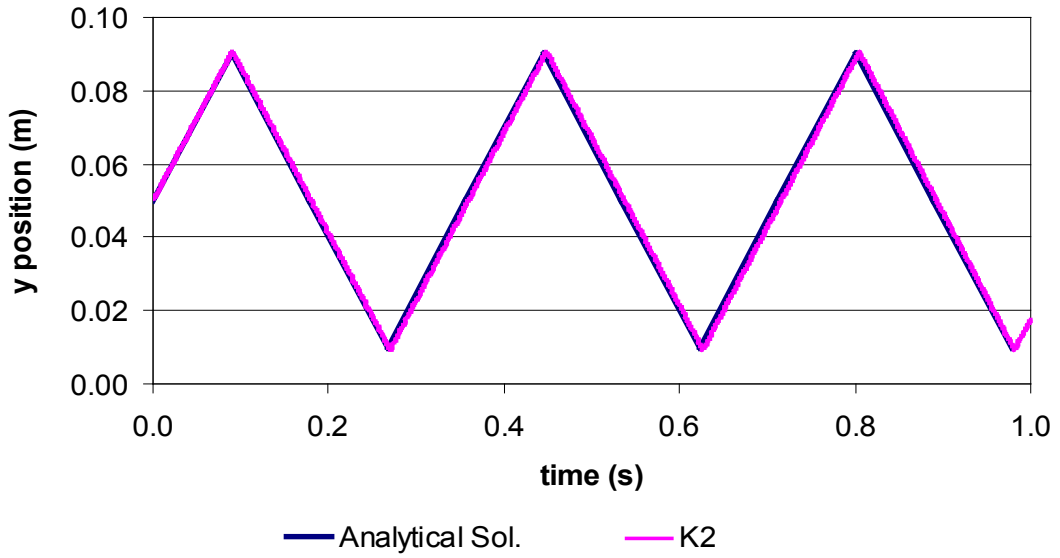

Figure 35. Test 2, *y* position of particle with time t

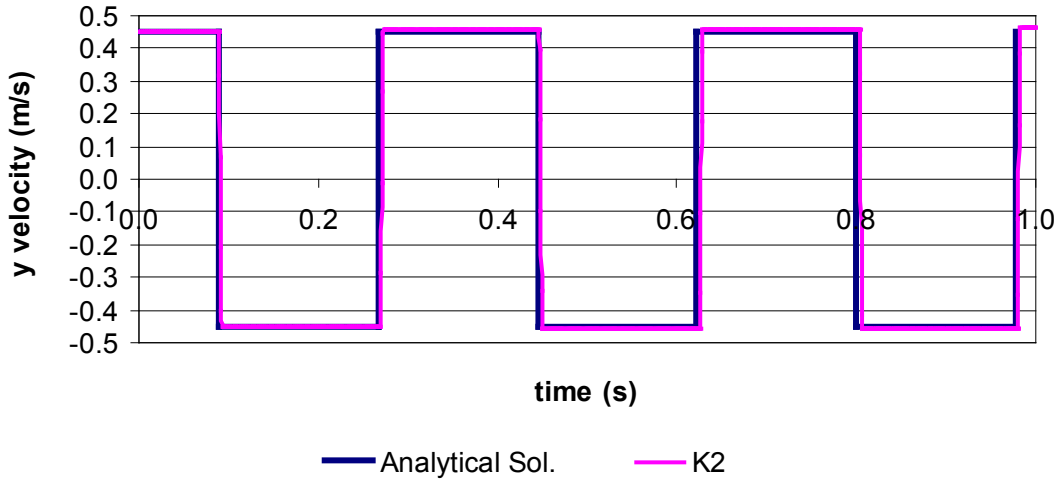

Figure 36. Test 2, *y* velocity of particle with time t

Figure 36 shows particle *y*-velocity variation, there is momentum conservation and particle cinematic is totally satisfied.

4.2.3 Test 3: Normal damping force

This test is identical to Test 1 but with the normal damping force accounted for. The normal damping coefficient E used is 0.8, which means that velocity after the impact must be 80% of velocity before the impact. Figure 37 shows how in this case, when the particle rebounds, it fails to reach the original height and its height decays along time due to damping. Figure 38 shows the decline in the normal velocity along time. Results show that in this case the numerical solution is very close to the analytical solution.

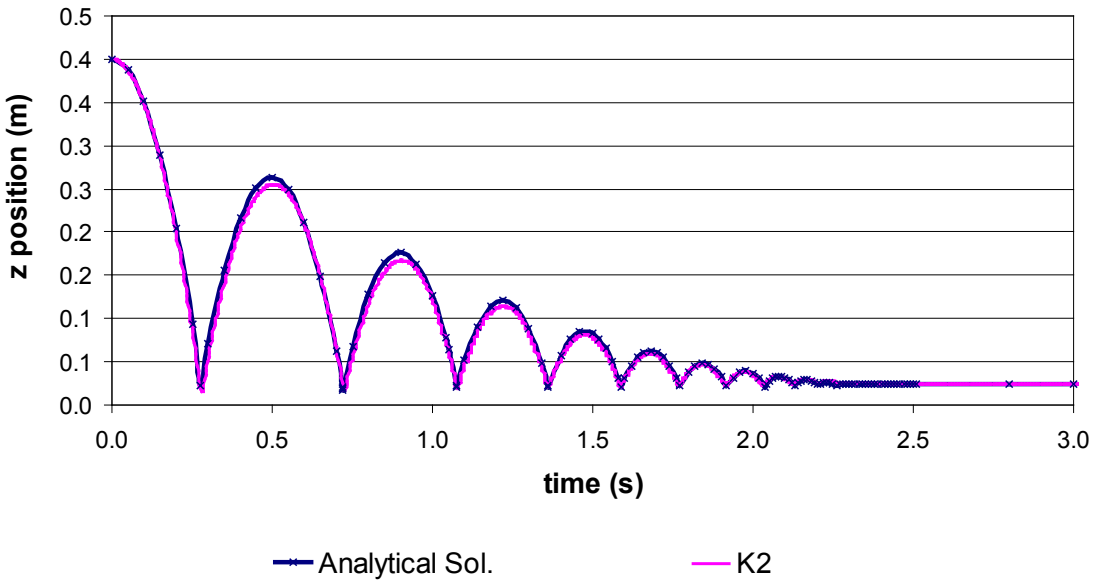

Figure 37. Test 3, *z* position of particle with time t

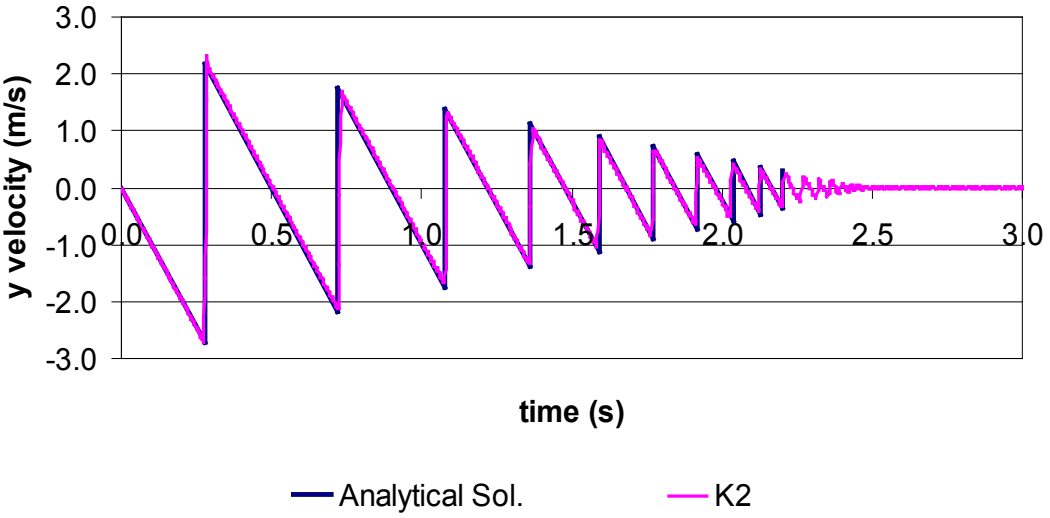

Figure 38. Test 3, z velocity of particle with time t

4.2.4 Test 4: Friction force, elastic

In this test, the elastic tangential force of the model is tested. Previous to gross sliding, this tangential elastic force keeps the particle in equilibrium when placed over an incline plane. No gross sliding occurs if $\mu_f = \text{Tan } \theta$.

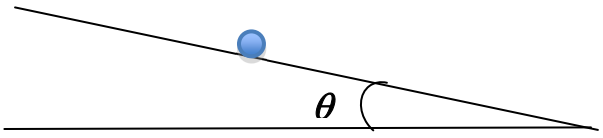

Figure 39. Test 4, schematic diagram

Gravitational, normal and damping forces were included together along with the friction force to show that particles will not move under the extreme condition $\mu = tan\ \theta$.

Figure 40 shows how the tangential velocity changes in a harmonic manner around the zero value, and declines over the time due to damping. Particles showed not noticeable movement down the plane.

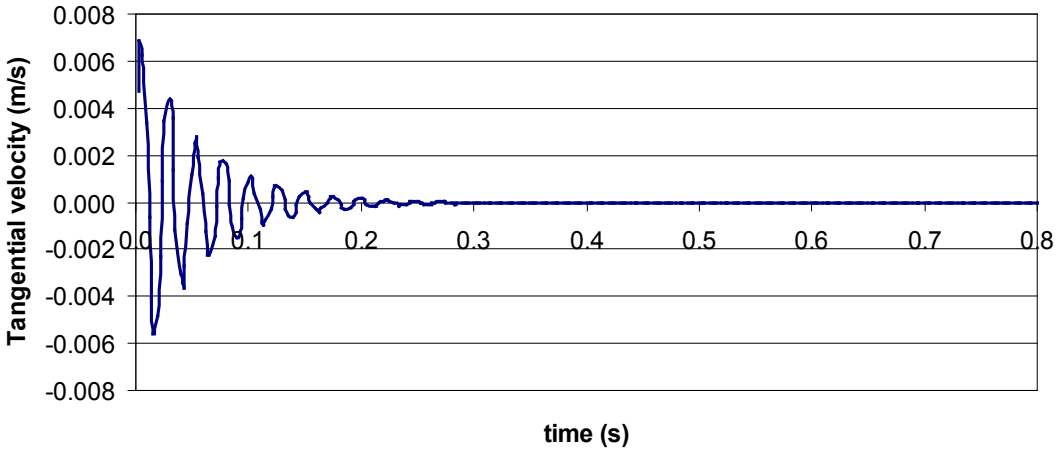

Figure 40. Test 4, particle tangential velocity with time t

The following slope angles and friction coefficients were tested using tangential linear stiffness ranging from 0.5 x 10^4 to 1.0 x 10^4, results were very accurate for all the range.

θ	μ_f
6^o	0.1
7^o	0.12
10^o	0.176
11.3^o	0.2

Table 1. Test 4, slope angles tested with corresponding limit friction coefficients

4.2.5 Test 5: Friction force, gross sliding

This test is similar to test 4, but in this case $\mu_f < tan\ \theta$, so the particle is able to slide over the incline plane. Solving particle equations of motion is known that

$$d = (\sin\theta - \mu_f \cos\theta)\frac{gt^2}{2} \tag{85}$$

then, distance along the plane could be obtained numerically for different times t to ensure analytical solution is satisfied. Gravitational, normal, damping and friction force were included. Normal stiffness constant is set to 10^5, tangential stiffness constant is set to 10^4, friction coefficient is 0.1 and slope angle equals 11.5^o. Results are in very good agreement with equation (85) as shown in Figure 41.

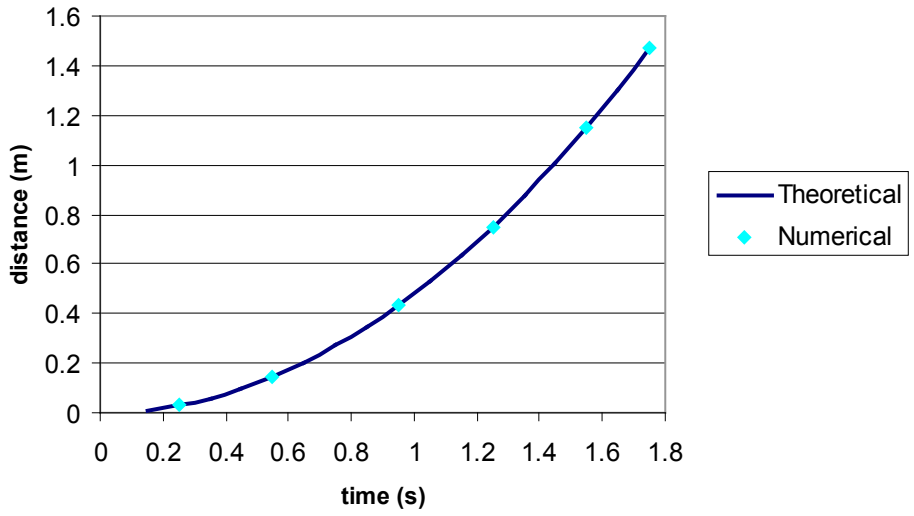

Figure 41. Test 5, distance traveled down the plane at time t

4.2.6 Test 6: Particle collisions, conservation of momentum

In this test one particle slides over the incline plane to then collide with two particles that are at rest over the horizontal plane. The test was first performed including gravitational and normal elastic force with no friction, then, second case includes friction force.

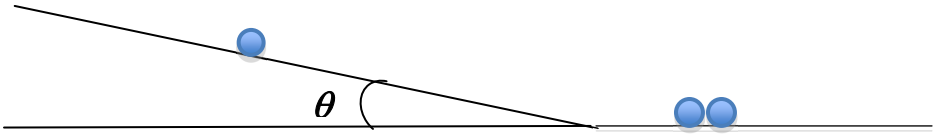

Figure 42. Test 6, schematic diagram

In the first case, at the time of collision, 0.592 s, V1 = 0.98 m/s. After collision V1 = -0.938×10^{-2} m/s, V2 = 0.254 m/s and V3 =0.736 m/s.

M1 = m V1 = m (0.98)

M2 = m V1 + V2 + V3 = m (-0.938×10^{-2} + 0.254 + 0.736) = m (0.98062)

Momentum is conserved.

In the second case, including friction with friction coefficient 0.1, collision occurs at time 0.838 s. V1 = 0.567 m/s just before collision. After collision V1 = -0.608×10^{-2} m/s, V2 = 0.150 m/s and V3 =0.420 m/s.

M1 = m V1 = m (0.567)

M2 = m V1 + V2 + V3 = m (-0.608×10^{-2} + 0.150 + 0.420) = m (0.56392)

Momentum is conserved.

Further tests were carried out to check momentum conservation in all directions. One example is shown in Figure 43 where the particle sliding over the incline plane

collides with two particles, in this case at the same distance in *x* direction. The example showed momentum conservation as well as perfect symmetry of movements on plane *x*-*y*.

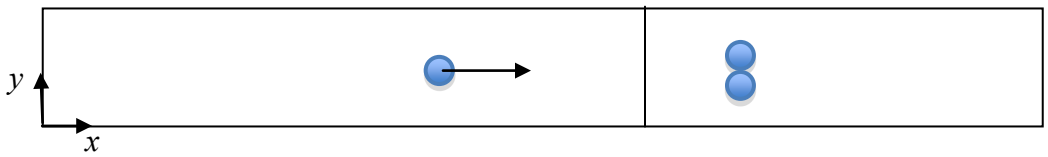

Figure 43. Test 6, example of momentum conservation

4.2.7 Test 7: Particle stacking, no overlap

This test simulates the free falling of five particles under gravity. The particles rebound over the incline plane and then collide with walls or among themselves until they reach equilibrium with velocities equal to zero. Particles, with radius 4.5 cm, are dropped from a height equal to 0.572 m. Vertical walls are situated at x = 0 and x = 1 m. The plane slope is 30^{o}. Gravitational, normal, damping and friction force were included. Normal stiffness constant is set to 10^{5}, tangential stiffness constant is set to 10^{4}, friction coefficient is 0.1 and restitution coefficient is 0.8. Figure 44 shows trajectory paths for all particles. Particles collide with bottom plane, walls and other particles with maximum overlap equal to 6×10^{-4} m. Equilibrium is reached with some staking as shown in Figure 45.

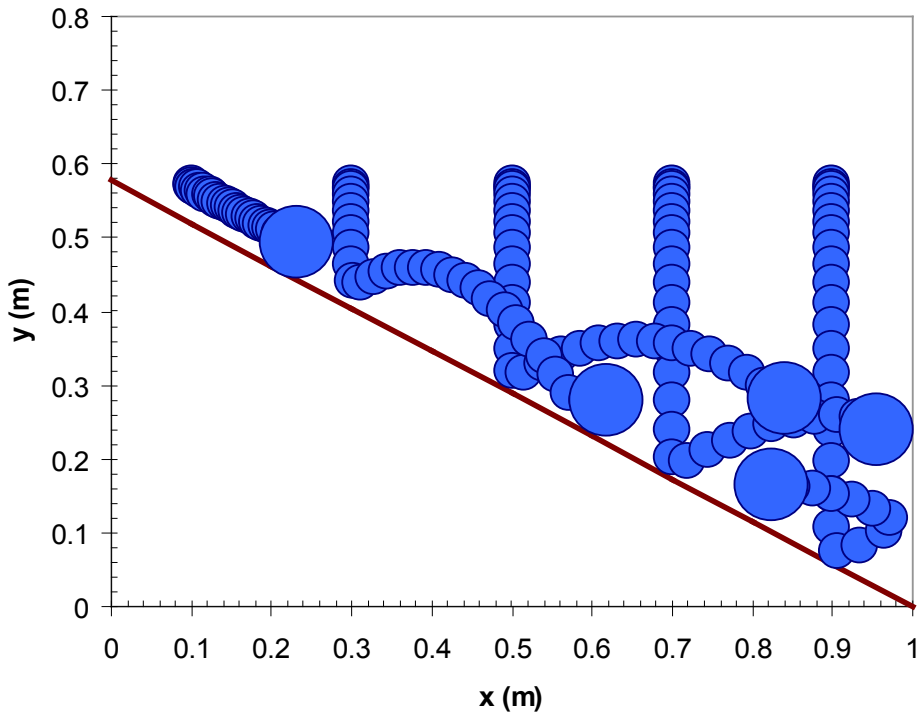

Figure 44. Test 7, trajectory paths for five free falling particles on an incline plane

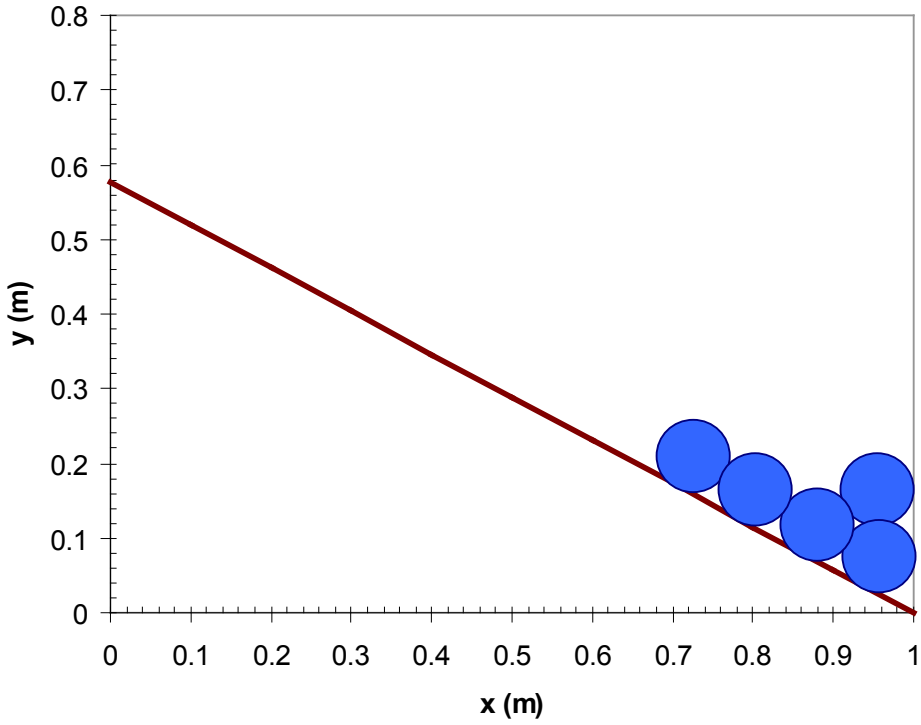

Figure 45. Test 7, particle final positions

4.2.8 Test 8: Particle terminal velocity, drag force

In this test, the drag force of the model is tested. The test simulates a free falling particle under gravity, but in this case immersed in fluid.

A free-falling particle achieves its terminal velocity when the downward gravitational force equals the upward drag force. This causes the net force on the particle to be zero, resulting in no acceleration.

As the particle accelerates downwards due to gravity, the drag force acting on the particle increases, causing the acceleration to decrease. At a particular speed, the drag force produced will equal the particle's weight. At this point the particle ceases to accelerate and continues falling at a constant speed called terminal velocity.

For a given particle of diameter d, the expression for terminal velocity, taking into account gravitational, buoyancy and drag force is as follows

$$V_t = \sqrt{\frac{4gd(\rho_p - \rho)}{3C_d \rho}} \tag{86}$$

In the test, the particle simulates a marble, with diameter d=2.5 cm and density ρ_p=2500 Kg/m^3. The fluid density is ρ=1390 Kg/cm^3 and viscosity is μ=0.162 Pa.s, in case (a), and ρ=1495.6 Kg/cm^3 and μ=0.740 Pa.s, in case (b).

Figure 46 shows how the z-velocity of the particle in case (a) increases in magnitude up to a constant value equal to 0.496 m/s. For this velocity, particle Reynolds number is R_{ep} = 106.4 and the drag coefficient is C_d = 1.1. Substituting the corresponding values in equation (86) the resulting terminal velocity is V_t = 0.49583 m/s. This result

means that the terminal velocity obtained numerically is the solution of the non-linear equation (86).

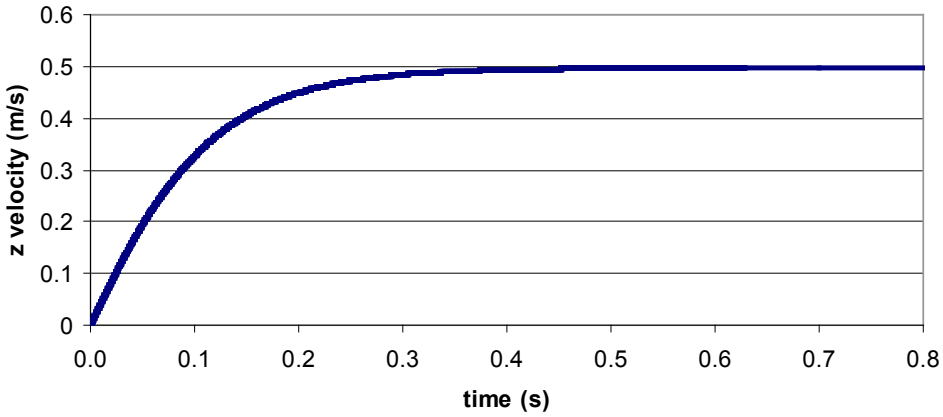

Figure 46. Test 8, case (a), absolute value of particle *z*-velocity with time *t*

Figure 47 shows the particle terminal velocity for case (b), equal to 0.249 m/s. For this velocity, particle Reynolds number is R_{ep} = 12.6 and the drag coefficient is C_d = 3.534. Substituting the corresponding values in equation (86) the resulting terminal velocity is Vt = 0.24896 m/s.

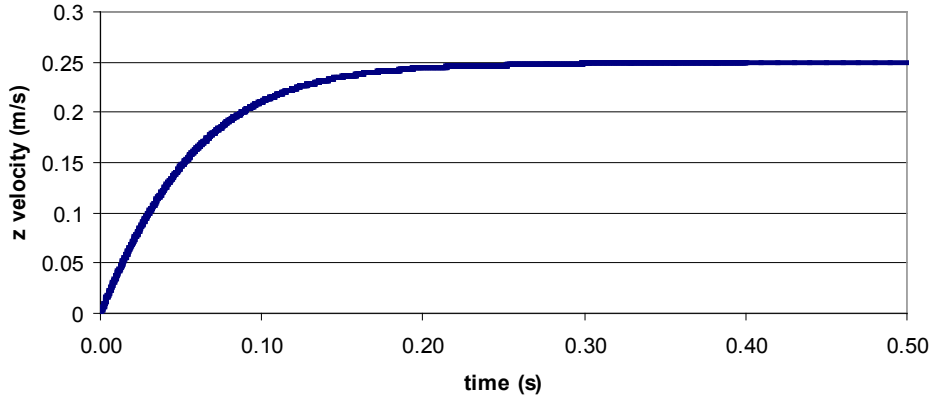

Figure 47. Test 8, case (b), absolute value of particle *z*-velocity with time *t*

After finishing these different tests it is concluded that the numerical model developed for the simulation of solid particles is ready to be incorporated in the main

program RiverFLO-2D. Verification of the computer program will go after using experimental results.

4.3 Model Pre-calibration using Experimental Data

A series of experiments were carried out in a laboratory channel using homogeneous mixtures and solid particles. The experiments were performed in a 1.9 m long, 0.19 m wide, Plexiglas walled laboratory flume, with adjustable slope. The downstream part of the flume was connected to a wood horizontal platform, 0.75 m long and 0.95 m wide as shown in Figure 48. A dam-break type of flow was initiated by releasing mixtures from a 0.40 m long reservoir situated on the upstream part of the flume. The release of mixtures was caused by an abrupt removal of a gate situated between the reservoir and the flume, Figure 49. The propagation of the fluid wave and the particle trajectories were filmed by two video cameras, one on the side and one on top of the flume.

Figure 48. Laboratory flume, Fluid Mechanics Institute, Universidad Central de Venezuela

Figure 49. Flume reservoir and gate, Fluid Mechanics Institute, Universidad Central de Venezuela

Water-clay mixtures were used in all the experiments, with volume sediment concentration from 18.0 % to 26.5 %. For preparation of the mixtures, kaolinite clay with specific unit weight of 2.77 was used. Density of mixtures was measured in the laboratory and rheological parameters μ and τ_y were determined using equations (9) and (10) in which α_1, β_1, α_2 and β_2 are $\alpha_1 = 0.621 \times 10^{-3}$, $\beta_1 = 17.3$, $\alpha_2 = 0.002$ and $\beta_2 = 40.2$. Rheological characteristics of experimental fluids are given in Table 2.

Cv (%)	ρ (Kg/m^3)	μ (Pa.s)	τ_y (Pa)
18.5	1330	0.0152	3.40
23.5	1410	0.0362	25.34
26.5	1460	0.0608	84.64

Table 2. Rheological properties of experimental fluids

4.3.1 Experiment 1

In this experiment the flow of a mixture of 23.5% volume concentration was studied. The flume bottom slope was set to 4^{o} and the initial volume released was 6.3 L. For t = 3 s the wave practically stopped flowing as shown in Figure 50.

The propagation of the wave was recorded for different times t to construct the spreading diagram showed in Figure 51. The canal was reticulated every cm to facilitate readings, Figure 52.

As shown in Figure 51, velocity of the front wave is practically constant up to the vicinity of the stopping point. The frontal wave velocity decreases progressively until the fluid stops.

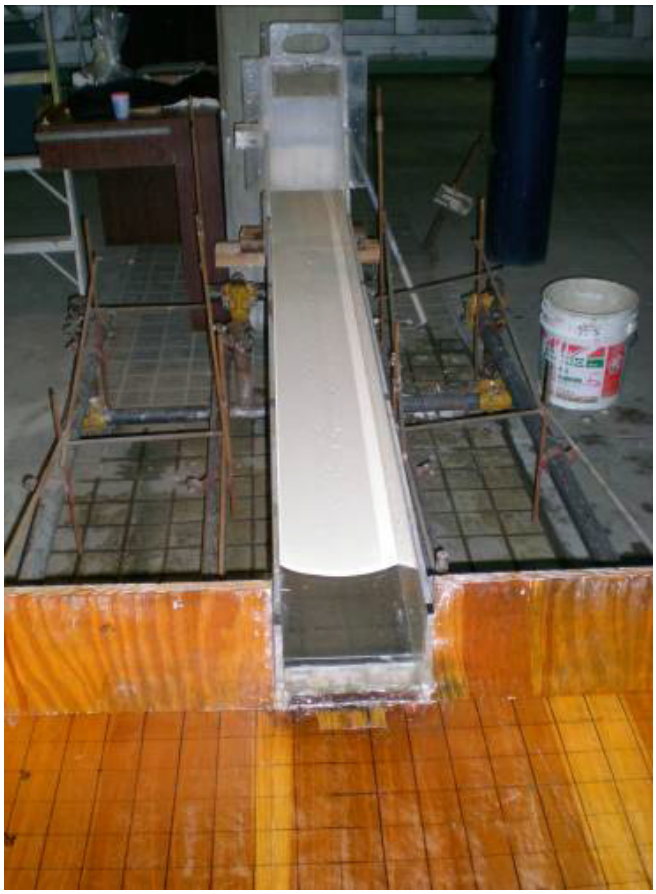

Figure 50. Experiment 1, fluid stops flowing over the sloping channel

Figure 51 compares the experimental data with the numerical solution using Bingham rheological formulation. Numerically, the condition of stopping the fluid is not easy to achieve; however, it is possible to appreciate how the maximum velocity in the fluid decreases with time and it becomes very close to zero about the time the fluid must stop. This fact shows that velocity criteria could be used numerically to stop the fluid.

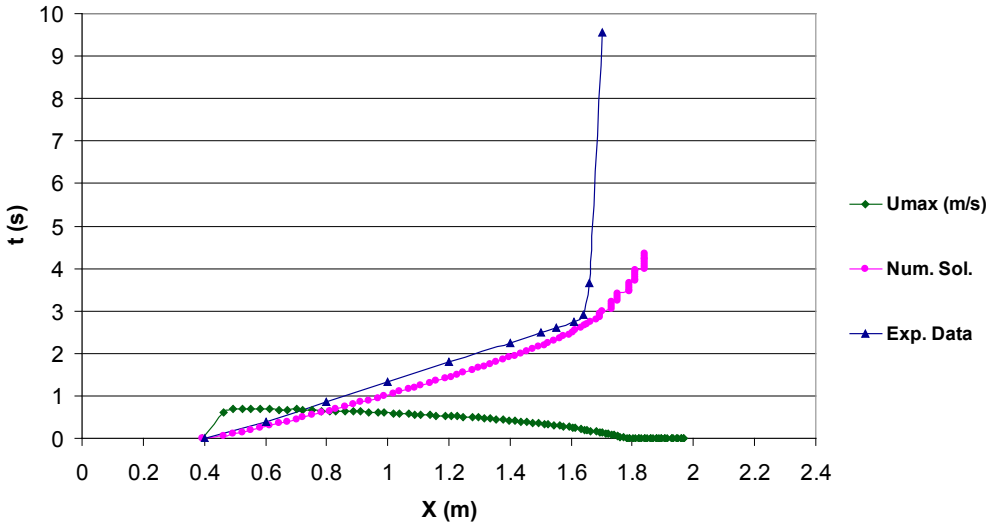

Figure 51. Experiment 1, spreading relation

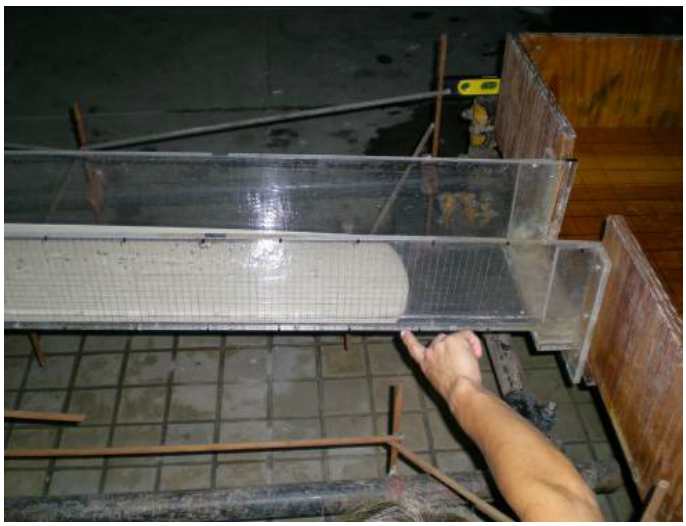

Figure 52. Experiment 1, measuring wave front position

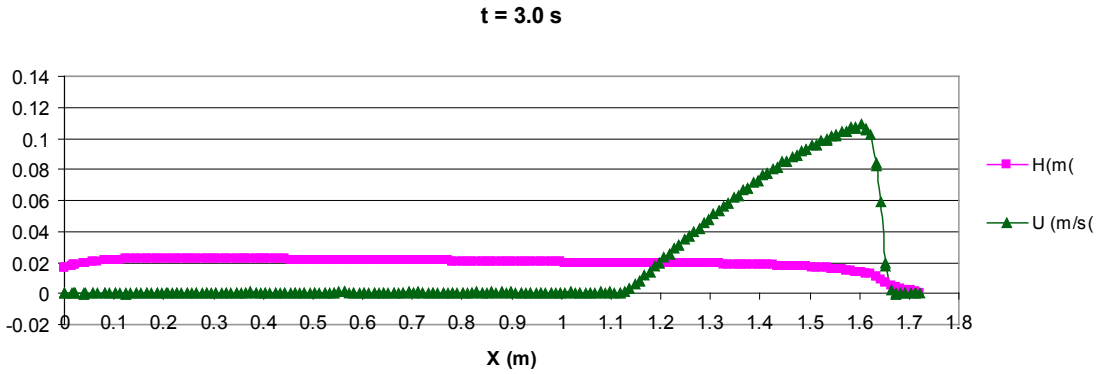

(a)

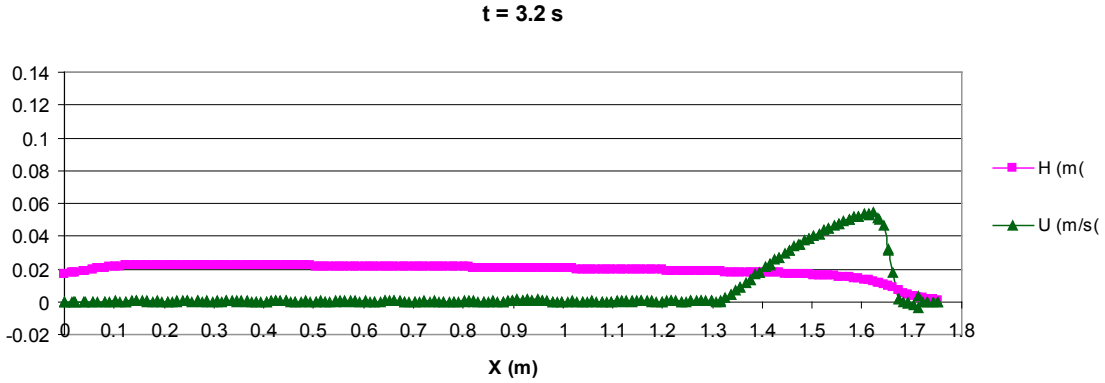

(b)

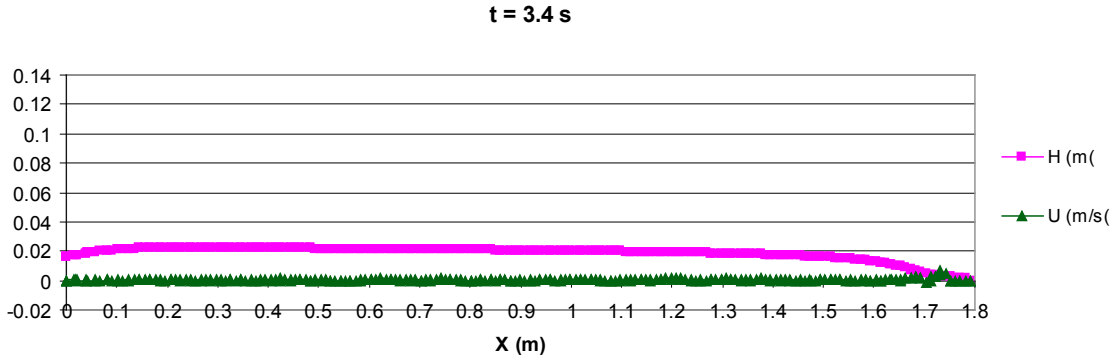

(c)

Figure 53. Experiment 1, free-surface longitudinal profiles and U_{max} value at time *t*

Figures 53(a) to 53(c) show free-surface longitudinal profiles for time 3 s and above. The figures also show how the maximum velocity value decreases progressively

to a value very close to zero, time when it is possible to consider the fluid wave should stop.

The final profile obtained numerically, is compared with the final profile measured at the laboratory flume in the following figure. This very good result was obtained implementing the wet-dry algorithm mentioned in previous chapter, using Bingham rheological formulation and using mesh refinement.

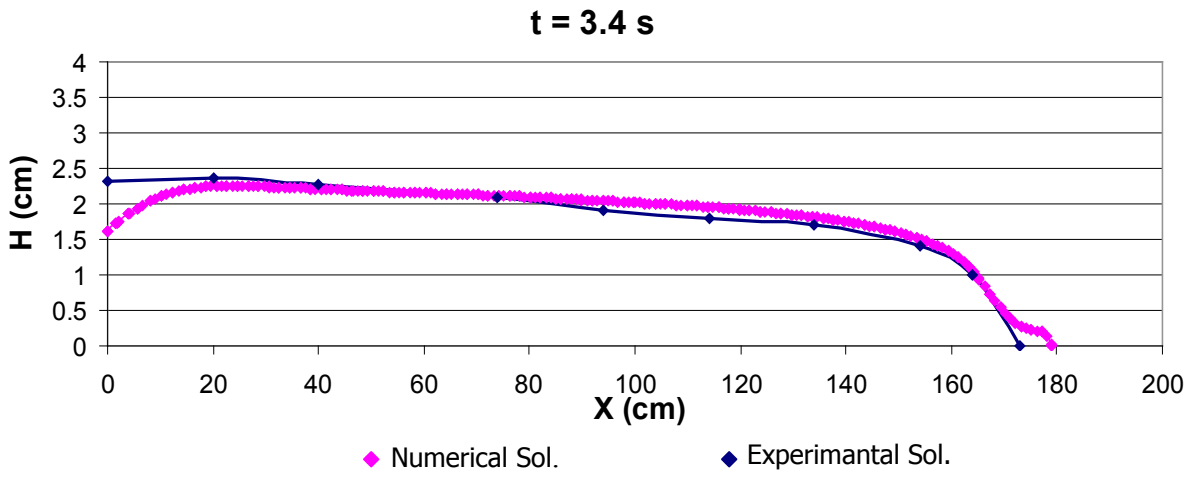

Figure 54. Experiment 1, final free-surface longitudinal profile

Figure 55 compares spreading relation and maximum velocity for old mesh (element size 3 cm) with the corresponding results using the new mesh (element size 1 cm). Results show great improvement when mesh is refined. The resulting spreading relation after refinement is more accurate than the one resulting with the old mesh.

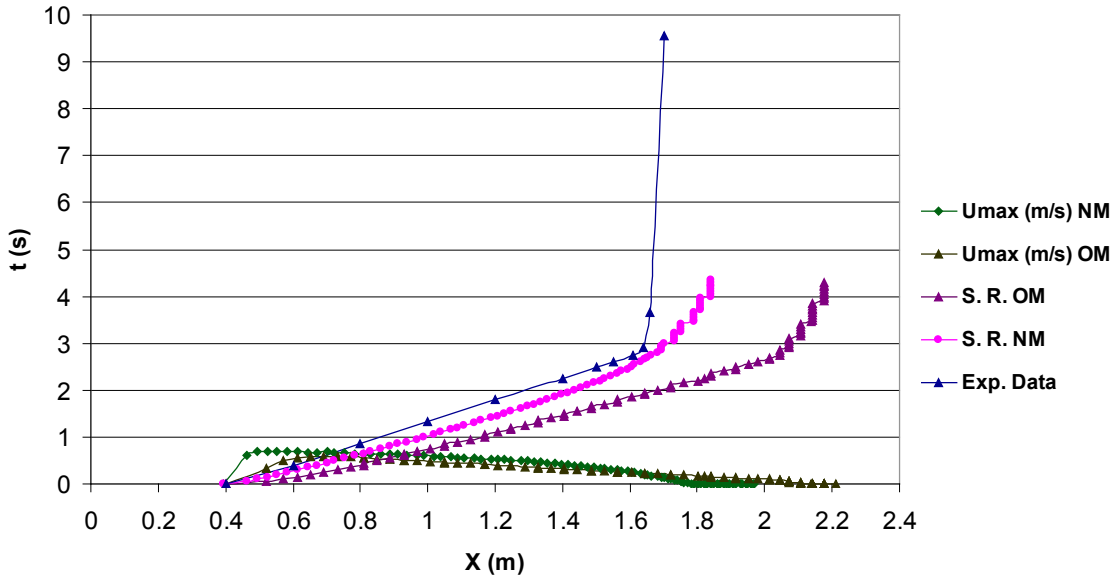

Figure 55. Experiment 1, spreading relation comparison, old mesh and new mesh

The following two figures compare longitudinal profiles and maximum velocity for the two different mesh sizes. As it is depicted in the Figures 56 (a) and 56 (b), the mesh refinement contributes to improve substantially the solution in the advancing front. The wet-dry algorithm implemented eliminates dry elements from the calculation, then there is a well defined interface between dry and wet elements.

However, there is a numerical tendency to form a front tail that is not real. This front tail can be reduced decreasing the element size as well as reducing the minimum height parameter, which makes the distinction between dry and wet elements. Best results were found with a minimum height or height tolerance equal to 0.01 times the average height of the fluid.

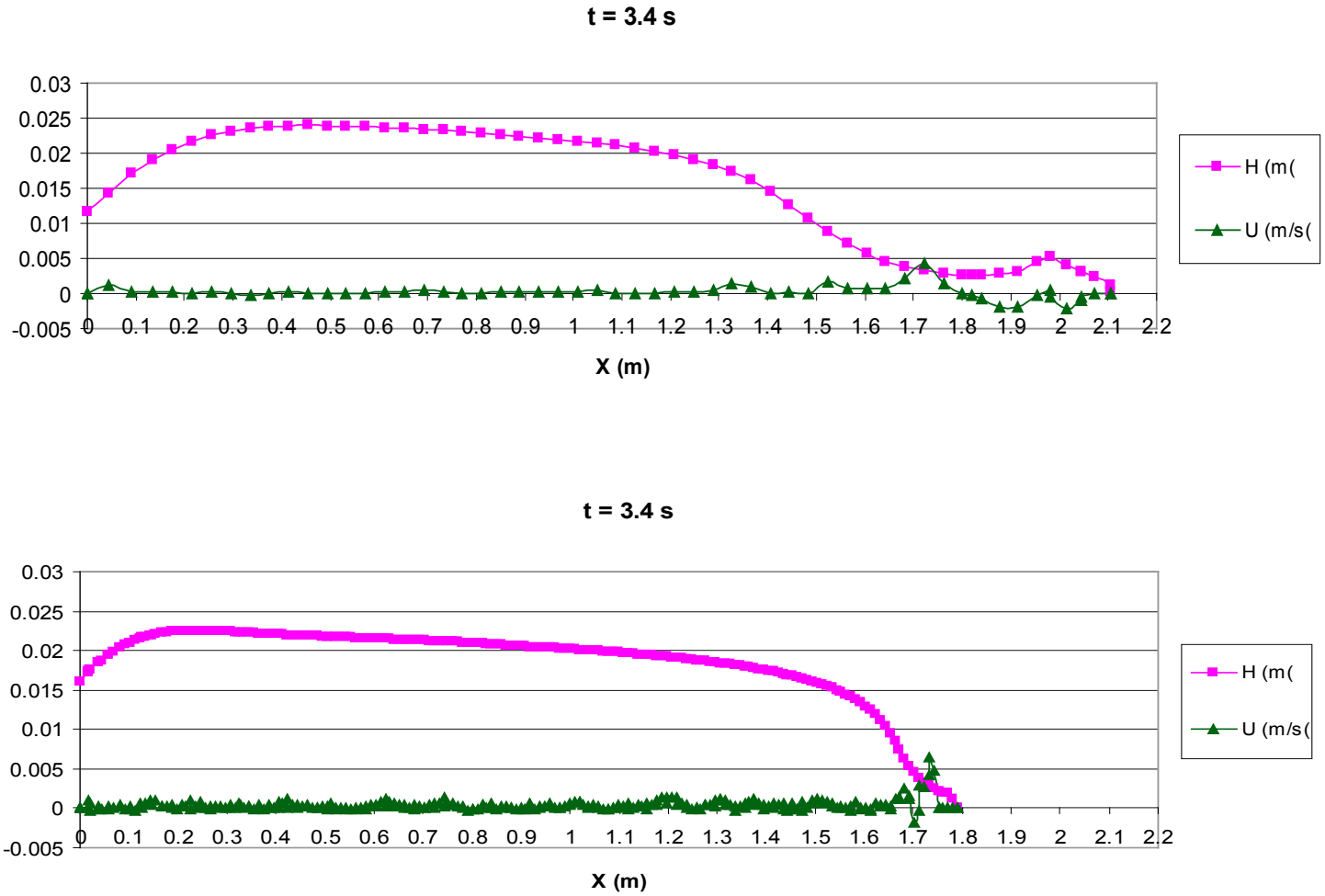

Figure 56. Experiment 1, final free-surface longitudinal profiles and U_{max}. (a) mesh size 0.03 m (b) mesh size 0.01 m

4.3.2 Experiment 2

The objective of this test was to study the spreading of the fluid in the fan, to verify the 2D fluid-phase formulation. In the lab, by time t = 1.5 s the front wave of the fluid had reached the end of the glass channel and it was entering into the horizontal platform. By time t = 2.4 s the mud stopped flowing forward, but continued flowing to the sides as shown in Figure 57.

(a) (b)

Figure 57. Experiment 2, (a) fluid at time 2.4 s. (b) fluid at time 8.4 s.

In this case, the flume bottom slope is 9.54^{o} and the initial volume released was 7.7 L. Figure 58 shows the spreading relation in the longitudinal direction for this experiment. The velocity of the front wave in the numerical solution is slower than the experimental velocity, however, the maximum velocity plot shows that by time t = 2.44 s the mud do not move forward anymore, as it was in the actual experiment.

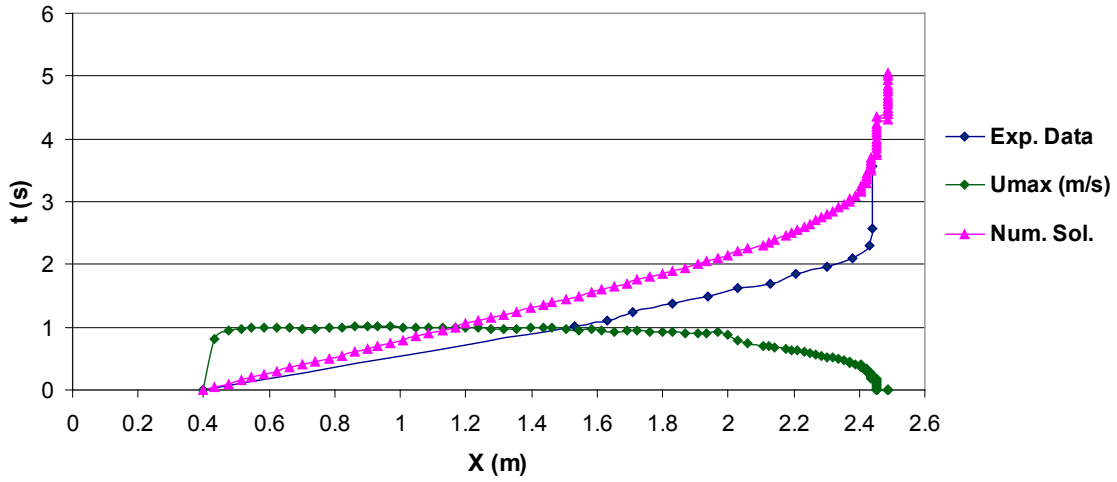

Figure 58. Experiment 2, spreading relation

Figure 59 shows how by the time t=7.25 s velocities along the longitudinal axis are very close to zero. Final free-surface profiles are compared in Figure 60 at that time. Numerical solution is in very good agreement with experimental results.

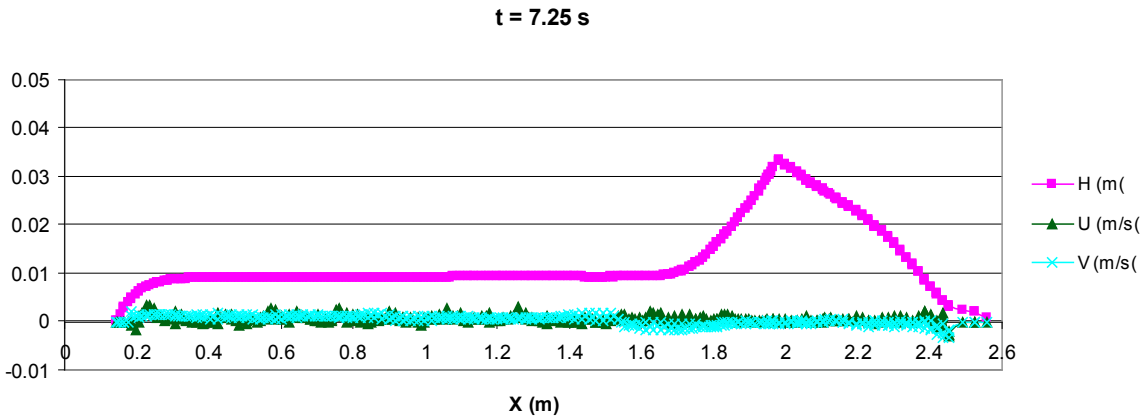

Figure 59. Experiment 2, free-surface longitudinal profile and U_{max}, V_{max} values at time t = 7.25 s

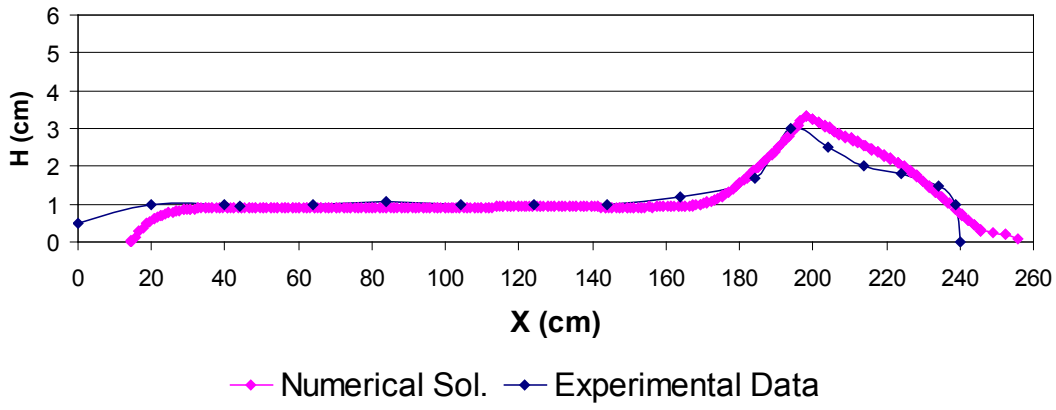

Figure 60. Experiment 2, free-surface longitudinal profiles at time t=7.25 s

Figure 61 shows a contour level map elaborated with height measurements done at the lab. It can be seen that maximum height (2.5 cm) occurs in the center just at the discharge zone of the channel. Figure 62 shows contour levels obtained numerically, in this case units are in meters. Comparing the two figures it can be appreciated that numerical results are very close to the experimental data.

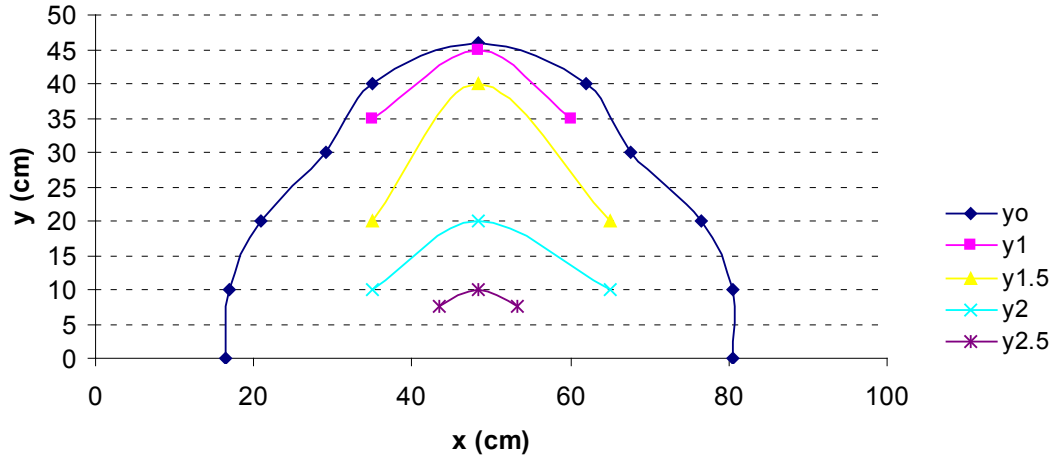

Figure 61. Experiment 2, experimental data, contour levels

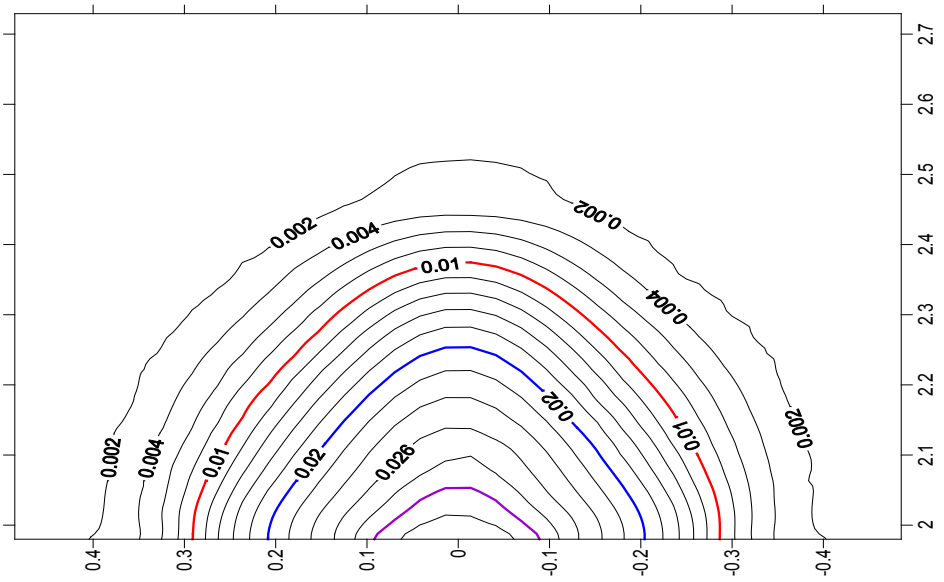

Figure 62. Experiment 2, numerical results, contour levels. Scales in m.

The following figure shows the contour level maps overlapped. It could be noticed the difficulty of modeling the front of the mud wave.

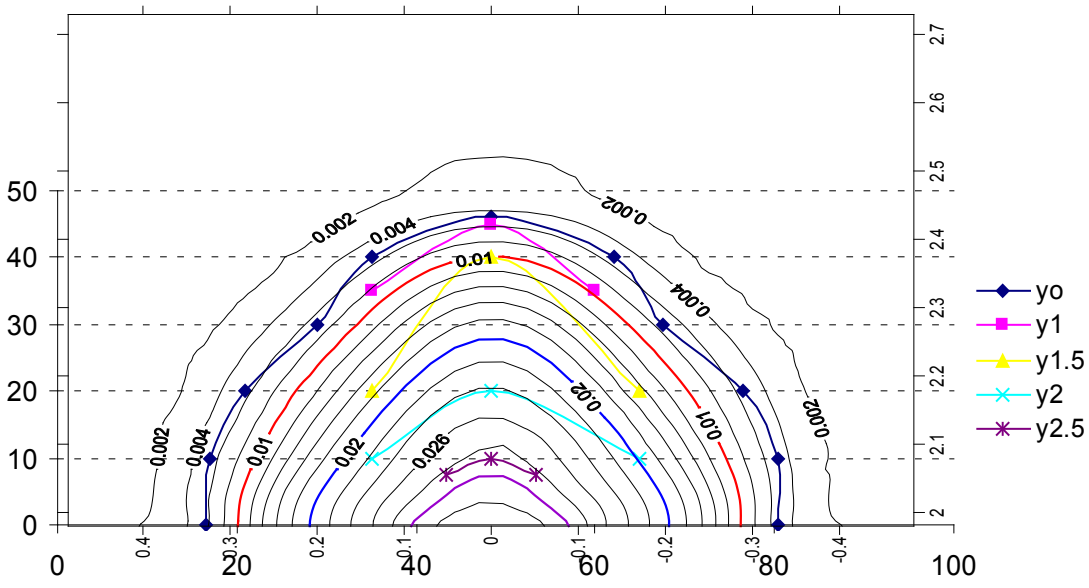

Figure 63. Experiment 2, comparison of experimental and numerical contour levels

Even though the wet-dry algorithm has clearly improved the front modeling, it is still a numerical diffusion problem that do not allow to have a fully representation of the front, as it is in Figure 64. This problem causes also difficulties for stopping the flow completely.

Figure 64. Experiment 2, wave front

4.3.3 Experiment 3

In this experiment the same mixture used in experiments 1 and 2 is utilized. In this case, the flume bottom slope is 9.54^{o} and the initial volume released was 6.4 L. The objective of this test was to study the spreading of the fluid in the fan and to study particle movement into the fluid.

14 particles, D = 2.5 cm and ρ_p = 2500 Kg/m^3, were placed over a small piece of wood inside the mud reservoir, just behind the gate as shown in Figure 65(a). By the time the fluid was released, the piece of wood was quickly removed, so the particles could start their movement along the channel with the fluid.

Particles depicted clearly the velocity profile shape at early times during the experiment; however, as the flow progressed down-stream, particles tended to move to the channel sides. The following plots shown the sequence of the events obtained numerically.

(a) (b)

Figure 65. Experiment 3, (a) initial position of particles, (b) final position of particles

Figure 66(a) shows the particles resembling the velocity parabolic distribution across the channel; then, the following figures shows how particles become disorganized. It can be noticed how particles in the center tend to move forward to reach the front of the wave, particles in the second row displace particles in the first row to the sides and these are then left behind because of the fluid velocity gradient. By the time the flow reached the fan, particles moved to the sides of the flow as it is shown in Figure 65(b).

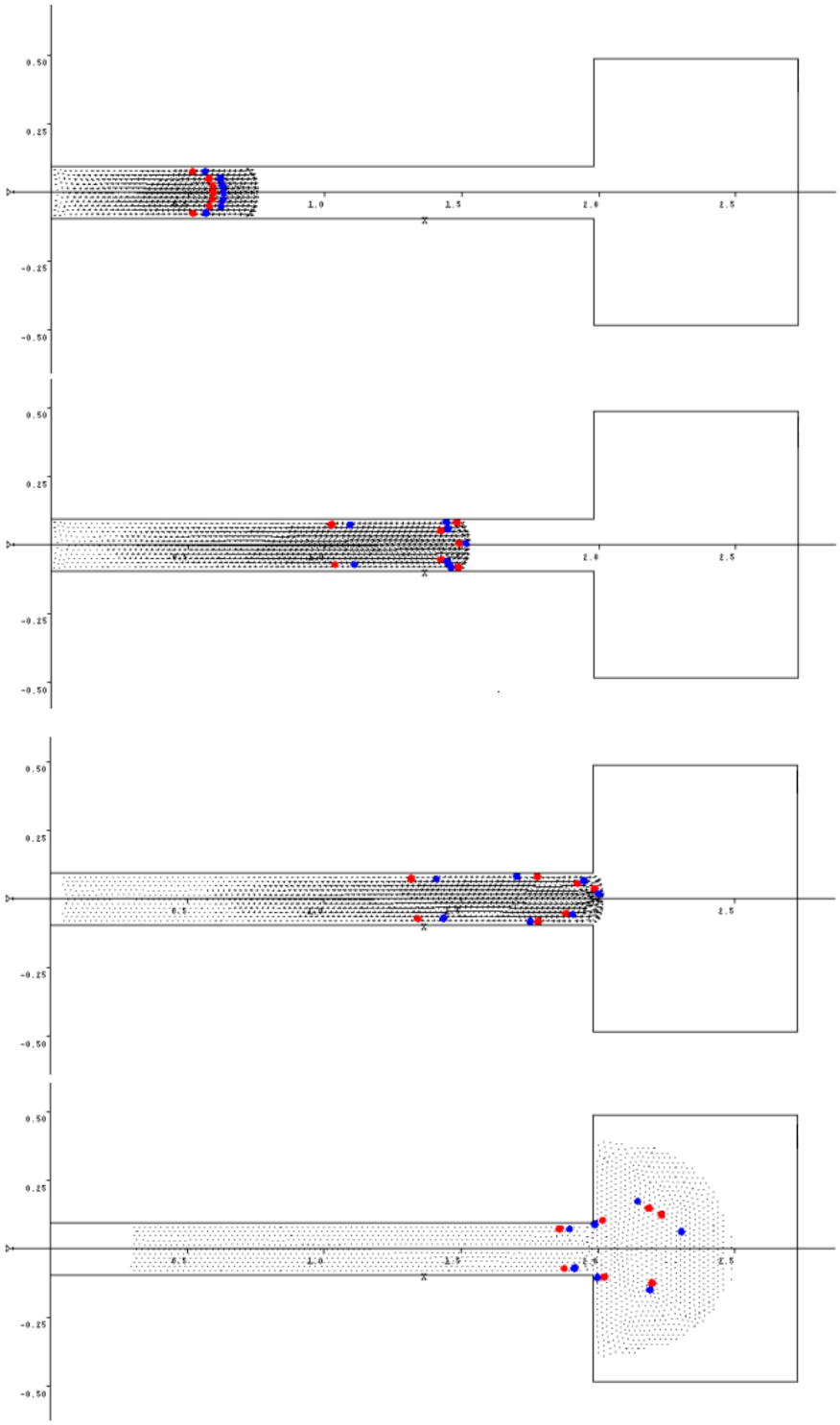

Figure 66. Experiment 3, (a) t = 0.5 s, (b) t = 1.6 s, (c) t = 2.4 s, (d) = 6.5 s

At this point it is important to mention the effect of the boundary condition for velocity on the sidewalls. Strictly speaking this condition should be a no-slip condition so $\vec{u} = 0$ at the wall. However, in reality, the velocity gradient near the wall is large and the velocity near a wall quickly becomes non-zero. Therefore, in practical application of the model the no slip condition formulated in finite elements becomes very restrictive, basically causing unrealistic delay of the flow. Up to this simulation, the no-slip condition has been replaced by a weaker condition, impermeability $u_N = 0$, and tangential velocity $u_T = 0.9(\vec{u} \cdot \vec{t})$. If a total slip condition is imposed, then no velocity profile across the channel would be resembled, that is the reason of using a boundary condition coefficient $BC_{coef} = 0.9$. This parameter was calibrated when performing simulations of previous experiments. When working with particles this parameter is also very important, in this case it could be seen that there exist some delay on the particles positioned close to the walls; however, higher values for this coefficient would cause non real results, as shown in Figure 67, when a fully slip condition is imposed $u_T = 1.0(\vec{u} \cdot \vec{t})$.

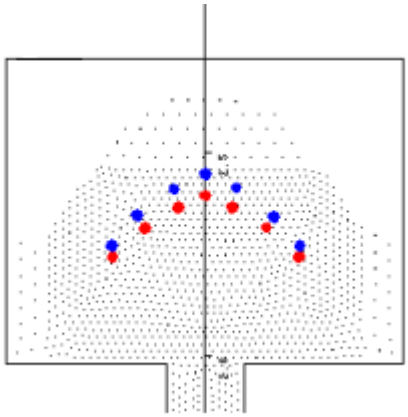

Figure 67. Experiment 3, final position of particles, numerical sol. 100% slip boundary condition

Figure 68 compares final position of particles obtained numerically, using the constant equal to 0.9, with final position of particles measured at the lab.

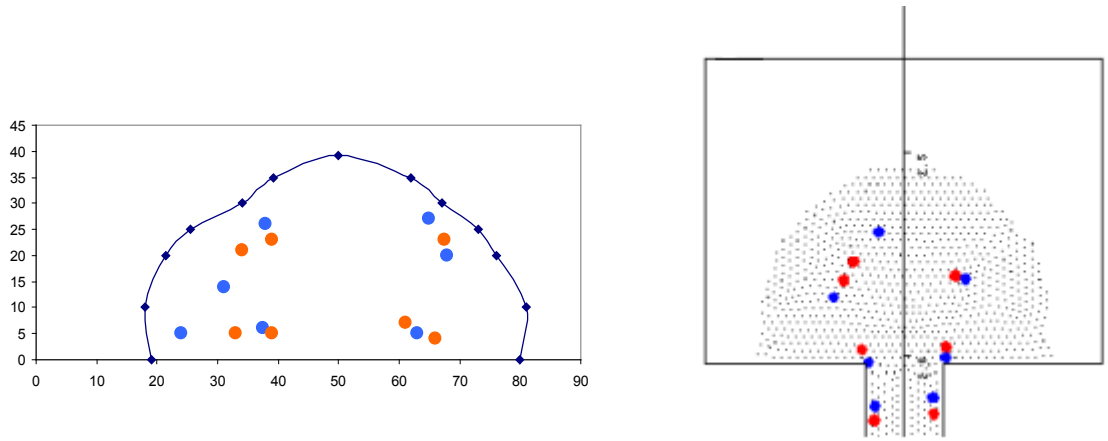

Figure 68. Experiment 3, final position of particles, (a) numerical sol. 75% slip boundary condition, (b) experimental data

The plots exposed in Figure 70, show velocity transversal distribution and flow depth for a section A situated at 2.08 m from the canal up-stream end, see Figure 69 as reference. The plots were obtained numerically for different times *t*.

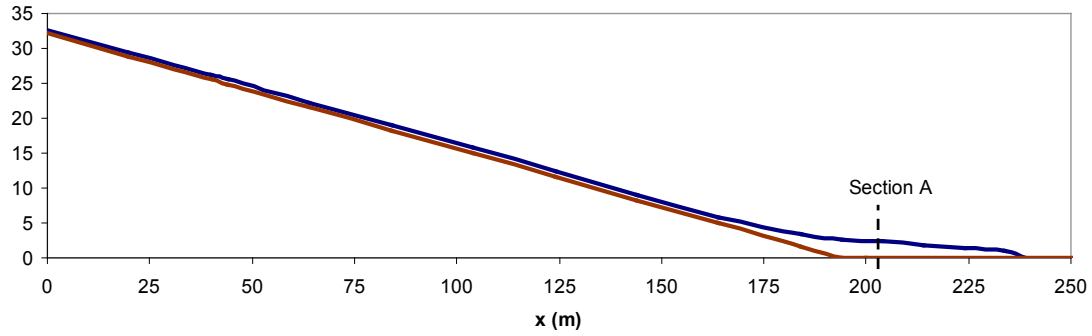

Figure 69. Experiment 3, final flow profile over the channel, section A located at x=2.08

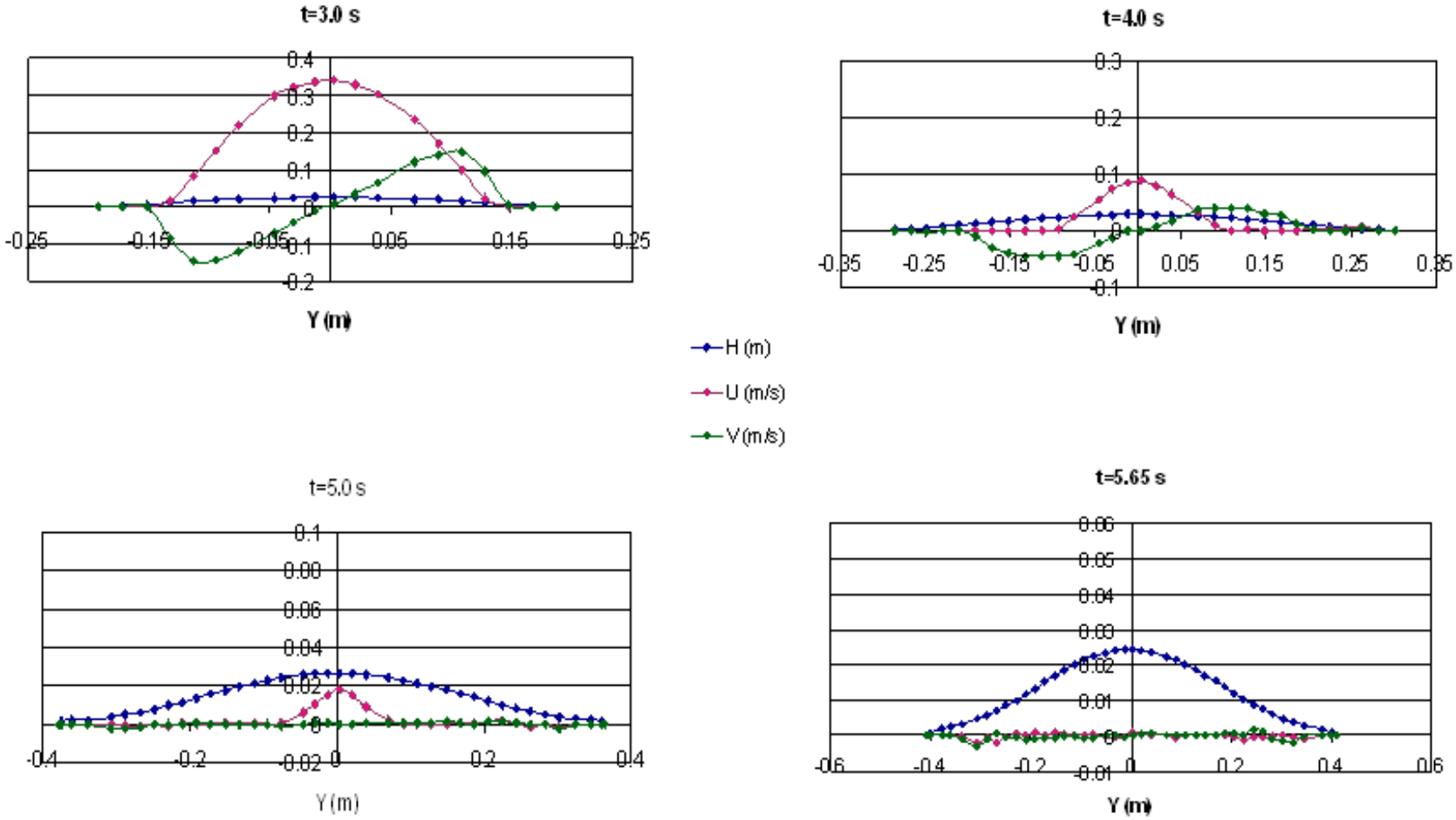

Figure 70. Experiment 3, velocity distribution and flow depth for section A located at x=2.08 m

The figures show how velocity *u* distribution is parabolic and decreases with time, from the sides of the flow to the centerline. On the other hand, transversal velocity *v* decreases with time from the centerline to the sides and distribution is anti-symmetrical, as can be expected. The last figure shows the final depth of the fluid in that section with velocities very close to zero.

4.3.4 Experiment 4

In this experiment a mixture of concentration 26.5% was studied. In this case, the flume bottom slope was increased to 10.7 ^{o} and the initial volume released was 11.1 L. The objective of this test was to study the spreading of the fluid and study particle movement into a mixture with higher clay concentration. Figures 71 (a) and (b) show pictures of the experiment when the flow reaches the fan.

Figure 71. Experiment 4, (a) t = 20 s, (b) t = 40 s

In this experiment, the velocity of the front wave is basically constant until reaching 1.6 m, from this point the celerity of the wave decreases abruptly, taking about 40 s for the fluid to stop completely.

Figure 72 shows the spreading relation in the longitudinal direction for this experiment. This relation is compared with numerical results obtained using Bingham rheological model and using Cross rheological model.

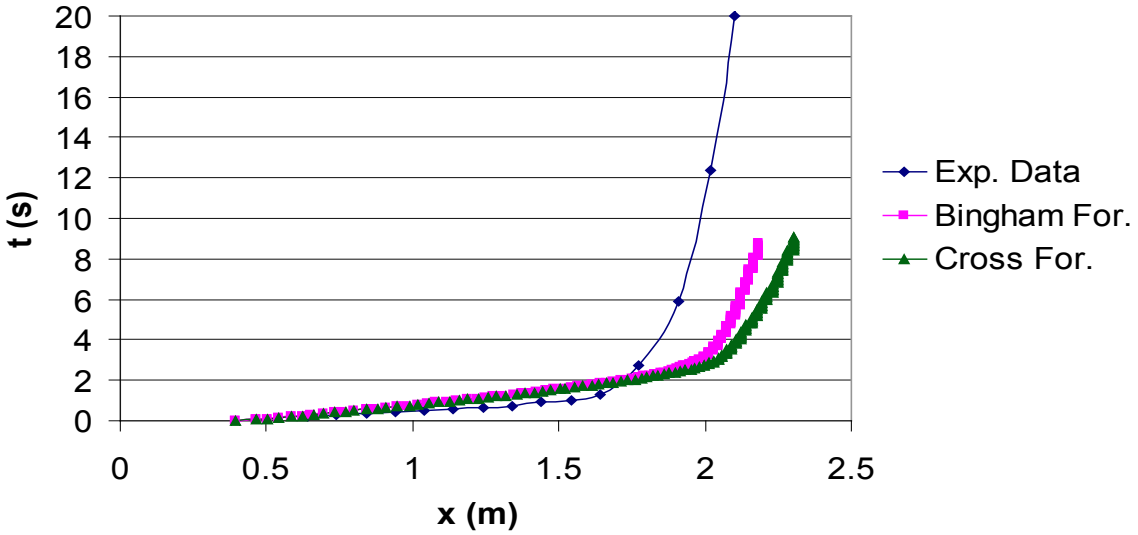

Figure 72. Experiment 4, spreading relation

The figure resumes what can be appreciated during all the simulations. Both rheological formulations produce very similar results, they are not totally capable of resembling the spreading of the flow; however, they show a final fluid extend, when velocities in the fluid become very close to zero, very similar to the real one. Bingham formulation shows to be more effective in decreasing the velocities along the fluid to zero. Figure 73 shows the final profile obtained at time t=10 s using Cross formulation. Results show that the final profile using the velocity criteria is very similar to the one measure in the lab.

In this experiment 14 particles were placed on the fluid in a similar manner that was done in the previous experiment. In this case, particles depicted the velocity profile shape at early times of the experiment; and as the flow progress down-stream, particles

tended to keep the parabolic distribution. Particles close to the walls were kept some behind.

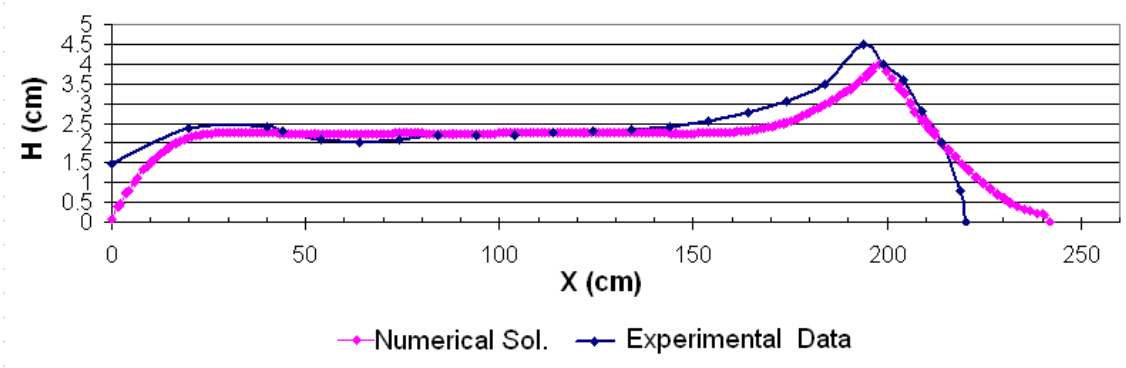

Figure 73. Experiment 4, final fluid profile, numerical and experimental results

The following plots shown the results obtained numerically. Figure 74(a) shows the particles resembling the velocity parabolic distribution across the channel; then, the following figures show how particles progress with a similar distribution along the channel. This fact can be appreciated in pictures shown in Figure 71.

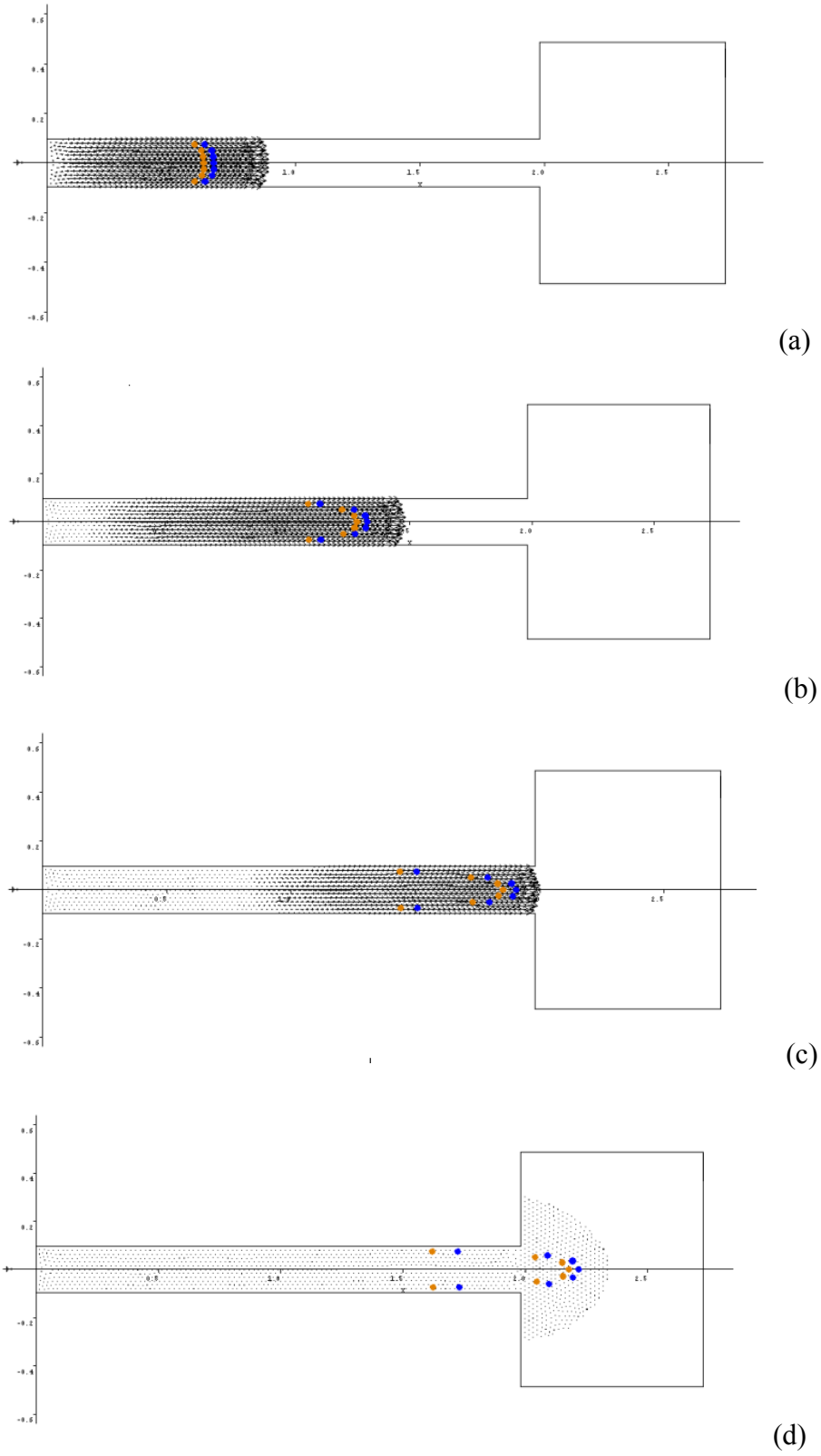

Figure 74. Experiment 4, (a) t = 0.5 s, (b) t = 1.5 s, (c) t = 3.2 s, (d) = 9.0 s

Figure 75 compares final position of particles obtained numerically, using 75% of slip boundary condition, with final position of particles measured at the lab. It can be observed that particles on the sides are left behind in both cases, more openly in the experimental case.

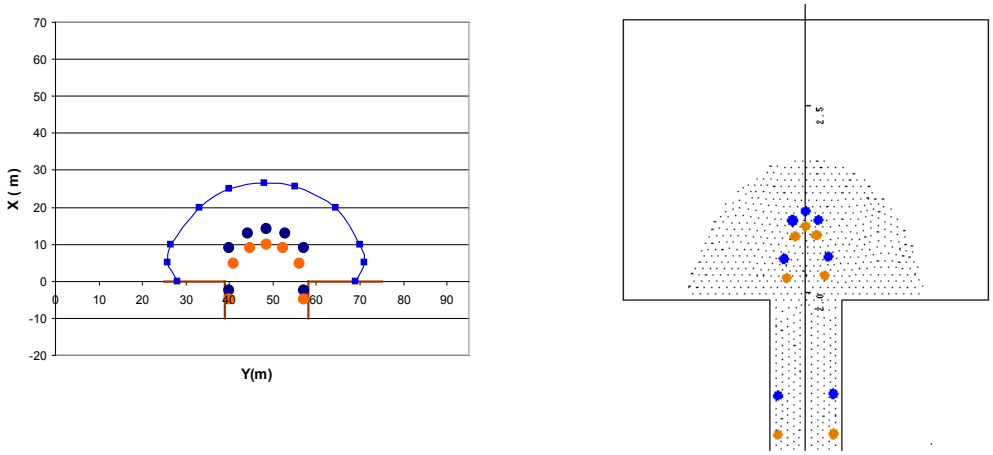

Figure 75. Experiment 4, final position of particles, (a) experimental data, (b) numerical sol. 75% slip boundary condition

4.3.5 Experiment 5

In this experiment the mixture of concentration 23.5% was studied. The flume bottom slope was set to 10.7 ^{o} and the initial volume released was 6.8 L. The objective of this test was to study the movement of several particles with different sizes into the fluid. In order to do that, 20 particles, D = 2.5 cm and ρ_p = 2500 Kg/m^3, and 50 smaller particles with D = 1.6 cm and ρ_p = 2500 Kg/m^3, were place randomly into the fluid reservoir before the fluid was released.

Figures 76 (a) and (b) shows the flow of mud and solid particles at two different stages of the experiment. Particles are dispersed along the fluid with a little higher concentration at the front. Some small particles remained at the channel upper part while

larger particles moved downwards; however, as it is depicted in figure 77, there was no accumulation of particles in the fluid front, as it could be expected.

Figure 76. Experiment 5, (a) flow frontal wave, (b) flow of mud and solid particles

Figure 77. Experiment 5, final extend of the flow and particle positions

The following figures shown the results obtained numerically for experiment 5. The same mixture and amount of fluid was used in the simulation, the same amount and

type of particles too, however; the same initial position of particles was not possible to resemble exactly. The particles were placed randomly in the fluid before the simulation started, as we did in the lab. Figures 78(a) to 78(d) show the particles as they move downstream with the fluid. Figures show some important facts:

- Particles do not overlap.
- Particles do not collide in such a way they can be placed out of the fluid.
- Large particles reach the channel down-stream, some of them never entered into the fan.
- Some small particles remained in the channel, stuck in the fluid.
- Some large particles formed a structure oriented to the left side of the fan similar to boulder deposits frequently found in debris flow events (USGS Report 01-0144).

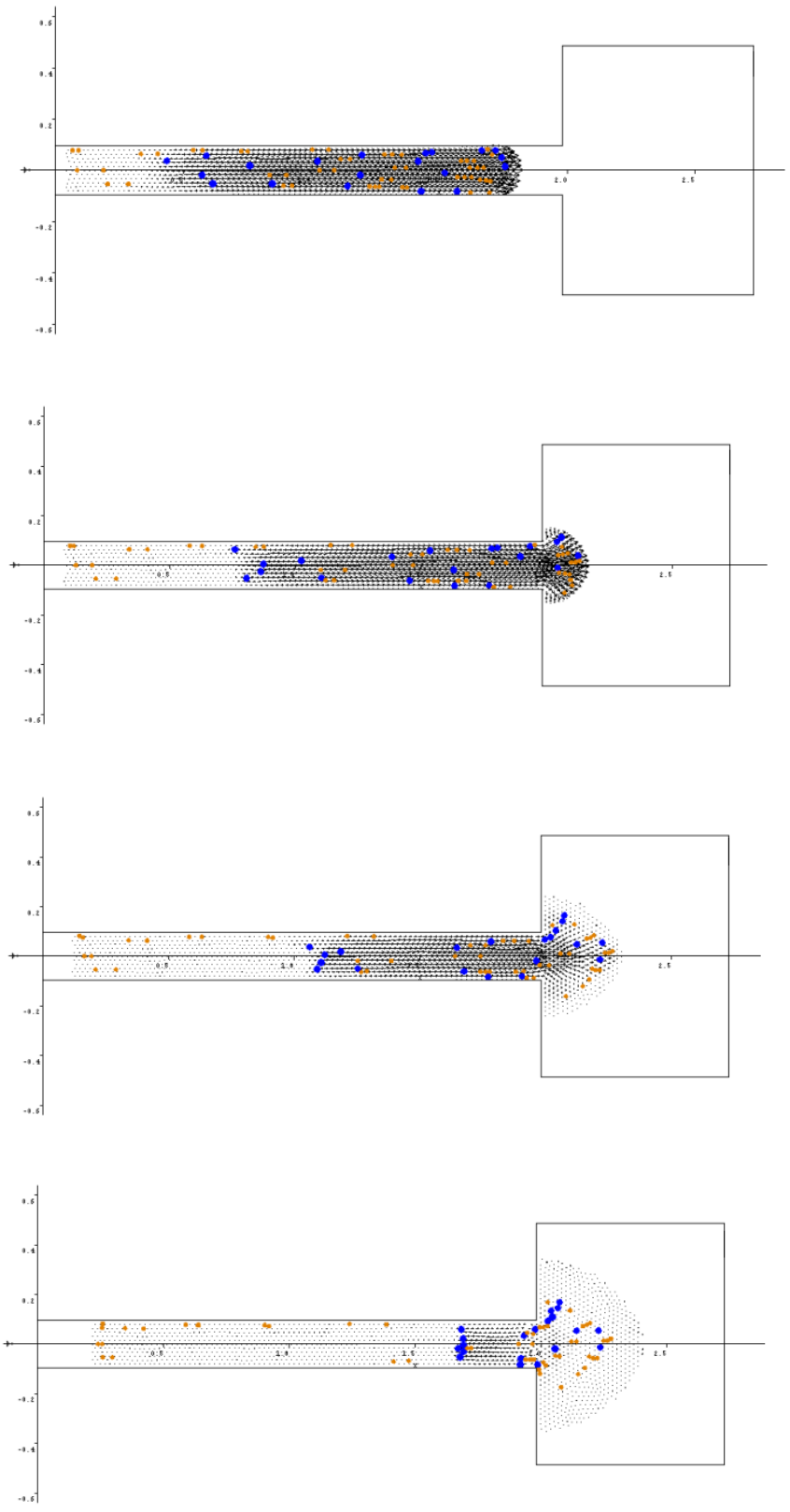

Figure 78. Experiment 5, top view, (a) t = 2.0 s, (b) t = 2.75 s, (c) t = 3.4 s, (d) = 5.0 s

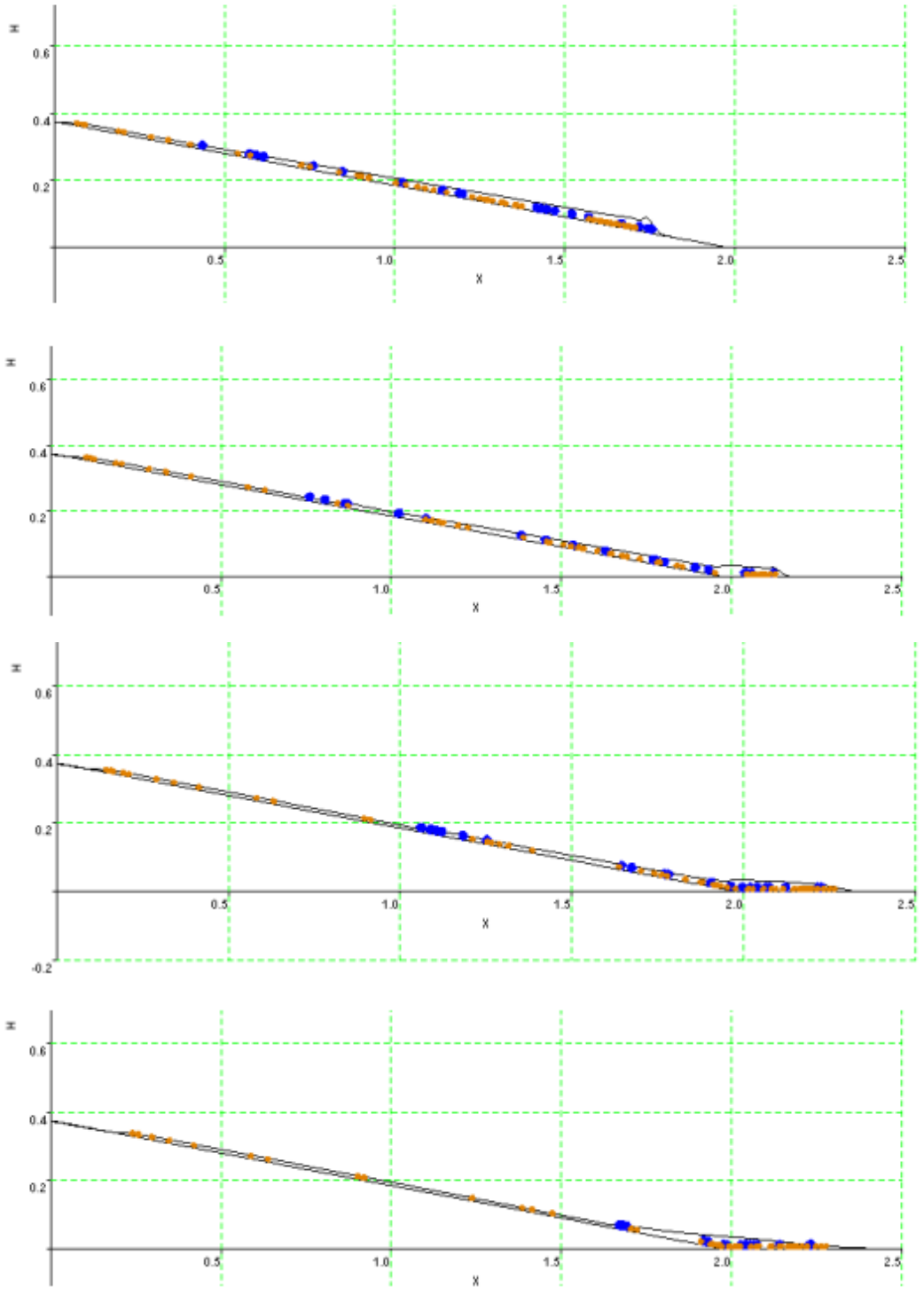

Figure 79. Experiment 5, side view, (a) t = 2.0 s, (b) t = 2.75 s, (c) t = 3.4 s, (d) = 5.0 s

Figures 79(a) to 79(d) shows the simulation from a side view.

4.3.6 Sensitivity Analysis

The main parameters of the numerical model that must be calibrated for an specific physical problem are: friction coefficient μ_f, normal stiffness K_N, tangential stiffness K_T, restitution coefficient E, boundary condition coefficient BC_{coef}, Manning's roughness coefficient N, the empirical coefficients α_1 and β_1, which define the exponential relationship between viscosity of the fluid and volume sediment concentration, and the empirical coefficients α_2 and β_2, which define the exponential relationship between the fluid yield strength and volume sediment concentration. In order to assess the relative importance of each variable, an expression used by McCuen and Snyder (1986) was chosen for the sensitivity analysis. The sensitivity coefficient is the ratio of the relative output change and the relative input change. If for any input parameter whose value is I_1, an output O_1 is produced, and for the input parameter I_2 the output is O_2, the sensitivity coefficient is:

$$S = \left(\frac{O_2 - O_1}{O_{12}} \right) \Bigg/ \left(\frac{I_2 - I_1}{I_{12}} \right) \tag{87}$$

The normalizing values O_{12} *and* I_{12} are the average of outputs O_1 and O_2, and the average of inputs I_1 and I_2, respectively. The use of this sensitivity index has the disadvantage of not taking into account the interaction between variables but, as these authors suggested, it is a simple a preliminary way to examine the behavior of the model variables.

Model sensitivity was estimated in one of the experiments presented previously, experiment 3, which allows the study of the fluid and particle dynamics. The parameters of the model are gathered in Table 3 and Table 4. In Table 3, the distance traveled by one of the particles along the flume is the output variable, specifically one particle situated initially at the front row in the middle of the channel. In Table 4, the maximum extend of the fluid measured along x-direction is the output variable.

Table 3 shows how sensitive is the model with respect to the parameters included in the solid phase formulation, which is the reason why the total distance traveled by a specific particle was chosen as the output variable. This table includes also the BC_{factor}, since the particle dynamics is affected substantially by this parameter. Results in this table show that the model is not very sensitive to the normal stiffness K_N, tangential stiffness K_T, and restitution coefficient E. There is some sensitivity to the variation of the friction coefficient μ_f, specifically in the particle movement along the horizontal fan. Figure 80 shows how the movement of the particle along the channel (first 2.00 m) is not affected by the friction coefficient, but it is affected once the particle reaches the horizontal fan. Less friction coefficient allows the particle to travel a longer distance.

Results in Table 3 also show that the model is very sensitive to the BC_{factor} parameter, this factor is related with the fluid boundary condition at the channel walls, and as it was explained previously, this condition defines the velocity profile across the channel, reason why is very influential in the particle dynamics.

Table 4 shows how sensitive is the model with respect to the parameters included in the fluid phase formulation; then, the maximum extend of the fluid measured along x-direction was chosen as the output variable.

Parameter	I_0	I_1	I_2	O_0	O_1	O_2	S_1	S_2	$\lvert S_1/S_{min}\rvert$	$\lvert S_2/S_{min}\rvert$
μ_f	0.1	0.01	0.2	2.34	2.54	2.28	-0.0501	-0.0390	7.83	6.09
K_N	100000	50000	200000	2.34	2.34	2.35	0.0000	0.0064	0.00	1.00
K_T	10000	5000	50000	2.34	2.35	2.34	-0.0064	0.0000	1.00	0.00
E	0.8	0.4	1	2.34	2.31	2.35	0.0194	0.0192	3.03	3.00
BC_{factor}	0.9	0.5	1	2.34	2.27	2.45	0.0531	0.4363	8.31	68.21

Table 3. Values of the model parameters considered for the model sensitivity analysis with the corresponding sensitivity coefficient S and the ratio $\lvert S/S_{min}\rvert$ where $S_{min} = 0.0064$

Parameter	I_0	I_1	I_2	O_0	O_1	O_2	S_1	S_2	$\lvert S_1/S_{min}\rvert$	$\lvert S_2/S_{min}\rvert$
BC_{factor}	0.9	0.5	1	2.51	2.49	2.70	0.0140	0.6929	1.17	57.74
α_1	6.21E-04	3.10E-04	1.24E-03	2.51	2.70	2.49	-0.1092	-0.0120	9.10	1.00
β_1	17.3	14.3	20.3	2.51	2.52	2.48	-0.0209	-0.0754	1.75	6.28
α_2	0.002	0.001	0.004	2.51	2.70	2.25	-0.1094	-0.1639	9.12	13.66
β_2	40.2	34.2	46.2	2.51	2.70	1.30	-0.4522	-4.5732	37.68	381.10
N	0.02	0.01	0.04	2.51	2.70	2.45	-0.1094	-0.0363	9.12	3.02

Table 4. Values of the model parameters considered for the model sensitivity analysis with the corresponding sensitivity coefficient S and the ratio $\lvert S/S_{min}\rvert$ where $S_{min} = 0.0120$

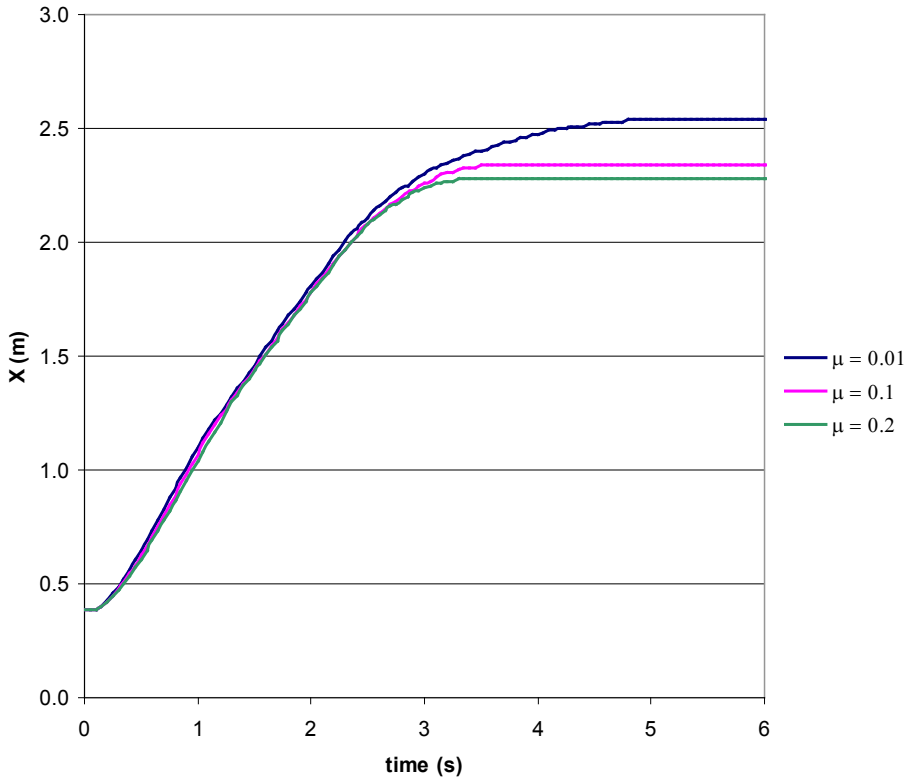

Figure 80. Effect of the friction coefficient in particle movement

Results show that the model is very sensitive to the empirical coefficients α_2 and β_2, which define the exponential relationship between the fluid yield strength and volume sediment concentration. These are key parameters for the calibration process, since they are empirical and correspond to the mixture that compound the fluid. The model shows less sensitivity to the Manning's coefficient, and the empirical coefficients α_1 and β_1, which define the exponential relationship between viscosity of the fluid and volume sediment concentration. The BC_{factor} parameter is also very significant in this case, which confirms the high sensitivity of the model with respect to this variable.

Finally, it is important to mention that all the parameters listed as initial value in the tables are the parameters that were used for the simulation of all the experiments.

5 MODEL PRELIMINARY APPLICATION

5.1 Venezuela's 1999 Alluvial Fan Debris Flooding Event

Heavy rainfall from the storm of December 14 to16, 1999, triggered thousands of shallow landslides on steep slopes of the Cerro El Avila, north of Caracas, Venezuela, and caused flooding and massive debris flows in the channels of major drainages that severely damaged coastal communities along the Caribbean Sea. The largest fan on this area is that of San Julián River at Caraballeda, shown in Figure 81.

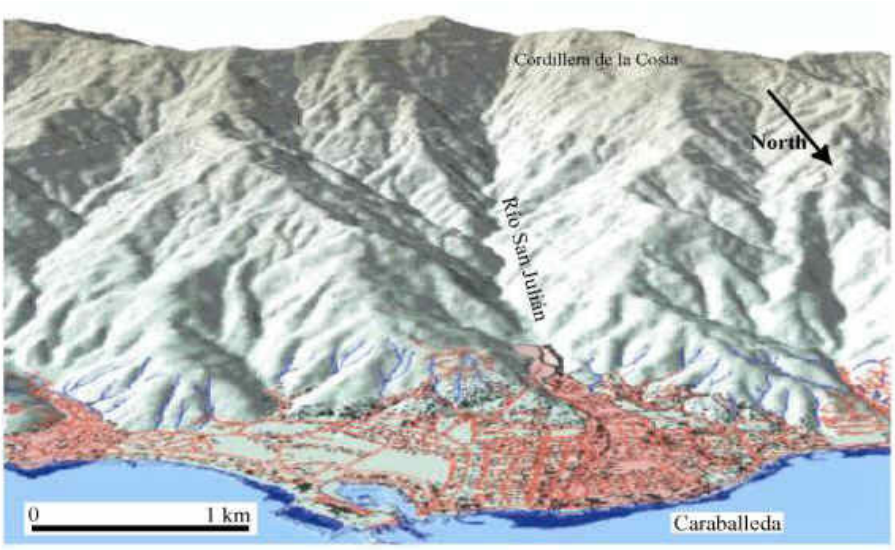

Figure 81. Caraballeda Alluvial Fan, Vargas, Venezuela

The topography of this region of coastal Venezuela is extremely steep and rough; highest elevations range between 6,000 and 7,000 feet and are only a mile inland from the coast. The streams and rivers drain steep canyons, emerging on to alluvial fans before emptying into the Caribbean Sea. The large fan of the San Julián River at Caraballeda was one of the most heavily damaged areas in the December 1999 event. The thickness of sediment deposition, maximum size of transported boulders, and size of inundated area were all notably larger in this drainage in comparison to the other close watersheds.

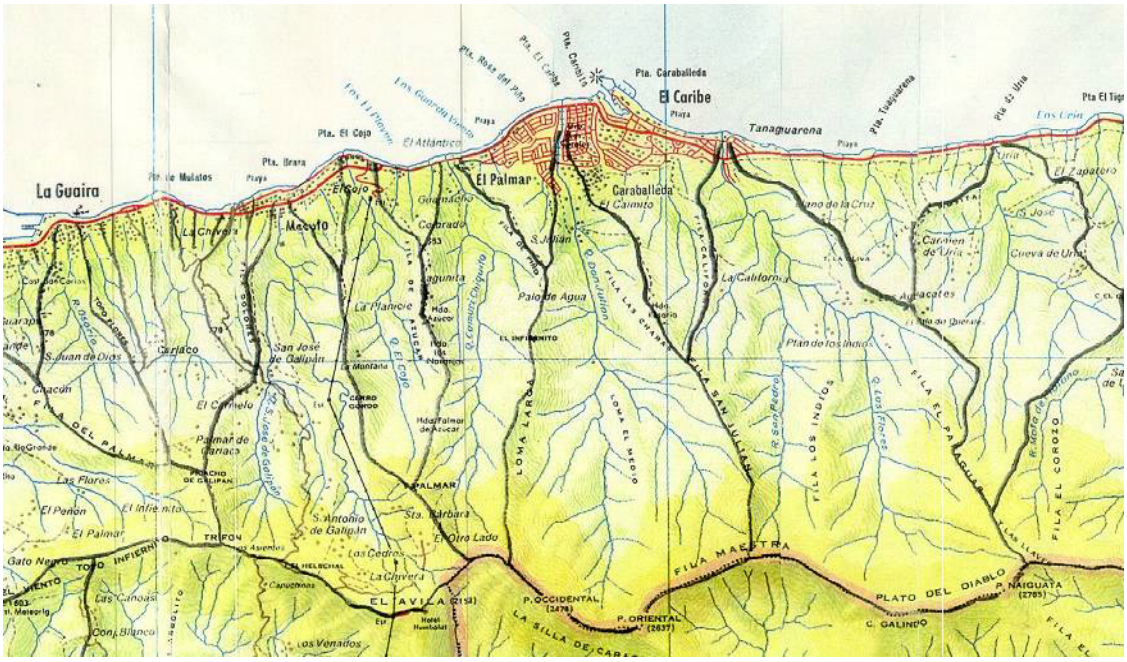

Figure 82. Watersheds situated along coastline, north of Caracas, Venezuela

By December 1999, Caraballeda was one of the more intensively developed communities in the area, with many high-rise buildings and large individual multi-story houses. San Julian River was canalized on one reach of the fan with one concrete trapezoidal 25 m wide channel, Figure 83. During the storm, the peak volume of flow, probably during a debris-flow surge, exceeded the channel capacity, sediment and debris blocked two bridges over the channel, resulting in multiple stream avulsions and subsequent flows spreading boulders and debris throughout the area.

The flow overcame the channel in several places, notably wherever sections or lineaments of the channel changed direction. Pre-1951 topographic maps show that the main course of the San Julián River followed a more or less straight path across the western part of the fan. In the events of December 1999, one of the stream avulsions followed the pre-1951 course, as shown in Figure 84.

Figure 83. Aerial view of San Julian river, March 1999

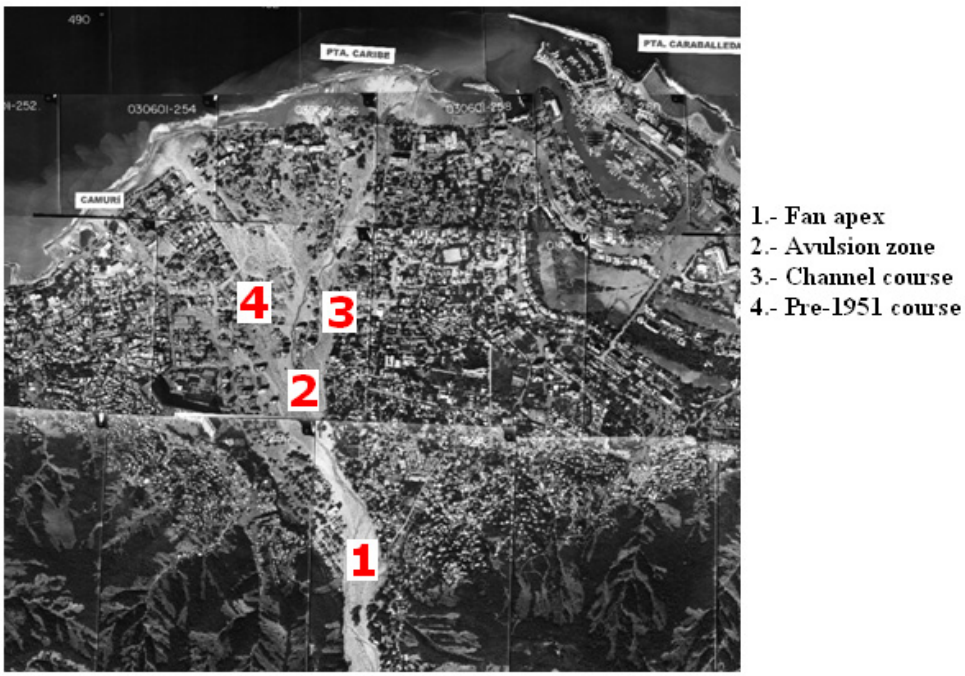

Figure 84. Aerial view of San Julian river, December 1999

Outside of the main channel, flows inundated the second and third stories of several apartment buildings, causing their partial collapse, and also burying or completely destroying many 2-story residential structures. Further down the fan, flows followed the paths of streets and openings between houses; the depth of sediment deposits diminished, but still exceeded one meter in several locations.

Figure 85. Buildings and houses partially buried by sediment in Caraballeda, December 1999

Following the December 1999 events, the US Geological Survey studied the affected area (Wieczorek *et. al* 2001), measuring slope, deposit thickness, and boulder size from the fan apex to the distal end of the fan near the coastline. Data was used to map the distribution and thickness of deposits and to draw contours of maximum boulder size, as shown in Figures 86 and 87.

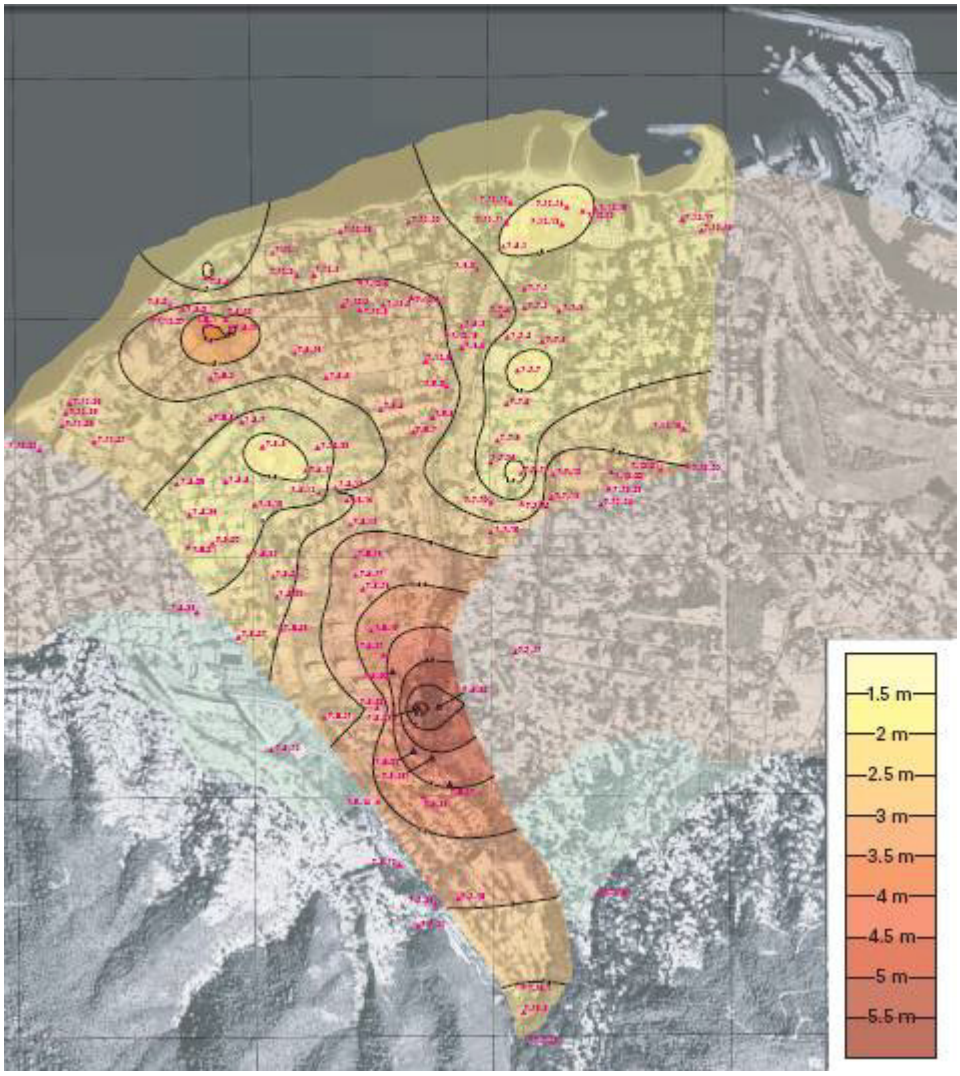

Figure 86. Contours of maximum transported boulder size on the Caraballeda Fan, Venezuela. From USGS , 2002

According to USGS measurements and observations, see Appendix C, boulder size ranged from 1.0 to 6.0 m of nominal diameter, largest boulders were found in the avulsion zone, location where more accumulation of boulders was also observed.

The thickest deposits were also in this zone, at this location, the fan slopes ranged between 5 and 6 degrees, and the maximum thickness of deposits was 7 m. Deposits on

slopes of 2 to 3 degrees, near the shoreline, were predominantly fine-grained and less than 1 m thick.

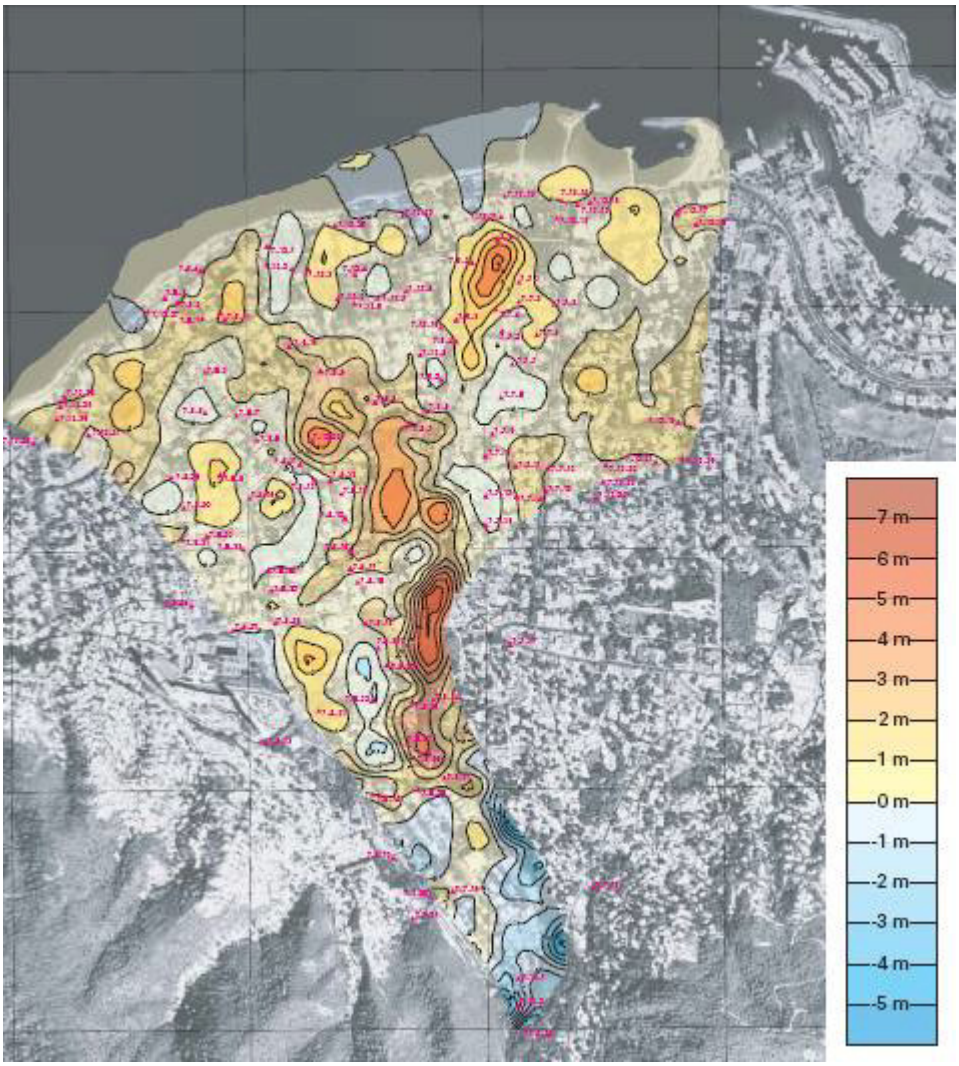

Figure 87. Flooding deposit thickness on the Caraballeda Fan, Venezuela. From USGS , 2002

5.2 Modeling procedure

The following figure shows the topography data used to define the finite element mesh. This data was interpolated from the original cartographic information prior to the event (Garcia, 2008).

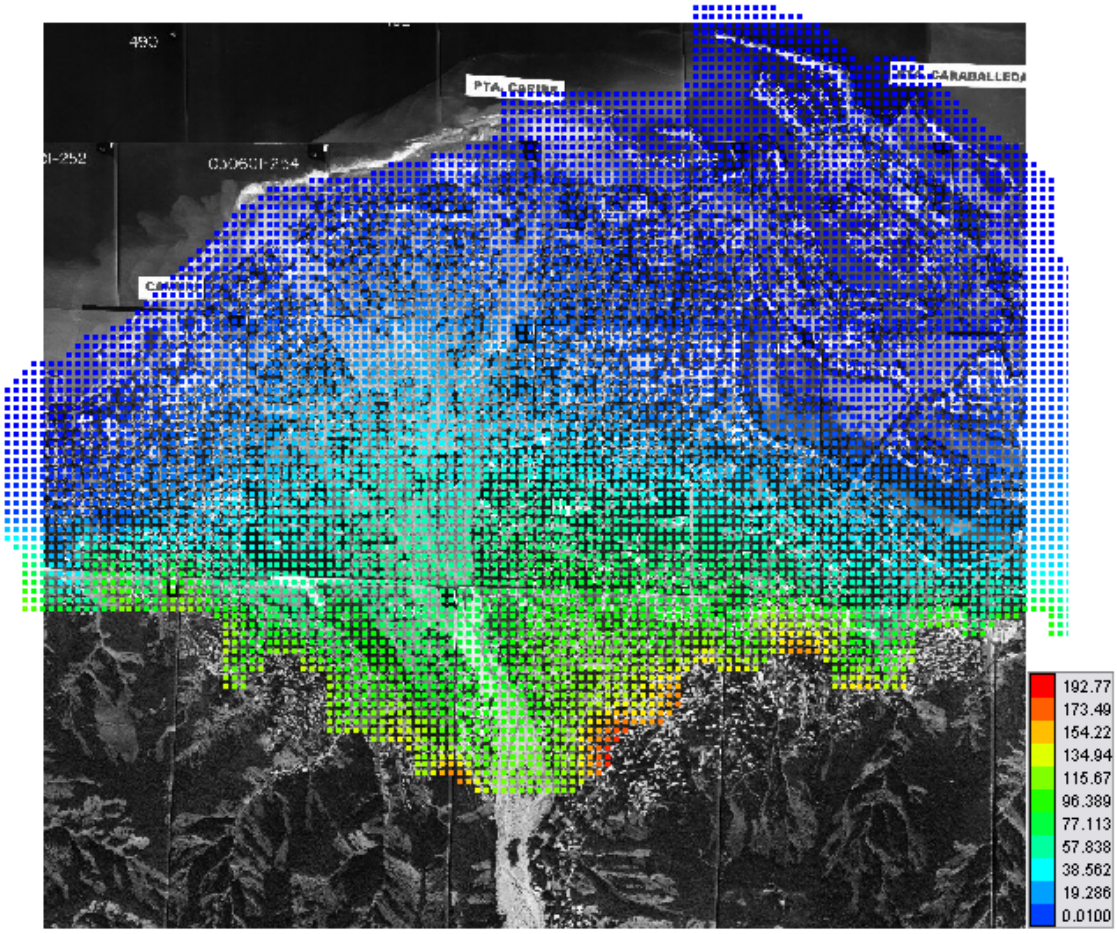

Figure 88. Topography Data Caraballeda Fan, Vargas, Venezuela. Legend indicates elevations in m.

An uncertain aspect in simulating debris flows is the estimation of the hydrograph, since the inflow sediment concentration throughout the event must also be provided. For the San Julian debris flow event, the clear water hydrograph of generalized cumulative rainfall for a 500 year-return period was used as input in the fan apex (Garcia. The hydrograph shown in Figure 89 was modified, increasing the volume, by imposing an average volume sediment concentration. Figure 90 shows the volume sediment concentration distribution. For simplicity, it was assumed that the sediment volumetric concentration was constant and equal to the average value of 0.3.

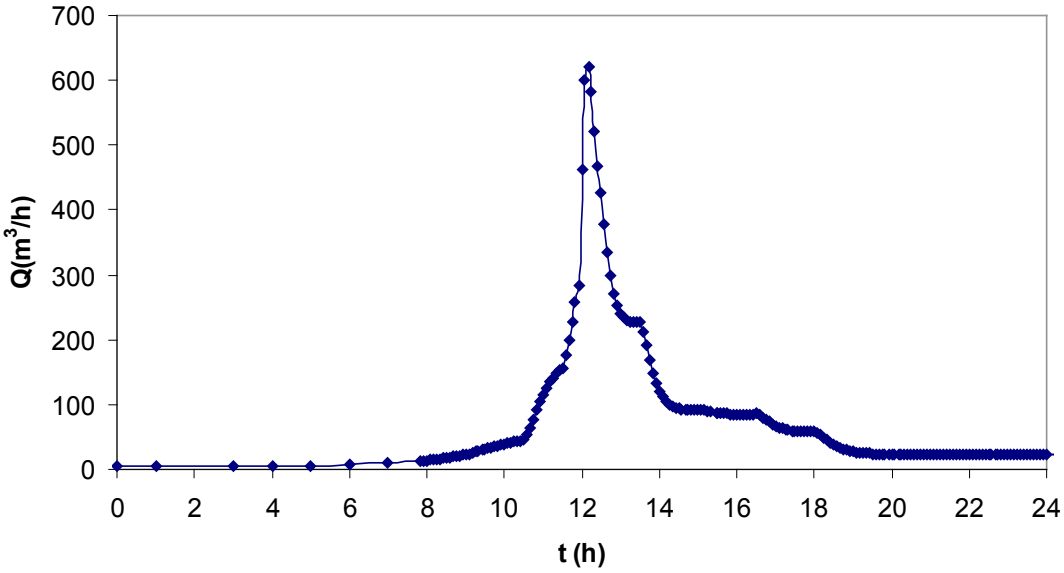

Figure 89. Inflow hydrograph for a 500 year-return period. Garcia, 2008

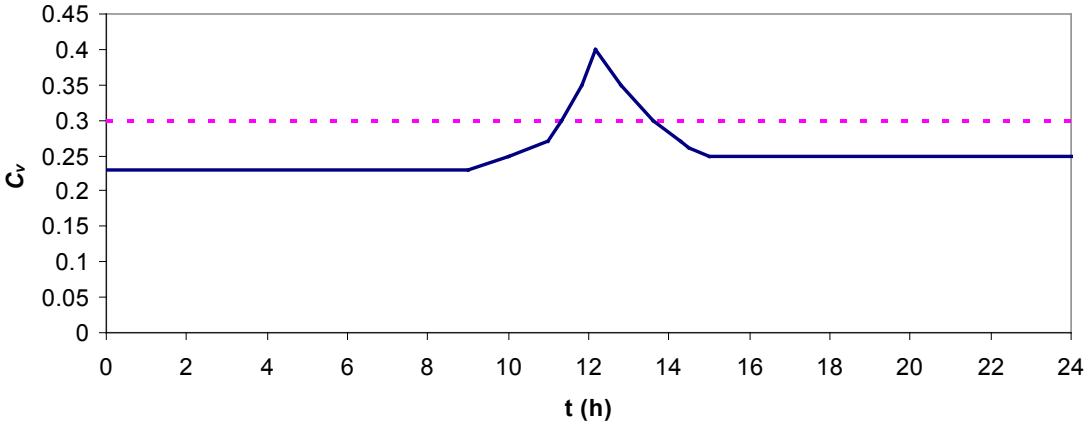

Figure 90. Volumetric sediment concentration distribution. Garcia, 2008

The final hydrograph used as input in the fan apex is shown in Figure 91. The plot illustrates the input flow rate during 10 hours (simulation time), from real time t = 10 h to real time t = 20 h and includes the volume sediment concentration.

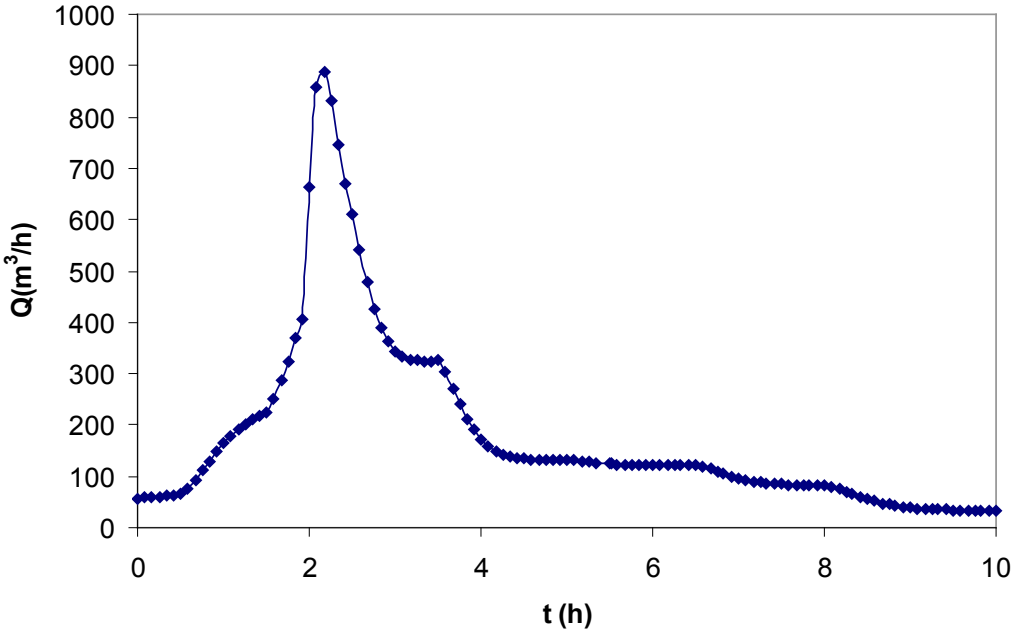

Figure 91. Inflow hydrograph for a 500 year-return period, including concentration of solids equal to 0.3

A second uncertain aspect of the simulation is the input rate of solid particles, or identically, boulders. It is assumed that during the simulation time a maximum of 1600 boulders, with different sizes, will be included in the event. The rate of input will be variable for the different scenarios. This amount of boulders is chosen to have a manageable running time.

The Finite Element mesh, with 22500 triangular elements, is shown in Figures 92 and 93. The element characteristic size is approximately 12 m in average. At the fan apex a fictitious channel was extended upstream, to locate particles and allow the fluid to entrain boulders before entering the fan area.

A Manning coefficient equal to 0.065 is considered in the whole fan area in order to take into account the terrain irregularity. The same value was used by Garcia, 2008,

and was found a good estimate for the area. The empirical relationships (9) and (10) were selected for the calculation of fluid rheological properties, using the parameters for water-clay mixtures. As a result of the volume sediment concentration, C_v = 0.3, ρ = 1531 Kg/m^3, μ = 0.11 Pa.s, τ_y = 90.3 Pa.

Density for the particles (boulders) was ρ = 2600 Kg/m^3, density of Gneiss boulders, type of boulders mostly found in the area by USGS.

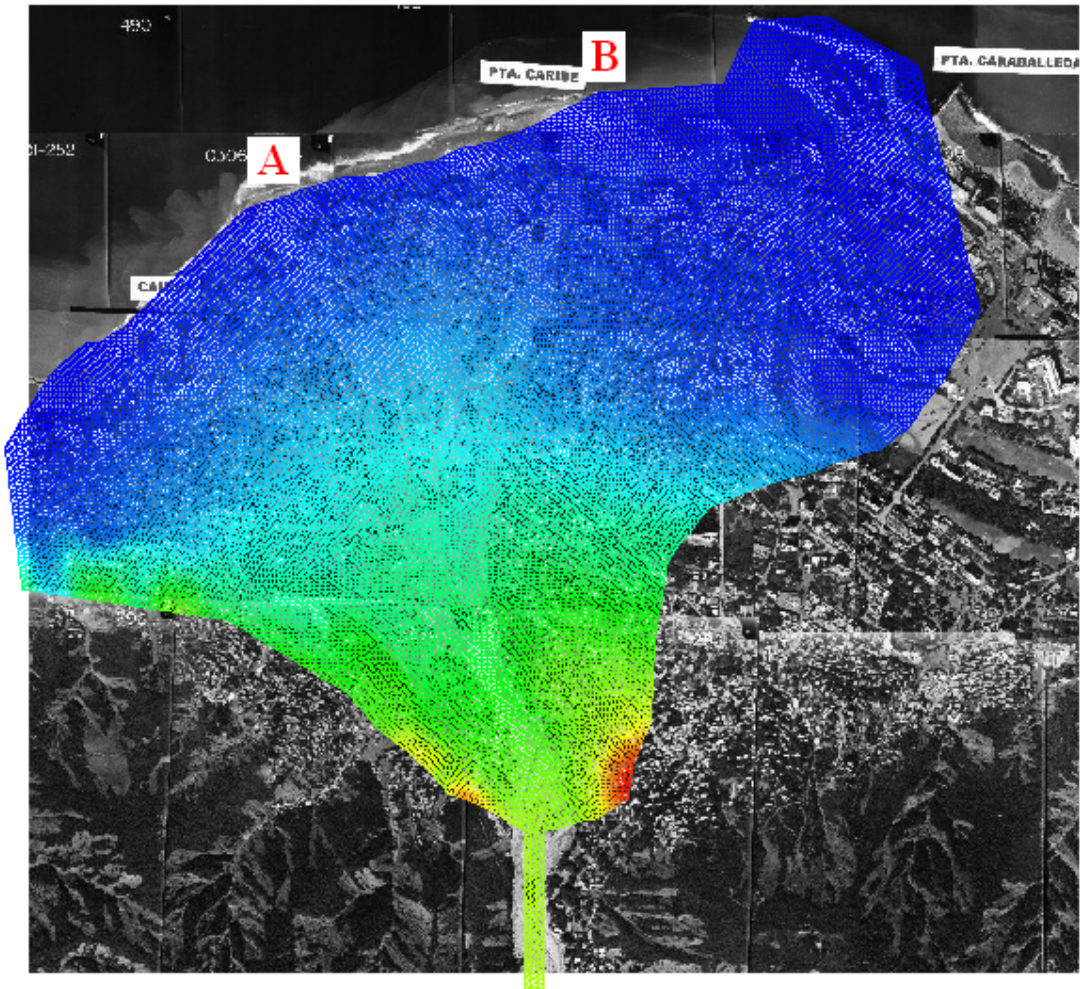

Figure 92. Finite Element Mesh, San Julian simulation

The coastline was assumed as a free boundary with the exception of two segments, A and B in Figure 92, where the major discharges to the sea took place. In these segments a constant depth equal to the water elevation, 2 m, was imposed.

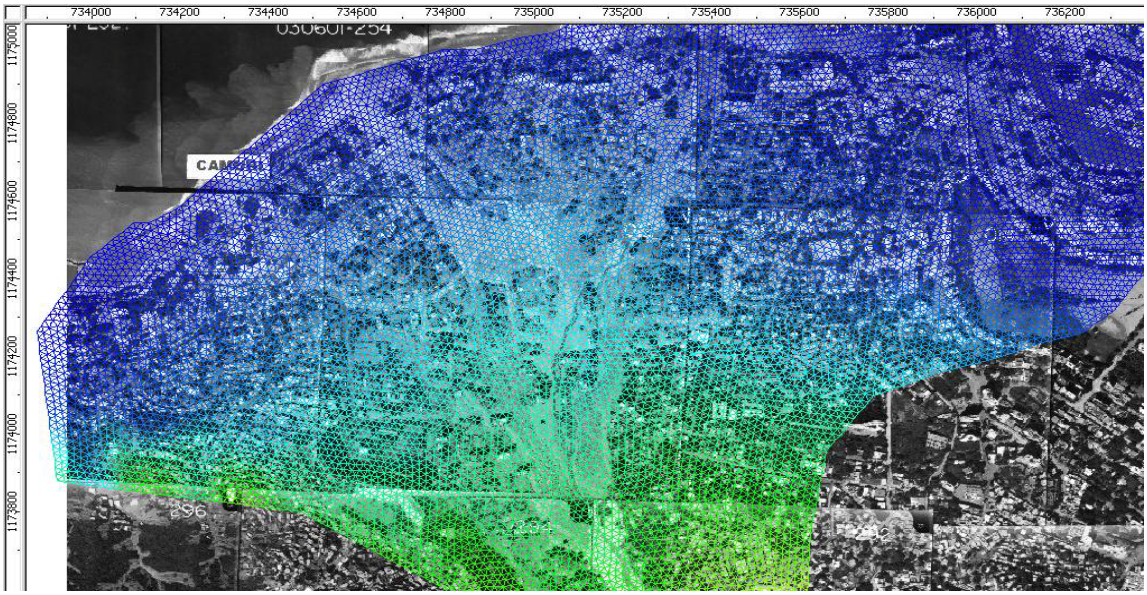

Figure 93. Finite Element Mesh zoomed at fan area

5.3 Model results

In this case of study 1600 particles are placed into the fan during the first three hours of simulation at a rate of 50 particles every 6 min. The input flow rate at the fan apex is given by the hydrograph in Figure 91. This amount of particles was selected to ensure a manageable running time.

Figure 94 and 95 show the flooded area at time t = 1.8 h and time t = 2.2 h respectively, being 2.2 h the time corresponding with the peak discharge in Figure 91. Comparing these figures with the post-event aerial view shown in the background, it can be noted that the model acceptably reproduces the extent of the area affected by the debris flow. The simulation results show an inundation area some larger than the one

observed in 1999 events, when comparing with the post-aerial view in Figure 85. However, it must be taken into account that this simulation was done without modeling the concrete canal exact dimensions and surface properties, then more severe results could be expected.

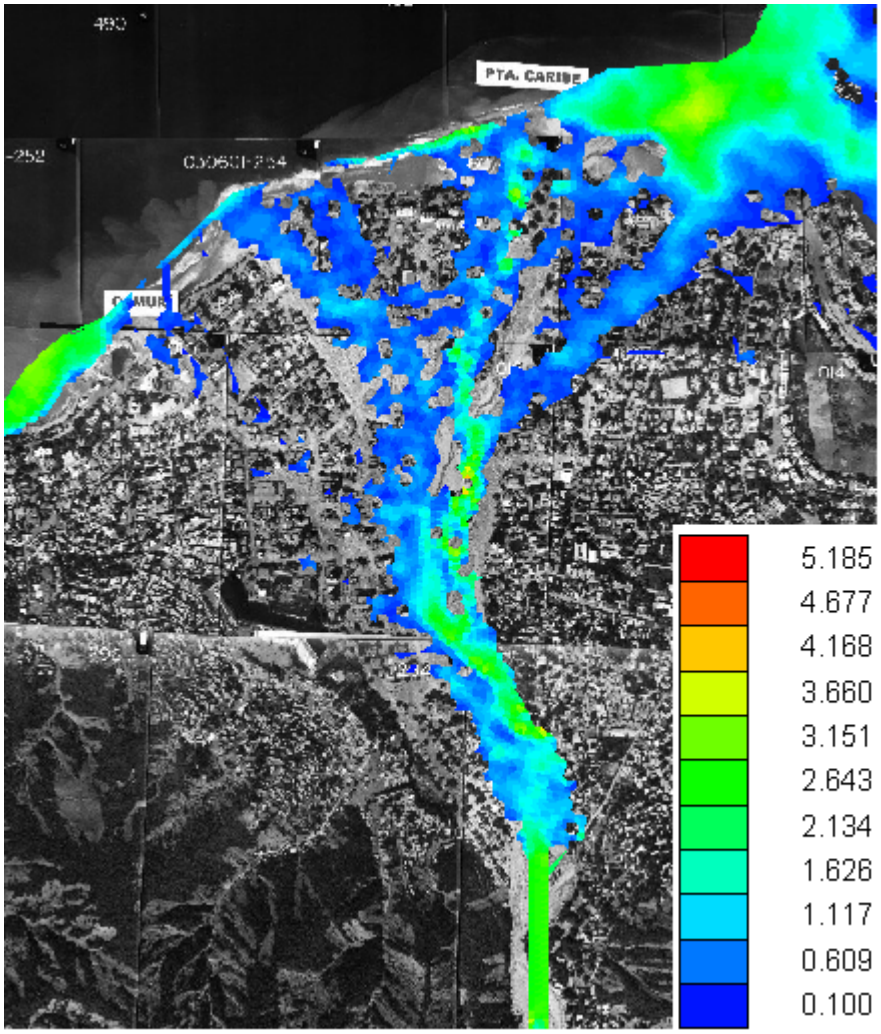

Figure 94. Flooded area at time t =1.8 h, Legend indicates flow depth in m.

It have been concluded in previous studies that even though the concrete canal was totally obtruded during the event, its presence was relevant during enough time to conduct the flood to the sea and decrease the inundation in the surrounding area.

Not counting shoreline bays and the fictitious channel at the fan apex, the maximum flow depths take place in the avulsion zone, 5.5 m, as it can be read in Figure 95. According to the USGS report, one of the largest thicknesses of the alluvial deposits was measured in this zone and it was in the order of 4 to 5 m.

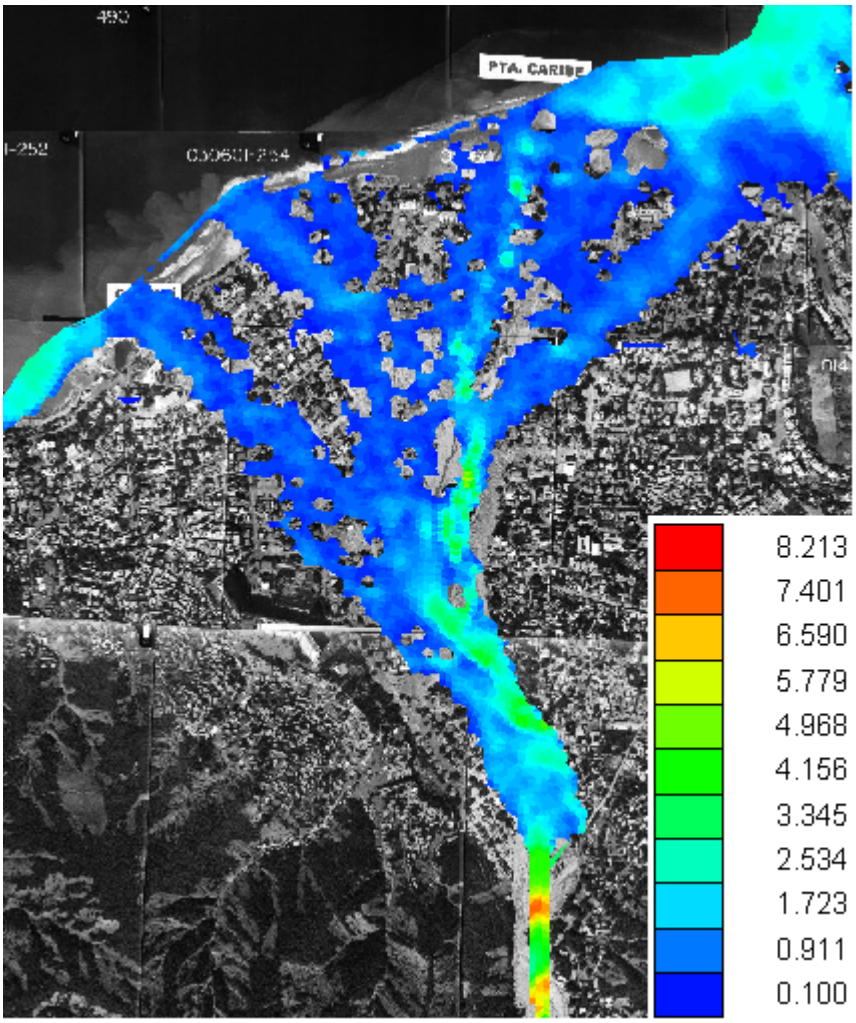

Figure 95. Flooded area at time t =2.2 h. Legend indicates flow depth in m.

Maximum fluid depth in the urban areas was between 2 and 3 m according to Garcia 2008, decreasing to 0.5 to 1 m in zones closer to the shoreline. Results in Figure 95 are in this range.

Figures 96 and 97 show the velocity field at time t = 1.8 h and t = 2.2 h respectively.

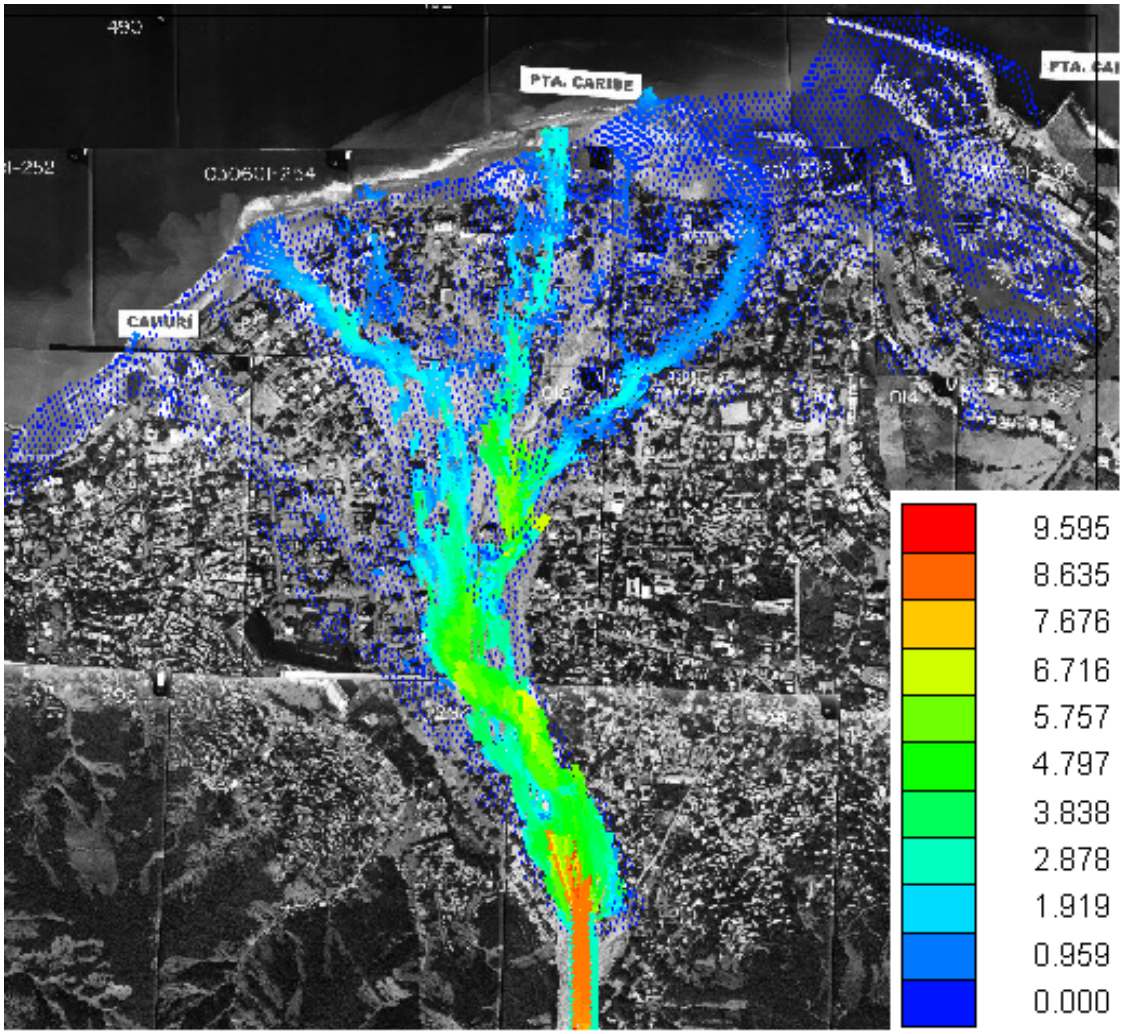

Figure 96. Velocity field at time t =1.8 h. Legend indicates velocity in m/s.

. It can be seen that major velocities occurs in the fan apex, where the discharge of the river is simulated. Velocities decrease at the urban areas, ranging from 0.5 to 3 m/s at

1.8 h and from 1.0 to 6 m/s at 2.2 h, time of the hydrograph maximum value. Higher velocities develop along the concrete channel, reaching 8 m/s, and in the avulsion zone, reaching 10 m/s. The velocities calculated by the model are in good agreement with those estimated by USGS, which ranged from 1.3 to 13.6 m/s, see Appendix C.

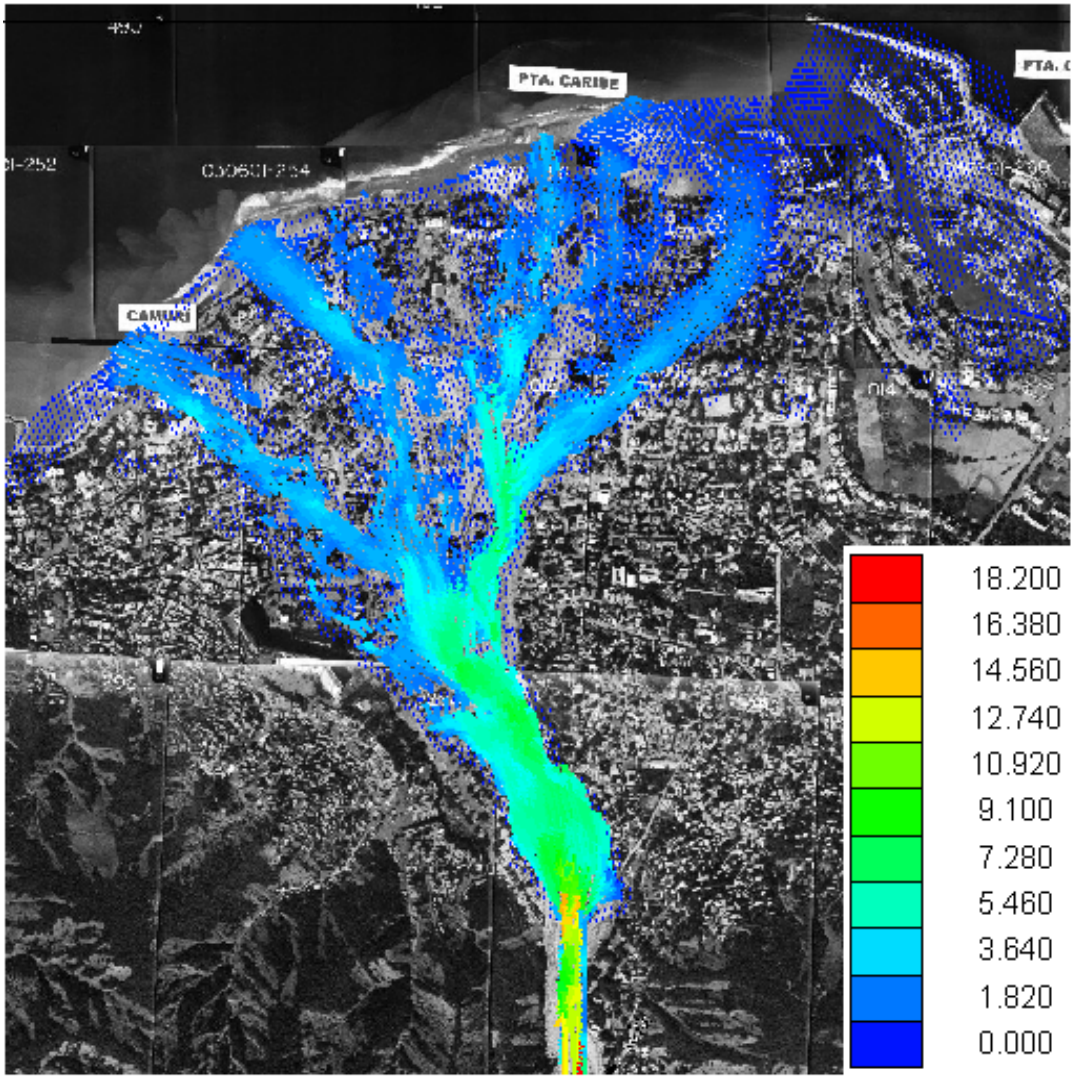

Figure 97. Velocity field at time t =2.2 h, Legend indicates velocity in m/s.

Figure 98 shows how solid particles, boulders, are transported by the flow along the main drainages at time t = 1.8 h. It is interesting to see how the largest boulders take the path of the concrete channel, while smaller boulders take the pre-1951 river alignment. According to the USGS report, the slope at zone 4, pre-1951 river orientation, was 4.0 degrees, while zone 3, concrete channel direction, was steeper, with a slope gradient of 5.5 to 6 degrees, then larger boulders were transported to this side. These values of mean nominal diameter and slope steepness reflect USGS observations that for the larger transported and deposited boulders there was a proportional relationship between boulder size and slope steepness.

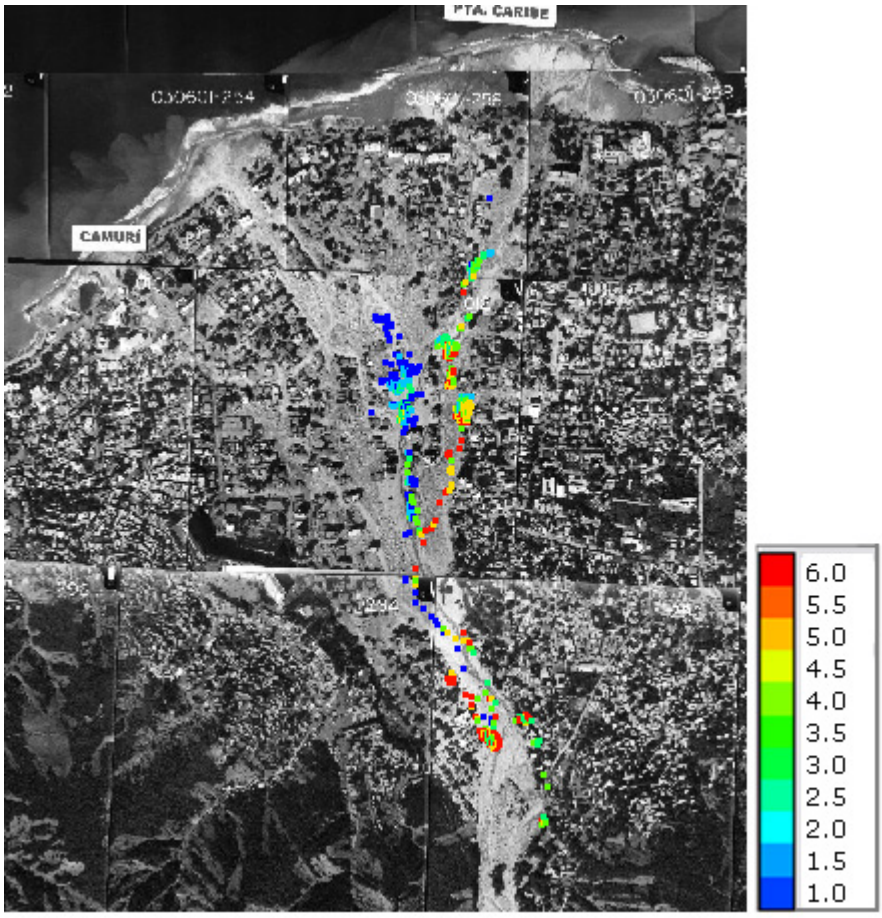

Figure 98. Particle positions at time t =1.8 h, Legend indicates diameter in m.

Figure 99 shows boulder positions after 6 hours of simulation in comparison with contours of maximum boulder size given by USGS. By this time in the simulation all boulders are already deposited. Smaller boulders continue taking the pre-1951 river alignment, some of them reached the shoreline or entered into the sea. Larger boulders were deposited in the avulsion zone or took right direction to the concrete channel. None of these large boulders reached the shoreline.

According to USGS the largest boulders were found in the avulsion zone, within a thick matrix, evidence that strongly supports transport by debris flow. At other sites, the largest boulders were observed isolated along the concrete channel, fact that suggests that these boulders moved sliding along the bottom of the channel in a dilute fluid until deposition occurred (USGS Report 01-0144). There is no indication of big boulders close to the shoreline at this site of the fan.

According to Takahashi, 1991, during the process of deposition, debris flows deposit the boulders in order from bigger to smaller as it proceeds downstream on alluvial fans. This process was better observed along the pre-1951 river direction and it was also replicated in the numerical simulation.

Figure 99 (a) shows the data surveyed by USGS. USGS map show size of boulders contoured from measurements using 0.5 meter contours. USGS measured the size of several boulders deposited in the Caraballeda alluvial fan, recording the lengths of the major three axes for all boulders. In terms of nominal diameter, equal to the cubic root of the product of these dimensions, the mean nominal diameter of boulders deposited at different stations was tabulated and is given in Appendix C.

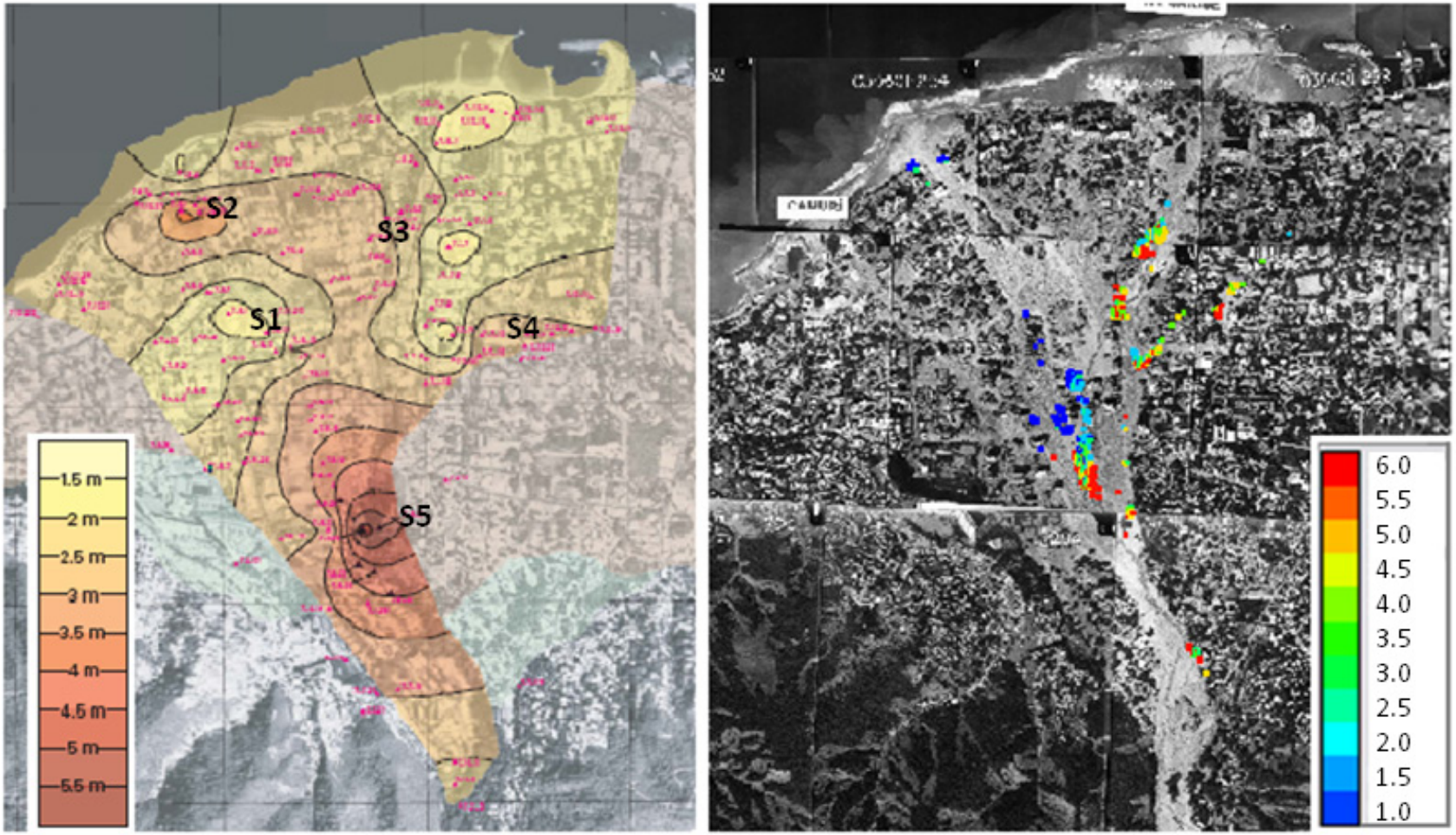

Figure 99. (a) Contours of maximum boulder size at the Caraballeda Fan. (b) Particle positions at time t =6.0 h, diameter (m)

Some of these stations are depicted in Figure 99 (a), for station S1 the mean nominal diameter was 1 m, while some larger boulders are deposited slightly further down the fan towards station S2, with 3.5 m nominal diameter. For comparison, boulders deposited at station S3 and S4 had mean nominal diameter of 3 m, and boulders deposited at station S5 had mean nominal diameter of 5 m. The final distribution of boulders obtained numerically shows similar results as it is depicted in the map illustrated in Figure 99 (b).

This preliminary application illustrated the capability of the model to reasonably reproduce large scale events. The model showed to be effective in the simulation of a real debris flow event over irregular slopes; fluid variables, velocity and depth, and final deposition of particles where well calculated with this new numerical model.

6 CONCLUSIONS

This thesis research describes the development of a quasi three-dimensional mathematical-numerical model to simulate stony debris flows, considering a continuum fluid phase and large sediment particles, such as boulders, as a non-continuum phase.

The fluid phase governing equations are the well-known shallow water equations, where the stress terms account for the bottom friction using the Manning's formula and the internal friction losses are implemented through a constitutive relation. Two different non-Newtonian constitutive relations are evaluated in this work, the Bingham rheological model and the Cross rheological model.

The fluid phase equations are solved using the Finite Element Method and a four-step, selective lumping, explicit time stepping scheme, that does not require simultaneous solution of the algebraic system of equations, usually required in implicit finite element methods.

Both formulations, Bingham and Cross, provide very stable results, even in the range of very low shear rates. In the simulation of mud dam-break problems, Bingham formulation is better able to simulate the stopping stage of the fluid; however, Cross formulation is more accurate for early stages of the solution, where Bingham is not as accurate.

The capability to simulate drying and wetting of the bed is crucial when solving mud dam-break problems. The implementation of a wet-dry algorithm improves noticeably the representation of the fluid frontal wave and numerical errors are considerably reduced when dry elements are eliminated from the Finite Element Method calculations.

Variation of the selective lumping parameter also enhances the numerical solution in the advancing front; values between 0.85 and 0.95 produce stable results, been 0.925 the value that provided more accurate results.

In practical applications, the no-slip boundary condition formulated in finite elements becomes very restrictive, and may cause unrealistic delay of the flow. However, slip boundary condition may cause other serious errors, as in the simulation of channel flows. If a total slip condition is imposed at the channel walls, then no velocity profile can be reproduced across the channel. The no–slip boundary condition can be replaced by a weaker condition, such as total impermeability and partial tangential velocity. The relationship $u_T = 0.9(\vec{u} \cdot \vec{t})$ produced very accurate results in the simulation of the dam-break experiments performed in this work.

The solid phase governing equations are based on the principles of the Discrete Element Method. Particles' trajectories are tracked using Newton's second law and the forces considered are gravity, buoyancy, fluid drag force and collision forces. The acceleration of the particle is computed from the particle governing equation and it is then numerically integrated to find velocity and displacement.

To ensure stability and accuracy of the numerical integration, it is important to guarantee a smaller time step than the minimum critical time, or time of impact, defined in equation (26). It was found during this work that a minimum of three time steps per time of impact are required to ensure a stable and accurate solution.

The simulation of lab experiments served for the verification of the numerical model and demonstrated the capability of the model of simulating the motion of discrete

particles in the fluid flow, showing that particles do not overlap and replicating realistically particle-particle and wall-particle collisions.

The sensitivity analysis performed showed that the model is very sensitive to the empirical coefficients α_2 and β_2, which define the exponential relationship between the fluid yield strength and volume sediment concentration. The BC_{factor} parameter resulted also very significant; this factor defines the tangential velocity boundary condition at the walls. The model showed less sensitivity to the Manning's coefficient N, and the empirical coefficients α_1 and β_1, which define the exponential relationship between viscosity of the fluid and volume sediment concentration. The model showed very few sensitivity to the parameters related with the solid phase formulation; the normal stiffness K_N, tangential stiffness K_T, and restitution coefficient E. There was some sensitivity to the variation of the friction coefficient μ_f, specifically in the particle movement along the horizontal fan.

The final application to the debris flow events that occurred in Northern Venezuela in1999 illustrated the capability of the model to reasonably reproduce large scale events. Results showed that the model reasonably simulates the extent of the area affected by the debris flow and demonstrated the model capability of replicating the main boulder accumulation areas, including size distribution, surveyed by the USGS.

7 RECOMMENDATIONS

The numerical model developed in this work for the simulation of debris flows is based on the well-known shallow water equations. This equations are derived assuming that extend of the fluid is much larger than its depth and assuming that slopes are relatively small, less than 10^{o}. This numerical model must be used under these conditions.

In this work, the rotation of the particles is not considered. The effect of particle rotation and the corresponding lift produced could be modeled by solving for the angular velocity of the particles in the angular equation of motion, including the torque exerted on them by the fluid and by the contact with other particles. It is recommended to include this effect if dynamics of particles would be study over the area of deposition, specifically when particles leave the fluid and continue moving and interacting with other particles.

This numerical model considers only spherical particles, it is recommended to extend the program to work with general shapes. Theory of clusters formed with spherical particles could be use, as described in Mustoe G. W. and M. Miyata, 2001.

Finally it is recommended to improve subroutines for detecting particle contacts and for finding the element where the particle is located, this will decrease considerably the solution computational time.

REFERENCES

Asmar B.N., Langston P.A., Matchett A.J., Walters J.K. 2002. Validation tests on a distinct element model of vibrating cohesive particle systems. *Computers and Chemical Engineering,* 26(6): 785-802.

Asmar B. N., Langston, P. A. and Ergenzinger, P. 2003. The potential of the Discrete Element Method to simulate debris flow. *Debris-flow hazards mitigation: mechanics, prediction and assessment*, 1:435-445.

Balmforth, N. J., Craster, R. V., Rust, A.C. and Sassi, R. 2006. Viscoplastic flow over inclined surface. *Journal of Non-Newtonian Fluid Mechanics,* 139:103-127.

Barnes, H.A., Hutton J.F., Walters, K. 1989. An introduction to rheology. Amsterdam. Elsevier.

Bagnold, R. A. 1954. Experiments on a gravity-free dispersion of large solid spheres in a Newtonian fluid under shear. *Proceedings of the Royal Society of London*. 225: 49-63.

Bello, M. E., López, J. L., García-Martínez, R. O'Brien, J. S. 2003. Simulation of flooding and debris flows in the Cerro Grande River. *Acta Científica Venezolana,* 54(1) : 22-32.

Bingham , E. C., and Green, H. 1919. Paint, a plastic material and not a viscous liquid; the measurement of its mobility and yield value. *Proceedings of American Society of Testing Materials*, 19: 640-664.

Chow, Ven T. 2000. Open Channel Hydraulics. Mc Graw Hill. New York.

Cleary, P. W. and Prakash, M. 2004. Discrete-element modelling and smoothed particle hydrodynamics: potential in the environmental sciences. *Philosophical Transactions of the Royal Society* of *London,* 362:2003–2030.

Clift, R. and Gauvin, W.H. 1971. Motion of Entrained Particles in Gas Streams. *The Canadian Journal of Chemical. Engineering,* 49: 439-448.

Coulomb, C.A. 1776. Sur une application des régles, de maximis et minimis á quelques problémes de statique, relatifs á l'architecture. *Paris, L'Imperial Royale, Mémoires de Mathématique et de Physique*, 343–384.

Coussot, P. and Piau, J. 1994. On the behavior of fine mud suspensions. *Rheologica Acta*, 33(3): 175-184.

Coussot, P. and Meunier, M. 1996. Recognition, classification and mechanical description of debris flows. Earth Science Reviews 40:209–227.

Cundall, P. A. 1971. A computer model for simulating progressive large scale movements in block rock systems. *Proceedings of the Symposium of the International Society of Rock Mechanics*, Nancy, II, Article 8.

Cundall, P.A. and Strack, O.D.L. 1979. A discrete numerical model for granular assemblies. *Geotechnique*, 29: 47-65.

Dent, D. J. and Lang, T. E. 1983. A biviscous modified Bingham model of snow avalanche motion. *Annals of Glaciology*, 4: 42-46.

García-Martínez, R., Espinoza, R., Valera, E. & González, M. 2006. An explicit two-dimensional finite element model to simulate short and long term bed evolution in alluvial rivers. *Journal of Hydraulic Research*, 44 (6): 755-766.

Garcia, R., Gonzalez, N. & O'Brien, J. 2009. Dam-break flood routing. Chapter 5 of Dam-Break Problems, Solutions and Case Studies. Ed. De Wrachien, D. & Mambretti, WIT Press. ISBN: 978-1-84564-142-9.

Garcia, R. and Lopez, J.L. 2005. Debris Flows of December 1999 in Venezuela. *Chapter 20th of Debris-flow Hazards and Related Phenomena*. Springer Verlag Praxis, Berlin.

Garcia, F.R., Saavedra, I., Febres, B., Valera, E., and Villoria, C. 1999. "A two-dimensional computational model to simulate suspended sediment transport and bed changes". Journal of Hydraulic Research, 37(3).

R. Garcia, R. 2008. Mud Flow Hazard Maps for Vargas State. Final Report for the Avila Project. Fluid Mechanics Insitute, University of Central Venezuela, (In Spanish).

Hammad, K. & Vradis,G.C. 1994. Flow of a non-Newtonian Bingham plastic through an axisymmetric sudden contraction: effects of Reynolds and yield numbers. *Numerical Methods Non- Newtonian Fluid Dynamics*, ASME 179: 63-90.

Herschel, W. H. and Bulkley, R. 1926. Measurement of consistency as applied to rubber-benzene solutions. *Proceedings of American Society of Testing Materials*, 26: 621-633.

Hertz, H. 1882. Uber die Beruhrung fester elastischer Korper (On the contact of elastic solids). *J. Reine Angewandte Mathematik*, 92: 156-171.

Huang, X. & Garcia, M.H. 1997. Asymtotic solution for Bingham debris flows. *Debris-flow hazards mitigation: mechanics, prediction and assessment*. Proceedings of the First International Conference, ASCE, New York, 561-575.

Huang, X. & Garcia, M.H. 1998. A Herschel-Bulkley model for mud flow down a slope. *Journal of Fluid Mechanics*, 374: 305-333.

Hutter, K., Siegel, M., Savage, S. B. and Nohguchi, Y. 1993. Two dimensional spreading of a granular avalanche down an inclined plane. Part 1. Theory. *Acta Mechanica.* 100: 37–68.

Iverson, R. M. 1997*a*. Hydraulic modeling of unsteady debris-flow surges with solid-fluid interactions. *Debris-flow hazards mitigation: mechanics, prediction and assessment*. Proceedings of the First International Conference, ASCE, New York, 550–560.

Iverson, R. M. 1997*b*. The physics of debris flows. *Reviews of Geophysics*.35:245–296.

Iverson, R.M. and Denlinger, R.P. 2001. Flow of variably fluidized granular masses across 3-D terrain: 1. Coulomb mixture theory. *Journal of Geophysical Research*, 106(B1): 537-552.

Iverson, R. M. and Vallance, J. W. 2001. New views of granular mass flows. *Geology*, 29(2): 115-118.

Johnson, A. M. 1965. A model for debris flow. Ph.D. dissertation. Pennsylvania State University, University Park.

Johnson, A. M. 1970. *Physical processes in geology*. Freeman, Cooper&Company, 431-459.

Johnson, K. L. 1985. *Contact Mechanics*, 2nd ed. Cambridge University Press, New York.

Komatina, D. & Jomanovic, M. 1997. Experimental study of steady and unsteady free surface flows with water-clay mixtures. *Journal of Hydraulic Research* 35: 579-590.

McCuen, R.H., Snyder, W.M., 1986. Hydrologic Modeling: Statistical Methods and Applications. Prentice-Hall, Englewood Cliffs.

Mainali, A. and Rajaratnam, N. 1994. Experimental Study of debris flows. *Journal of Hydraulic Engineering*, 120(1):104-123.

Martinez, C., Miralles-Wilhelm, F. & Garcia, R. 2008. Verification of a 2D finite element debris flow model using Bingham and Cross rheological formulations. *Debris Flows 2008*. Wessex Institute, Ashurst, UK. (Invited paper).

Martinez, C., F.Miralles-Wilhem and R. Garcia-Martinez, 2007. A 2D finite element debris flow model based on the cross rheology formulation. Fourth *International Conference on Debris-Flow Hazards Mitigation: Mechanics, Prediction and Assessment.* Chendu, China.

Mindlin, R.D., 1949. Compliance of elastic bodies in contact. *ASME Journal of Applied Mechanics*, 16:259-268.

Mindlin, R.D. and Deresiewicz, H., 1953. Elastic spheres in contact under varying oblique forces. *ASME Journal of Applied Mechanics*, 20: 327-344.

Miyazawa, N., Tanishima, T., Sunada, K. and Oishi, S. 2003. Debris-flow capturing effect of grid type steel-made sabo dam using 3D distinct element method. *Debris-flow hazards mitigation: mechanics, prediction and assessment*, 1:527-538.

Mustoe G. W. and M. Miyata, 2001. Material Flow Analyses of Non-Circular Shaped Granular Media using Discrete Element Methods, *Journal of Engineering Mechanics*, ASCE., 127 (10): 1017-1026.

Nagurka, M. and Huang, S., 2006. A Mass-Spring-Damper Model of a Bouncing Ball. *International Journal of Engineering Education*, 22 (2):393-401.

O'Brien, J.S. and Julien, P.Y. 1985. Physical properties and mechanics of hyperconcentrated sediment flows. *ASCE Specialty Conference on the Delineation of Landslides, Floods and Debris Flows Hazards*. ASCE, New York, 260-279.

O'Brien, J.S. and Julien, P.Y. 1988. Laboratory analysis of mudflows properties. *Journal of Hydraulic Engineering*, 114(8): 877-887.

O'Donovan, E. J. and Tanner, R. I. 1984. Numerical study of the Bingham squeeze film problem. *Journal of Non-Newtonian Fluid Mechanics*, 15: 75-83.

Parsons, J. D., Whipple, K. X. and Simoni, A. 2001. Experimental Study of the grain-flow, fluid-mud transition in debris flows. *TheJournal of Geology*, 109: 427-447.

Pierson, T. C. 1986. Flow behavior of channelized debris flows. *Hillslope Processes*, 269-296.

Pitman, E. B. and Le, L. 2005. A two-fluid model for avalanche and debris flows. *Philosophical Transactions of the Royal Society*, 363:1573-1601.

Phillips, C. J. and Davies, T. R. H. 1991. Determining rheological parameters of debris flow material. *Geomorphology,* 4:101–110.

Pudasaini, S. P. and Hutter, K. 2003. Rapid shear flows of dry granular masses down curved and twisted channels. Journal of Fluid Mechanics, 495: 193–208.

Savage, S.B. 1984. The mechanics of rapid granular flows. *Advances in Applied Mechanics*, 24: 289–366.

Savage, S.B. and Hutter, K., 1989, The motion of a finite mass of granular material down a rough incline. *Journal of Fluid Mechanics,* 199: 177–215.

Shao, S. & Lo, E.Y. 2003. Incompressible SPH method for simulating Newtonian and Non-Newtonian flows with a free surface. *Advances in Water Resources* 26(7): 787-800.

Takahashi, T. 1978. Mechanical characteristics of debris flow. *Journal of the Hydraulics Division*, ASCE, 104(HY8):1153-1169.

Takahashi, T. 1980. Debris flow on prismatic open channel.. *Journal of the Hydraulics Division*, ASCE, 106(HY3):381-396.

Takahashi, T. 1981. Debris flow. *Annual Reviews of Fluid Mechanics*, 13:57-77.

Takahashi, T. 1991. *Debris Flows*. Rotterdam: Balkema.

Thornton, C., 1997. Coefficient of restitution for collinear collisions of elastic perfectly plastic spheres. *ASME Journal of Applied Mechanics*, 64:383-386.

Thornton, C. and Randall, C.W. 1988. Applications of theoretical contact mechanics to solid particle system simulations. *Micromechanics of Granular Materials,* Ed. J.T. Jenkins and M. Satake, Elsevier, Amsterdam, 133- 142.

Vu-Quoc, L. and Zhang, X. 1999. An accurate and efficient tangential force-displacement model for elastic frictional contact in particle-flow simulations. *Journal of Mechanics of Materials*, 31:235-269.

Walton, O.R., Braun, R.L. 1986. Viscosity, granular-temperature, and stress calculations for shearing assemblies of inelastic, frictional disks. *Journal of. Rheology*, 30 (5):949-980.

Wan, Z. 1982 Bed material movement in hyperconcentrated flow. *Denmark Institute of Hydrodynamics and Hydrology Engineering*, Series Paper 31, Lyngby.

Wildemuth, C. R. and Williams, M. C. 1985. A new interpretation of viscosity and yield stress in dense slurries: coal and other irregular particles. *Rheologica Acta,* 24:75-91.

Wieczorek, G.F., Larsen, M.C., Eaton, L.S., Morgan, B.A. and Blair, J. L. 2001. Debris-flow and flooding hazards associated with the December 1999 storm in coastal Venezuela and strategies for mitigation. *U.S. Geological Survey*, Open File Report 01-0144.

Xu, B. H. and Yu, A. B. 1997. Numerical simulation of the gas-solid flow in a fluidized bed by combining discrete particle method with computational fluid dynamics. *Chemical Engineering Science,* 52: 2785-2809.

APPENDICES

APPENDIX A

Derivation of fluid governing equations
Sample volume *dxdydz:*

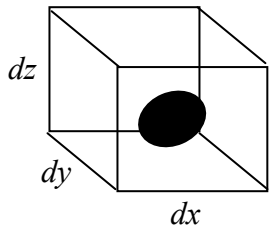

1. <u>Continuity:</u>

$$\rho q_x - \left[\rho q_x + \frac{\partial(\rho q_x)}{\partial t}dx\right] + \rho q_y - \left[\rho q_y + \frac{\partial(\rho q_y)}{\partial t}dy\right] + \rho q_z - \left[\rho q_z + \frac{\partial(\rho q_z)}{\partial t}dz\right] = -\frac{\partial(\rho\, dxdydz)}{\partial t}$$

$$q_x = u dxdydz$$

$$q_y = v dxdydz$$

$$q_z = w dxdydz$$

$$\frac{\partial u}{\partial x} + \frac{\partial v}{\partial y} + \frac{\partial w}{\partial z} = 0$$

Depth integration:

$$\frac{1}{H}\int_0^H \left(\frac{\partial u}{\partial x} + \frac{\partial v}{\partial y} + \frac{w}{\partial z}\right)dz = 0$$

$$\frac{1}{H}\frac{\partial}{\partial x}\int_0^H u\,dz + \frac{1}{H}\frac{\partial}{\partial y}\int_0^H v\,dz + \frac{1}{H}\frac{\partial}{\partial z}\int_0^H w\,dz = 0$$

Applying Leibnitz rule and setting bottom velocities equal to zero gives

$$\frac{1}{H}\left(\frac{\partial(\bar{u}H)}{\partial x} - u(H)\frac{\partial H}{\partial x}\right) + \frac{1}{H}\left(\frac{\partial(\bar{v}H)}{\partial y} - v(H)\frac{\partial H}{\partial y}\right) + \frac{1}{H}w(H) = 0$$

Substituting free surface boundary condition:

$$w(H) = \frac{\partial H}{\partial t} + u(H)\frac{\partial H}{\partial x} + v(H)\frac{\partial H}{\partial y}$$

ends to

$$\boxed{\frac{\partial H}{\partial t}+\frac{\partial(\overline{u}H)}{\partial x}+\frac{\partial(\overline{v}H)}{\partial y}=0}$$

2. <u>x- Momentum:</u>

$$F_x = m\,a_x = \rho\,dxdydz\frac{Du}{Dt}$$

$$Pdydz-\left(P+\frac{\partial P}{\partial x}dx\right)dydz-\tau_{xx}dydz+\left(\tau_{xx}+\frac{\partial\tau_{xx}}{\partial x}dx\right)dydz-\tau_{xz}dxdy+\left(\tau_{xz}+\frac{\partial\tau_{xz}}{\partial z}dz\right)dxdy$$

$$-\tau_{xy}dxdz+\left(\tau_{xy}+\frac{\partial\tau_{xy}}{\partial y}dy\right)dxdz+\rho f_x dxdydz-\sum_{i=1}^{m}F_{Dxi}=\rho dxdydz\frac{Du}{Dt}$$

$$-\frac{\partial P}{\partial x}+\frac{\partial\tau_{xx}}{\partial x}+\frac{\partial\tau_{xz}}{\partial z}+\frac{\partial\tau_{xy}}{\partial y}+\rho f_x-F_{Dx}=\rho\frac{\partial u}{\partial t}+\frac{\partial}{\partial x}(\rho u^2)+\frac{\partial}{\partial y}(\rho uv)+\frac{\partial}{\partial z}(\rho uw)$$

$$\frac{\partial u}{\partial t}+\frac{\partial}{\partial x}(u^2)+\frac{\partial}{\partial y}(uv)+\frac{\partial}{\partial z}(uw)=-\frac{1}{\rho}\frac{\partial P}{\partial x}+\frac{1}{\rho}\left(\frac{\partial\tau_{xx}}{\partial x}+\frac{\partial\tau_{xz}}{\partial z}+\frac{\partial\tau_{xy}}{\partial y}\right)+f_x-\frac{1}{\rho}F_{Dx}$$

Depth integration:

$$\int_0^H\left(\frac{\partial u}{\partial t}+\frac{\partial}{\partial x}(u^2)+\frac{\partial}{\partial y}(uv)+\frac{\partial}{\partial z}(uw)\right)dz=-\frac{1}{\rho}\int_0^H\frac{\partial P}{\partial x}dz+\frac{1}{\rho}\int_0^H\left(\frac{\partial\tau_{xx}}{\partial x}+\frac{\partial\tau_{xz}}{\partial z}+\frac{\partial\tau_{xy}}{\partial y}\right)dz+$$

$$\int_0^H\left(f_x\right)dz-\frac{1}{\rho}\int_0^H F_{Dx}dz$$

Applying Leibnitz rule and setting surface pressure and stresses equal to zero gives

$$\frac{\partial(\overline{u}H)}{\partial t}-u(H)\frac{\partial H}{\partial t}+\frac{\partial(\overline{u}^2H)}{\partial x}-u^2(H)\frac{\partial H}{\partial x}+\frac{\partial(\overline{uv}H)}{\partial y}-u(H)v(H)\frac{\partial H}{\partial y}+u(H)w(H)=$$

$$-\frac{1}{\rho}\frac{\partial}{\partial x}(\overline{P}H)+\frac{1}{\rho}\frac{\partial}{\partial x}(P\overline{\tau}_{xx}H)+\frac{1}{\rho}\frac{\partial}{\partial y}(\overline{\tau}_{xy}H)-\frac{1}{\rho}\tau_{xz}(0)+f_xH-\frac{1}{\rho}F_{Dx}H$$

Substituting free surface boundary condition:

$$w(H)=\frac{\partial H}{\partial t}+u(H)\frac{\partial H}{\partial x}+v(H)\frac{\partial H}{\partial y}$$

and neglecting internal stresses $\bar{\tau}_{xx}$ and $\bar{\tau}_{xy}$, so $\tau_{xz}(0) = \tau_{xz}$ represents the stresses into the fluid and in the bottom, gives:

$$\frac{\partial(\bar{u}H)}{\partial t} + \frac{\partial(\bar{u}^2 H)}{\partial x} + \frac{\partial(\bar{u}\bar{v}H)}{\partial y} = -\frac{1}{\rho}\frac{\partial}{\partial x}(\bar{P}H) - \frac{\tau_{xz}}{\rho} + f_x H - \frac{1}{\rho}F_{Dx}H$$

Now assume hydrostatic pressure so $\bar{P} = \frac{1}{2}\rho g H$, and substitute body force f_x by $(-g\frac{\partial z_b}{\partial x})$

$$\frac{\partial(\bar{u}H)}{\partial t} + \frac{\partial(\bar{u}^2 H)}{\partial x} + \frac{\partial(\bar{u}\bar{v}H)}{\partial y} = -Hg\frac{\partial H}{\partial x} - \frac{\tau_{xz}}{\rho} - Hg\frac{\partial z}{\partial x} - \frac{1}{\rho}F_{Dx}H$$

Doing some math work it is possible to rewrite the equation as

$$\frac{1}{g}\frac{\partial \bar{u}}{\partial t} + \frac{\bar{u}}{g}\frac{\partial \bar{u}}{\partial x} + \frac{\bar{v}}{g}\frac{\partial \bar{u}}{\partial y} + \frac{\partial \eta}{\partial x} + \frac{F_{Dx}}{\rho g} + \frac{\tau_{xz}}{\rho g H} = 0$$

or

$$\frac{1}{g}\frac{\partial \bar{u}}{\partial t} + \frac{\bar{u}}{g}\frac{\partial \bar{u}}{\partial x} + \frac{\bar{v}}{g}\frac{\partial \bar{u}}{\partial y} + \frac{\partial \eta}{\partial x} + \frac{F_{Dx}}{\rho g} + S_{fx} = 0$$

where S_{fx} is the depth integrated stress term that depend on the rheological formulation used to model the slurry.

3. **Stress Term**

Using the quadratic model postulated by O'Brien and Julien (1985)

$$\tau_{xz} = \tau_y + \mu\dot{\gamma} + \zeta\dot{\gamma}^2$$

The first two terms are referred to as the Bingham shear stresses and represent the internal resistance stresses of a Bingham fluid. The last term represents the sum of the dispersive and turbulent shear stresses, which depend on the square of the shear rate.
When the shear stress relationship is depth integrated can be rewritten in the following slope form:

$$S_{fx} = S_y + S_v + S_{td}$$

where

$$S_y = \frac{\tau_y}{\rho g H}$$

Now, assuming a vertical parabolic distribution for velocity u:

$$u(z) = \frac{3u}{H}\left(1 - \frac{z^2}{2H}\right)$$

$$\dot{\gamma}(0) = \frac{\partial u}{\partial z}(0) = \frac{3\bar{u}}{H}$$

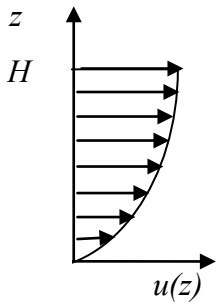

Then,

$$S_v = \frac{\mu\dot{\gamma}}{\rho g H} = \frac{3\mu\bar{u}}{\rho g H^2}$$

For the quadratic term O'Brien and Julien (1985) suggest the use of Manning formula. The Manning formula is an empirical formula for open channel flow, or flow driven by gravity. It was developed by the Irish engineer Robert Manning. The Manning formula states:

$$V = \frac{1}{N} R_h^{2/3} S^{1/2}$$

where V is the cross-sectional average velocity (m/s), N is the Manning coefficient of roughness, R_h is the hydraulic radius (m), and S is the energy gradient (m/m).
The hydraulic radius is defined as the area of the cross section of the channel divided by the length of the wetted perimeter; for example, for a rectangular channel of width b and depth H,

$$R_h = \frac{bH}{(b + 2H)}$$

When b >>H, $R_h \approx H$

Then, Manning formula can be rewritten to express the energy gradient as:

$$S = \frac{N^2 V^2}{H^{4/3}} \quad \text{or}$$

$$S_{td} = \frac{N^2 \bar{u}^2}{H^{4/3}}$$

The Manning coefficient of roughness *N*, is an empirically derived coefficient, which is dependent on many factors, including bottom surface roughness and sinuosity. Values typically range between 0.02 for smooth and straight rivers, to 0.075 for sinuous rivers and creeks with excess debris on the river bottom or river banks.
Finally, for the quadratic rheological model of O'Brien and Julien, the depth integrated stress term is

$$S_{fx} = \frac{\tau_y}{\rho g H} + \frac{3\mu\overline{u}}{\rho g H^2} + \frac{N^2\overline{u}^2}{H^{4/3}}$$

When the quadratic model of O'Brian and Julien is combined with the Cross formulation,

$$\tau_{xz} = \mu_{eff}\dot{\gamma} + \zeta\dot{\gamma}^2$$

and the depth integrated stress term results

$$S_{fx} = \frac{\mu_{eff}\dot{\gamma}}{\rho g H} + \frac{N^2\overline{u}^2}{H^{4/3}}$$

with $\dot{\gamma} = \frac{3\overline{u}}{H}$, $\mu_{eff} = \frac{\mu_0 + \mu_\infty K_B\dot{\gamma}}{1 + K_B\dot{\gamma}}$, $K_B = \frac{\mu_0}{\tau_y}$, $\mu_\infty = \mu$ and $\mu_0 = 10^3\mu$.

APPENDIX B

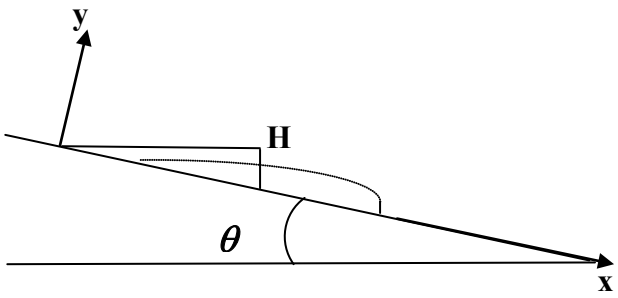

Equations of motion are reduced to the following form

$$\frac{\partial u}{\partial x}+\frac{\partial v}{\partial y}=0$$

$$\rho\left(\frac{\partial u}{\partial t}+u\frac{\partial u}{\partial x}+v\frac{\partial u}{\partial y}\right)=-\frac{\partial p}{\partial x}+\rho gSin\theta+\frac{\partial \tau}{\partial y}=0$$

$$\frac{\partial p}{\partial y}=-\rho gCos\theta$$

Where ρ is fluid density, g is acceleration of gravity, p is pressure and (u,v) are the flow velocity components in (x,y) directions respectively. The boundary conditions are:

$$p=0,\quad \tau=0 \qquad at \quad y=h$$

Then, since pressure in the mudflow is hydrostatic and given by:

$$p=\rho g(h-y)\cos\theta$$

Now consider the two layer-model shown in figure 2: The flow is divided into a plug layer, with uniform velocity U_p and depth h_p, and a shear layer with varying velocity u and depth h_s. For the case of steady, uniform flow the velocity distribution is given by

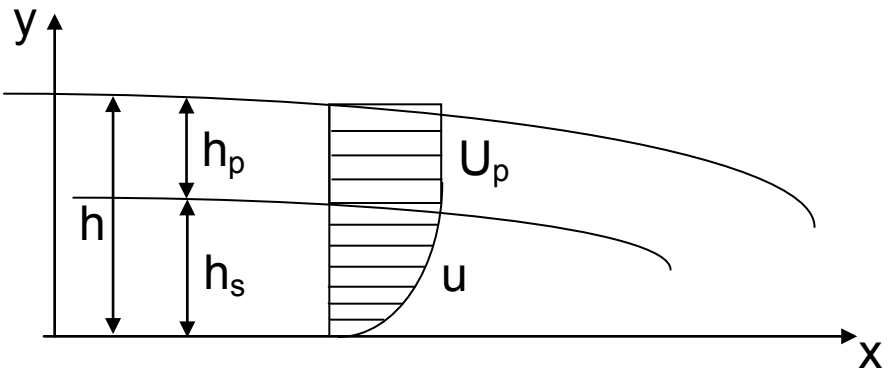

Figure 2

$$u = U_p \quad h_s \le y \le h$$

$$u = U_p\left(\frac{2y}{h_s} - \frac{y^2}{h_s^2}\right) \quad 0 \le y \le h$$

and the flow rate per unit width is

$$q = U_p \frac{(3h - h_s)}{3}$$

Assuming that this is also valid for non-uniform boundary layer flows without committing serious errors (with U_p changing with x and time t), the following depth-integrated momentum and continuity equations are obtained taking into account the surface boundary condition

$$v = \frac{\partial h}{\partial t} + U_p \frac{\partial h}{\partial x} \qquad at \quad y = h$$

Continuity:

$$\frac{\partial h}{\partial t} + \frac{\partial q}{\partial x} = 0 \qquad with \qquad q = U_p\left(h - \frac{h_s}{3}\right)$$

Momentum balance in the shear layer:

$$\frac{\partial}{\partial t}\left(\frac{2}{3}U_p h_s\right) + \frac{\partial}{\partial x}\left(\frac{8}{15}U_p^2 h_s\right) - U_p\left(\frac{\partial h_s}{\partial t} + \frac{\partial}{\partial x}\left(\frac{2}{3}U_p h_s\right)\right) = g h_s\left(\sin\theta - \frac{\partial h}{\partial x}\cos\theta\right) - \frac{2\mu U_p}{\rho h_s}$$

Momentum balance in the plug layer:

$$\frac{\partial U_p}{\partial t} + \frac{\partial}{\partial x}\left(\frac{U_p^2}{2} + gh\cos\theta\right) = g\sin\theta - \frac{\tau_y}{\rho(h-h_s)}$$

These three equations could be solve numerically to look for the unknowns h, U_p and h_s**;** however, studying the relative magnitudes of the terms in these equations it is possible to derive first-order solutions for the outer and inner regions of the flow.

OUTER SOLUTION

The relative magnitudes of the terms in the equations above are evaluated by introducing a number of scales as follows:

$$(h^*, h_s^*, U_p^*, x^*, t^*, \varepsilon, \lambda, Fr) = \left(\frac{h}{h_0}, \frac{h_s}{h_0}, \frac{U_p}{U_0}, \frac{x}{l}, \frac{t}{U_0 l}, \frac{h_0}{l}, \frac{h_y}{h_0}, \frac{U_0}{\sqrt{gh_0}}\right)$$

In which l = length scale in x, h_o = length scale in y, Fr = Froude number, $\varepsilon << 1$, U_0 = velocity scale given by

$$U_0 = \frac{\rho g h_0^2 \sin\theta}{3\mu}$$

and h_y = yield depth defined by

$$\tau_y = \rho g h_y \sin\theta$$

Introducing the scales into the governing equations yields to the dimensionless form of the governing equations, when considering $\varepsilon / sin\theta << 1$ these equations reduce to the kinematic-wave approximations given by:

$$\frac{\partial h^*}{\partial t^*} + \frac{\partial q^*}{\partial x^*} = 0$$

$$U_p^* = \frac{3h_s^{*2}}{2}$$

$$h - h_s = \lambda$$

$$h^* > \lambda$$

Substituting q^* and using the chain rule, yields two ordinary differential equations, such that

$$\frac{\partial h^*}{\partial t^*} = 0$$

along characteristic curves

$$\frac{\partial x^*}{\partial t^*} = 3h_s^{*2} - 3h^*\lambda$$

in the *(x*,t*)* plane.

To see the solution of a flow from a source of finite size, as an example, a dam break of mud-slide problem with initial triangular shape on a slope is considered.

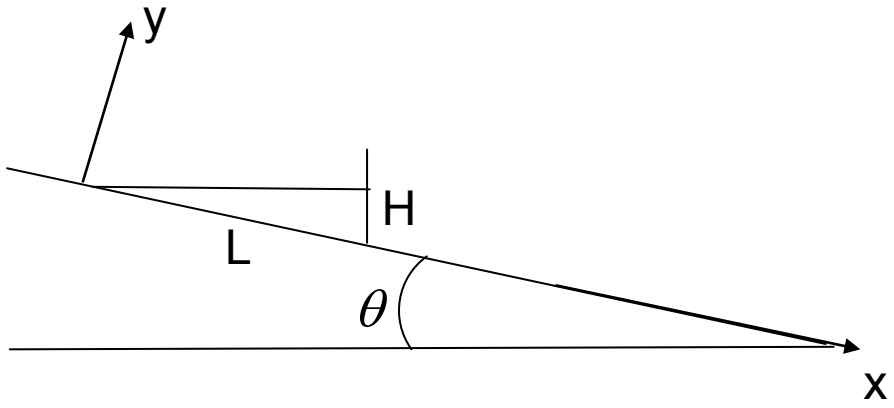

If the length scales are $h_0 = H \quad and \quad l = L$, the initial conditions will be:

$$h^*(x^*, 0) = x^* \qquad 0 \le x^* \le 1$$
$$h^*(x^*, 0) = 0 \qquad -\infty \le x^* \le 0 \quad or \quad 1 \le x^* \le \infty$$

Here, L is the initial length of the soil mass; and H is the maximum depth of the soil mass. Integrating the governing equations above with the help of these boundary conditions gives:

$$x^* = (3h^{*2} - 3h^*\lambda)t^* + h^*$$

A relation that holds in the *(x*, t*)* plane only and allows to solve for the depth of the fluid *h** at any time *t** and location x*. Since it is a nonlinear relation, it could be solved by using a numerical procedure as Newton-Raphson.

The shock location is determined invoking mass conservation, since it is assumed that the mass of fluid remains constant with time. Then

$$A^* = \int_{\lambda}^{x_f^*} h^* dx^* \quad = \frac{(1-\lambda^2)}{2}$$

gives the relation:

$$x_f^* = \frac{3h_f^{*2} - 3h_f^*\lambda + h_f^{*4} - h_f^*\lambda^3}{4h_f^{*3} - 3h_f^{*2}\lambda - \lambda^3}$$

Then x_f* yields the time at which the flow depth just upstream of the shock is h_f*, such that

$$t^* = \frac{1 - h_f^{*2}}{4h_f^{*3} - 3h_f^{*2}\lambda - \lambda^3}$$

The above solution is the first order outer approximation. This solution is valid everywhere (red solution, figure 3), except near the shock, where the boundary layer assumptions are violated, i.e., $\frac{\partial h^*}{\partial x^*}$ is not small anymore. An inner solution that is valid near the shock can be found by using different variables to rescale the governing equations.

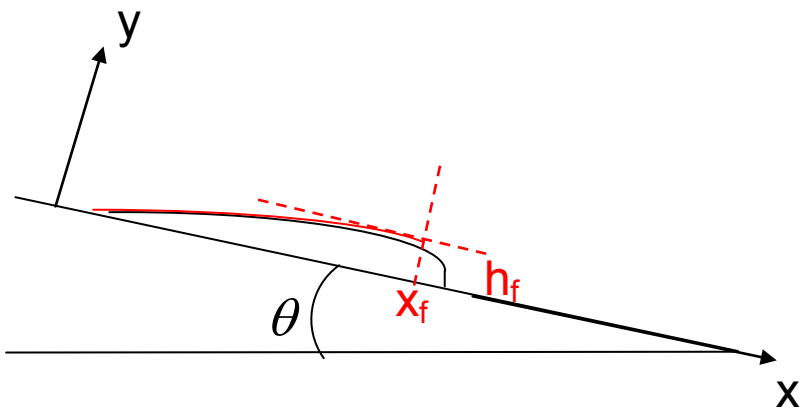

INNER SOLUTION

Let's now introduce the following inner variables to rescale the governing equations:

$$(h_i^*, h_{si}^*, \xi^*, U_i^*, U_{pi}^*, t_i^*) = (\frac{h}{h_0}, \frac{h_s}{h_0}, \frac{x^* - x_f}{\varepsilon}, \frac{u}{U_0}, \frac{U_p}{U_0}, \frac{t}{U_0 l})$$

Substituting these scales into the continuity equation and taking the limit $\varepsilon \to 0$, integrating over the depth, and taking into account that h_i* vanishes at the leading edge for any time t, yields to

$$U_i^* = \frac{\partial x_f^*}{\partial t^*}$$

which shows that velocities near the shock change only with time. Then, in a similar way momentum equations yield to

$$h_{si}^* \frac{\partial h_i^*}{\partial \xi^*} \cos\theta = \left(h_{si}^* - \frac{2U_{pi}^*}{3h_{si}^*} \right) \sin\theta$$

$$(h_i^* - h_{si}^*) \frac{\partial h_i^*}{\partial \xi^*} \cos\theta = \left(h_i^* - h_{si}^* - \lambda \right) \sin\theta$$

Then, it is possible to derive a differential equation for the free surface profile near the shock as

$$\frac{\partial h_i^*}{\partial \xi^*} = \left[1 - \frac{\lambda}{h_i^*} - \frac{\sqrt{(h_f^* - \lambda)^4 + 4h_i^* \lambda (h_f^* - \lambda)^2} + (h_f^* - \lambda)^2}{2h_i^{*2}} \right] \tan\theta$$

which matches the outer solution correctly since $h_i^* \to h_f^*$ as $\xi^* \to -\infty$. This equation can be easily solve using some numerical method as Runge-Kutta; however, since the right hand side is independent on ξ^*, the location of the profile is unknown. The right place will be given under the condition of mass conservation given by

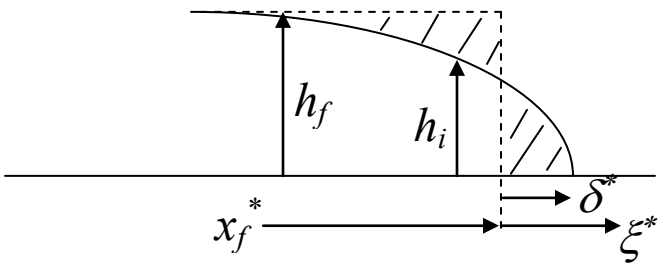

$$\int_{-\infty}^{0} (h_f^* - h_i^*) d\xi^* = \int_{0}^{\delta^*} h_i^* d\xi^*$$

where δ* is defined as the distance from x_f to the leading edge of the shock.

The outer and inner solutions in the above can be expressed in dimensional forms with the help of the scales introduced. Thus, the final solution will be given by a composite solution given by

$$h_c = h + h_i - h_f \qquad x \le x_f$$

$$h_c = h_i \qquad x \succ x_f$$

APPENDIX C

The following tables include measurements of debris flow, flood deposits and boulder size values done by USGS in 2001. USGS Report 01-0144.

Map no.	Slope, in degrees	Flow depth		Deposit thickness, in m	Channel width, in m	Boulder size, in m			Maximum boulder size, in m					Superelevation		Flow velocity, in m/s		Comments
		left, in m	right, in m			50%	75%	90%	A axis	B axis	C axis	Volume, in m³	Nom. diam. cube (sphere)	in degrees	velocity, in m/s	Costa, 1983	Clarke, 1996 cube (sphere)	
San Julián (channel)																		
7–10–1	5.0	3.5	–	3.5	172.0	–	–	–	3.1	2.6	1.0	8.1	2.01 (2.49)	–	–	8.3	5.2 (5.7)	Gneissic boulder.
7–10–1	–	–	–	–	–	–	–	–	3.6	3.0	1.2	13.0	–	–	–	–	–	–
7–10–2	3.0–3.5	–	–	1.7	181.0	–	–	2.5	–	–	–	–	–	–	–	–	–	–
7–10–2	3.0–3.5	–	–	7.0	–	–	–	0.5	–	–	–	–	–	–	–	–	–	Sequence of three old debris-flow deposits with combined thickness of 7 m capped by new deposits.
7–10–3	3.5–5.0	–	–	3.0	111.0	–	–	–	5.3	2.7	1.9	27.2	3.00 (.73)	–	–	8.4	6.3 (6.9)	Gneissic boulder supported in matrix.
7–10–3	–	–	–	–	–	–	–	–	5.9	3.3	1.5	29.2	3.08 (3.92)	–	–	9.3	6.3 (7.0)	Gneissic boulder supported in matrix.
4–5–1	–	–	–	2.5	–	–	0.75	–	–	–	–	–	–	–	–	–	–	–
7–10–4	4.0–5.0	–	–	3.0–6.0	135.0	–	–	–	6.3	2.0	1.9	23.9	2.88 (3.58)	–	–	7.3	6.1 (6.8)	Dark-colored gneissic boulder within a sandy gravel matrix.
7–10–4	–	–	–	–	–	–	–	–	4.4	2.6	1.8	20.8	2.74 (3.40)	–	–	8.3	6.0 (6.6)	–
4–5–2	–	–	–	3.0	–	–	1.0–2.0	–	–	–	–	–	–	–	–	–	–	Central depositional part of channel.
4–5–3	3.0	2.5	–	1.0	–	–	–	–	–	–	–	–	–	–	–	–	–	–
4–5–4	2.5–3.5	1.5	–	–	75.0	–	2.0	–	–	–	–	–	–	–	–	–	–	–
4–5–5	–	–	–	–	–	–	–	–	2.0–3.0	–	–	–	–	–	–	–	–	–
4–5–6	3.0–4.0	–	–	1.0	–	–	–	–	5.6	5.2	3.9	113.6	4.84 (6.00)	–	–	11.6	7.9 (8.7)	–
4–5–6	–	–	–	–	–	–	–	–	5.5	5.2	1.8	45.76	3.58 (4.43)	–	–	11.6	6.8 (7.5)	–
4–5–7	14.0	–	–	–	–	1.20	–	–	3.0–4.0	–	–	–	–	–	–	–	–	Debris flow entering main channel from tributary channel of Quebrada las Choras; debris flows split community of San Julián.
7–10–5	5.5	–	–	>10.0	129.0–145.0	–	–	–	3.0	2.1	1.5	9.5	2.11 (2.62)	–	–	7.5	5.3 (5.9)	Gneissic boulder.
7–10–5	–	–	–	–	–	–	–	–	4.4	4.2	2.5	46.2	3.59 (4.45)	–	–	10.5	6.8 (7.6)	Semi-rounded gneissic boulder deposited near center of channel.
7–10–6	–	–	–	–	145.0	–	–	2.0–3.0	–	–	–	–	–	–	–	–	–	Top of old debris-flow terrace 17.4 m above present-day channel level; 8-cm-thick carbon-rich layer over old debris flow with 2- to 3-m-size boulders at 7.3 m above present-day channel level.
7–10–7	6.0	11.0	–	9.0	140.0	–	–	–	4.8	1.8	1.4	12.1	2.30 (2.85)	–	–	6.9	5.5 (6.1)	Gneissic boulder.
4–5–8	–	–	–	–	–	–	–	–	5.0	2.6	1.0	13.0	2.35 (2.92)	–	–	8.3	5.6 (6.2)	Matrix of debris flow protected under rock; 11 of the largest boulders measured at this location.
7–10–8	5.5–6.0	10.6	–	10.6	75.0	–	–	–	3.6	2.3	1.9	15.7	2.51 (3.11)	–	–	7.8	5.7 (6.4)	Gneissic boulder deposited at constriction point of channel.
7–10–9	4.0	–	–	–	71.0	–	–	3.5	–	–	–	–	–	–	–	–	–	Many boulders greater than 3 m deposited on upper bench of channel.
7–10–10	6.0–6.5	–	–	5.0	98.0	–	–	2.5	6.0	5.3	1.8	57.2	3.85 (4.76)	–	–	11.7	7.0 (7.8)	Old debris-flow terrace on east side of channel with semi-rounded gneissic boulders of 2.5 m deposited about 5 to 7 m above level of present-day channel.
7–10–11	5.5	–	–	6.0	131.0	–	–	–	6.9	4.1	2.9	82.0	4.35 (5.39)	–	–	10.3	7.5 (8.3)	Gneissic boulder.
4–5–9	–	–	–	3.5	–	–	–	–	1.0–2.0	–	–	–	–	–	–	–	–	Islands of bouldery debris-flow deposits incised 2 to 3 m deep by subsequent flooding.
7–10–12	5.0–6.0	–	–	4.0	113.0	–	–	1.5	–	–	–	–	–	–	–	–	–	–
4–5–10	4.0	5.0	12.0	4.0	71.0	–	–	–	2.0–3.0	–	–	–	–	–	–	–	–	Sequence of recent debris flow, flood, debris flow, exposed in 4-m-thick section over old debris-flow deposits; channel eroded to schist bedrock; middle of channel filled with blocky debris.
7–10–13	5.0	5.0	–	4.0	90.0–94.0	–	–	–	9.5	5.9	2.6	145.7	5.26 (6.53)	–	–	12.3	8.2 (9.1)	Dark-banded gneissic boulder supported in matrix; boulder plucked out from nearby outcrop.
7–10–13	5.0	–	–	–	–	–	–	–	6.2	5.8	4.0	143.8	5.24 (6.50)	–	–	12.2	8.2 (9.1)	Boulders supported in matrix of old debris flow.
7–10–13	5.0	–	–	–	–	–	–	–	7.2	6.6	3.8	180.6	5.85 (7.01)	–	–	13.0	8.5 (9.4)	Boulders supported in matrix of old debris flow.
4–5–11	–	–	–	–	–	–	–	–	–	–	–	–	–	–	–	–	–	Intact island of old debris-flow deposits topped with recent debris-flow deposits in middle of channel; slightly raised bedrock bench on one side of channel; steep north-dipping foliation in bedrock.
7–10–14	4.0–4.5	12.5	–	4.0	96.0	–	–	–	3.4	2.7	1.8	14.7	2.45 (3.04)	–	–	8.4	5.7 (6.3)	Trim line from flood 12.5 m above present-day level of channel; much higher than trim line from debris flow; gneissic boulder.
7–10–15	4.5	–	–	0.5	95.0	–	–	–	–	–	–	–	–	–	–	–	–	Mostly erosional scour in narrow channel; only thin layer of deposition remaining on high terrace.
4–5–12	2.0–3.0	3.0	3.0	–	95.0	–	–	–	10.4	8.4	4.8	419.3	7.48 (9.29)	–	–	14.7	9.7 (10.7)	Boulder moved(?)—all sides of boulder appear to be fresh and unweathered; some parts of boulder are covered by fresh deposits.
7–10–16	3.5–4.5	12.0	–	>2.0	66.0	–	–	–	8.4	6.4	3.2	172.0	5.56 (6.90)	–	–	12.8	8.4 (9.3)	New 2-m-thick debris-flow deposit atop old terrace.
4–5–13	6.0–7.0	6.0	–	–	–	–	–	–	–	–	–	–	–	–	–	–	–	Evidence of debris flows in main and tributary channels . Debris flow in main channel on a slope of 6° to 7° carried the largest boulders; subsequent debris flow from tributary channel on a 15° slope crossed and temporarily blocked main channel.
4–5–14	15.0	–	–	1.5	–	–	–	2.0	–	–	–	–	–	–	–	–	–	Large boulders imbricated over inclined, sandy pre-event(?) surface.
4–5–15	6.0–7.0	–	–	5.0	–	–	–	2.5	–	–	–	–	–	–	–	–	–	Thick bouldery debris-flow deposit incised just below junction of tributary.
7–10–17	7.0	–	–	1.0–3.0	40.0	–	–	–	14.6	13.8	6.5	1309.6	10.90 (13.57)	–	–	18.7	11.8 (12.9)	Old very rounded gneissic boulder at edge of channel; recent deposit, 1 to 3 m thick, plastered against old debris-flow terrace.
7–11–1	6.0–6.5	8.7	–	1.0–1.5	49.0	–	–	–	–	–	–	–	–	–	–	–	–	At western tributary channel, erosional zone with only 1 to 1.5 m of deposition; old 5-m-thick debris-flow terrace of angular to semi-rounded gneissic boulders about 9 m above present-day level of channel.
7–11–2	16.0	–	–	–	–	–	–	–	7.0	5.0	4.0	140.0	5.19 (6.44)	–	–	11.4	8.1 (9.0)	Steep side channel of fault zone(?) near main channel of Río San Julián.
7–11–3	4.5–7.0	10.9	–	1.0	43.0	–	–	–	–	–	–	–	–	–	–	–	–	Erosional section with step-like, irregular topography of bedrock in channel.
7–11–4	–	12.5	–	–	31.0	–	–	–	8.2	5.9	4.0	193.5	5.78 (7.18)	–	–	12.3	8.6 (9.5)	Semi-rounded boulder of augen gneiss; eyewitness reports area was terrace with mangrove trees; pothole eroded into bedrock indicates previous exposure.
7–11–5	5.0–7.0	7.3	–	–	31.0	–	–	–	18.4	11.5	9.5	740.6	9.05 (11.23)	–	–	17.1	10.6 (11.8)	Large boulder moved and jammed into place in steep scoured section of channel with irregular sloped surface.
7–11–6	–	10.0	–	–	34.0	–	–	2.0	–	–	–	–	–	–	–	–	–	Old rounded boulder exposed in debris-flow terrace 14 m above present-day level of stream; multiple bedrock steps in channel.
7–11–7	8.5	12.7	–	–	40.0	–	–	1.5	–	–	–	–	–	–	–	–	–	Main channel completely scoured exposing bedrock; side channels choked with boulders; semi-rounded boulders are seen within old debris-flow terraces.
7–11–8	10.0–14.0	12.0	–	–	18.0	–	–	–	–	–	–	–	–	–	–	–	–	U-shaped channel in bedrock without any remaining deposits.

Map no.	Slope, in degrees	Flow depth		Deposit thickness, in m	Channel width, in m	Boulder size, in m			Maximum boulder size, in m					Superelevation		Flow velocity, in m/s		Comments
		left, in m	right, in m			50%	75%	90%	A axis	B axis	C axis	Volume, in m³	Nom. diam. cube (sphere)	in degrees	velocity, in m/s	Costa, 1983	Clarke, 1998 cube (sphere)	
San Julián (Carabalileda fan)—Continued																		
7-6-1	3.0–3.5	2.0	–	–	–	–	–	–	2.0	1.5	1.0	3.0	1.44 (1.79)	–	–	6.3	4.4 (4.9)	At eastern end of highway bridge.
7-6-2	4.0	3.5	–	–	96.0	–	–	–	2.9	2.3	2.2	14.7	–	–	–	–	–	Semi-rounded gneissic boulder.
7-6-2	–	–	–	–	–	–	–	–	4.3	2.5	2.1	22.6	–	–	–	–	–	Semi-angular gneissic boulder.
7-6-2	–	–	–	–	–	–	–	–	4.0	3.1	2.1	26.0	2.96 (3.68)	–	–	9.0	6.2 (6.9)	Semi-angular gneissic boulder.
7-6-3	4.0	2.3	–	–	188.0	–	1.3	–	–	–	–	–	–	–	–	–	–	–
7-6-4	3.0	1.0	–	–	128.0	–	–	–	–	–	–	–	–	–	–	–	–	–
7-6-5	2.0–3.0	2.0	–	–	213.0	–	–	–	3.9	3.1	1.6	19.3	2.68 (3.33)	–	–	9.0	5.9 (6.8)	Semi-angular boulder.
7-6-6	4.0	1.7	–	–	79.0	–	–	–	4.0	2.4	2.2	21.1	–	–	–	–	–	Boulders overflowed channel at bend.
7-6-6	–	–	–	–	–	–	–	–	4.1	3.8	3.0	46.7	3.60 (4.47)	–	–	10.0	6.8 (7.6)	Thinning deposits as debris flow spreads at bend in channel.
7-6-7	3.0	3.0–6.0	–	–	434.0	–	–	–	5.3	2.1	1.7	18.9	2.66 (3.31)	–	–	7.5	5.9 (6.8)	Semi-angular boulder.
7-6-8	3.5–4.0	>4.0	–	–	–	–	–	–	5.9	2.8	1.1	18.2	2.63 (3.26)	–	–	8.6	5.9 (6.5)	Tabular boulder.
7-6-9	4.5	4.0	–	–	–	–	–	–	4.1	3.5	1.4	20.1	2.72 (3.37)	–	–	9.6	6.0 (6.8)	Debris flow completely buried first floors of houses.
7-6-10	4.5	5.0	–	–	–	–	–	–	–	–	–	–	–	–	–	–	–	Fine-grained deposits on top of matrix-supported debris flow.
7-6-11	3.0–3.5	2.0–2.5	–	–	–	–	–	–	6.5	5.7	1.3	48.2	3.64 (4.51)	–	–	12.1	6.9 (7.6)	At intersection with main highway.
7-6-11	–	–	–	–	–	–	–	–	5.0	2.3	1.6	18.4	–	–	–	–	–	Tabular boulder.
7-6-12	3.5	2.5–3.0	–	–	–	–	–	3.0	4.4	3.3	1.6	23.2	2.85 (3.54)	–	–	9.3	6.1 (6.8)	Boulders deposited on high-rise patio; large boulders within matrix deposited above road.
7-6-13	–	–	–	–	–	–	–	–	0.5	–	–	–	–	–	–	–	–	Old debris-flow terrace up to 5 m thick.
7-6-14	4.5–6.0	3.0	–	–	–	–	–	2.0	5.2	–	–	–	–	–	–	–	–	Old debris-flow terrace, 17 m high, displays a sequence of at least four events; yellowish-brown, sandy matrix.
7-6-15	–	–	–	–	–	–	–	–	1.5	–	–	–	–	–	–	–	–	Old debris-flow terrace.
7-7-1	2.5–3.0	1.8–2.5	–	–	–	–	–	1.0	–	–	–	–	–	–	–	–	–	Sequence of three events with a capping debris flow.
7-7-2	3.0–3.5	2.0–2.5	–	–	267.0	–	–	1.0	–	–	–	–	–	–	–	–	–	Sandy gravel deposits.
7-7-3	2.5	1.0–1.5	–	–	–	–	–	–	–	–	–	–	–	–	–	–	–	Fine-grained sandy deposits with little structural damage.
7-7-4	3.5	1.8–2.0	–	–	–	–	–	–	3.1	2.6	1.4	11.3	–	–	–	–	–	Semi-angular boulder.
7-7-4	–	–	–	–	–	–	–	–	3.9	2.7	2.2	23.2	2.85 (3.54)	–	–	8.4	6.1 (6.8)	Blockage of large boulders and tree trucks protected house downstream.
7-7-5	4.0	2.5–3.0	–	–	238.0	–	–	2.0	–	–	–	–	–	–	–	–	–	Debris blockage.
7-7-6	3.0	0.5	–	–	239.0	–	–	<0.5	–	–	–	–	–	–	–	–	–	Sandy deposits on a side street perpendicular to flow direction.
7-7-7	4.0	2.0	–	–	–	–	–	–	1.8	1.3	0.7	1.6	1.18 (1.48)	–	–	5.8	4.0 (4.4)	Gravelly sand deposits.
7-7-8	5.0–5.5	2.0	–	–	–	–	–	–	–	–	–	–	–	–	–	–	–	Old debris-flow boulders incorporated within wall and partially buried in lawn.
7-7-9	2.0–2.5	1.0	–	–	–	–	–	1.0	–	–	–	–	–	–	–	–	–	Old debris-flow terrace >5 m thick with schistose and gneissic boulders.
7-7-10	3.5–4.0	1.5	–	–	–	–	–	<0.5	–	–	–	–	–	–	–	–	–	Little damage to trees along road; impact marks no higher than 0.5 m.
7-7-11	3.5	0.5–1.0	–	–	–	–	–	1.0	2.1	1.3	0.7	1.9	1.24 (1.54)	–	–	5.9	4.1 (4.5)	A few large boulders within coarse-grained sandy deposits; flow through irregular topography in yards between houses.
7-7-12	4.0	2.5	–	2.0	–	–	–	–	5.5	4.2	1.2	27.7	3.02 (3.75)	–	–	10.5	6.3 (7.0)	Flow deposits of very coarse grained sand distributed along street.
7-7-13	5.5	2.0	–	–	–	–	–	2.0	–	–	–	–	–	–	–	–	–	Large boulders filling house and yard causing collapse of wall.
7-7-14	6.0–7.0	2.0–3.0	–	–	–	–	–	1.5	–	–	–	–	–	–	–	–	–	Large boulders supported by sandy matrix.
7-7-15	4.0	1.75	–	–	–	–	–	2.5	–	–	–	–	–	–	–	–	–	–
7-7-16	6.0	2.5	–	–	–	–	–	2.5	–	–	–	–	–	–	–	–	–	Small boulders, 20 to 30 cm in size, in gravelly, sandy matrix that has some laminations.
7-7-17	5.0–6.0	–	–	–	–	–	–	–	2.8	1.3	0.8	2.9	1.43 (1.77)	–	–	5.9	4.4 (4.9)	At Plaza de Piedras, old debris-flow boulders distributed around house built in 1917.
7-7-18	–	–	–	–	–	–	–	–	4.0	–	–	–	–	–	–	–	–	Old schistose, debris-flow boulders exposed in 15-m-high roadcut in red soils.
7-7-19	5.0	3.0	–	–	–	–	–	2.0–2.5	2.5	2.5	2.5	15.6	2.5	–	–	8.1	5.7	Cubed-shaped gneissic boulder.
7-7-20	4.0	–	–	–	–	–	–	–	2.7	–	–	–	–	–	–	–	–	Side channel with 3.5-m-high exposure of three old debris-flow events, with mostly schistose boulders but rare gneissic boulders.
7-7-21	6.0	–	–	–	17.0	–	–	–	1.0	–	–	–	–	–	–	–	–	Side channel with 3-m-high incised box-shaped channel exposing three old debris-flow events; lowest deposit has cemented matrix and gneissic boulders.
7-7-22	5.0–6.0	>2.5	–	–	141.0	–	–	–	2.5	2.0	1.7	8.5	2.04 (2.53)	–	–	7.3	5.2 (5.8)	Along Río San Julián near village of San Julián, a 15-m-high exposure with three units: debris flow, fluvial, and debris flow topped by red soil; lowest unit has tan-colored 2-m-size boulders.
7-8-1	3.0–4.0	–	–	2.5	50.0	–	–	–	4.8	4.4	2.4	50.7	3.70 (4.59)	–	–	10.7	6.9 (7.7)	Along Avenida Principal, one block from old shoreline; coarse-grained, sandy matrix atop gneissic boulders.
7-8-1	–	–	–	–	–	–	–	–	4.8	2.8	1.4	18.8	–	–	–	–	–	–
7-8-2	3.5	–	–	1.7	–	–	–	–	4.5	3.8	1.0	17.1	2.58 (3.20)	–	–	10.0	5.8 (6.4)	Along Avenida Principal, 1/2 block from old shoreline.
7-8-3	1.0	1.1	–	–	–	–	–	–	–	–	–	–	–	–	–	–	–	No boulders found at old shoreline.
7-8-4	1.5	–	–	2.2	–	–	–	–	2.5	1.5	0.8	3.0	–	–	–	–	–	–
7-8-4	–	–	–	–	–	–	–	–	3.8	2.0	1.6	12.2	2.30 (2.85)	–	–	7.3	5.5 (6.1)	Gneissic boulders reached road at old shoreline.
7-8-5	3.5	2.3	–	–	13.0	–	–	–	1.3	0.9	0.8	0.9	0.98 (1.21)	–	–	4.9	3.8 (4.1)	Flow between buildings using road as the channel.
7-8-6	–	0.6	–	–	–	–	–	–	–	–	–	–	–	–	–	–	–	Eyewitness reported that large boulders had been removed subsequent to the event.
7-8-7	3.0	1.8–2.0	–	3.4	–	–	–	–	0.9	0.6	0.5	0.3	0.85 (0.80)	–	–	4.1	3.0 (3.3)	Resident reported amount of material removed was 3.4 m thick.
7-8-8	3.0	1.4–1.7	–	–	–	–	–	–	1.6	1.1	0.9	1.6	1.17 (1.45)	–	–	5.5	4.0 (4.4)	Flow traveled between houses.
7-8-9	–	1.4	–	–	–	–	–	–	2.3	2.2	1.2	6.1	1.82 (2.26)	–	–	7.6	4.9 (5.5)	Very irregular benched slope.
7-8-10	2.5–3.5	1.5	–	–	–	–	–	–	3.1	2.0	0.9	5.6	1.77 (2.20)	–	–	7.3	4.9 (5.4)	Gneissic boulder.
7-8-11	3.5	4.2	–	–	–	–	–	–	2.1	1.7	0.8	2.9	1.42 (1.76)	–	–	6.7	4.4 (4.8)	Old debris-flow deposit beneath foundation of crushed house.
7-8-12	–	–	–	2.7	–	–	–	–	–	–	–	–	–	–	–	–	–	–
7-8-13	3.5–4.5	–	–	>3.0	–	–	–	1.0	3.8	2.9	1.7	18.7	2.66 (3.30)	–	–	8.7	5.9 (6.5)	Bouldery deposit filling first floor of building; 1-m-size boulders deposited atop roof.
7-8-13	–	–	–	–	–	–	–	–	4.8	4.8	2.0	46.1	3.59 (4.45)	–	–	11.2	6.8 (7.5)	Boulder from old debris-flow event; street eroded and served as channel.
7-8-14	4.0	2.5	–	2.0	–	0.75	–	–	3.1	2.4	1.9	14.1	2.42 (3.00)	–	–	8.0	5.6 (6.3)	About 1 m of erosion beneath road level.
7-8-15	–	–	–	–	–	–	–	–	6.0	3.4	1.3	26.5	2.98 (3.70)	–	–	9.4	6.2 (6.9)	Schistose boulder of old debris-flow deposit incorporated within foundation of house.
7-8-16	5.0	–	–	2.0–3.0	–	–	–	–	5.8	4.3	1.7	40.9	3.45 (4.28)	–	–	10.8	6.7 (7.4)	Within a large deposit of boulders, one boulder within matrix rests on steel rebar from building foundation.

Map no.	Slope, in degrees	Flow depth		Deposit thickness, in m	Channel width, in m	Boulder size, in m			Maximum boulder size, in m					Superelevation		Flow velocity, in m/s		Comments
		left, in m	right, in m			50%	75%	90%	A axis	B axis	C axis	Volume, in m³	Nom. diam. cube (sphere)	in degrees	velocity, in m/s	Costa, 1983	Clarke, 1996 cube (sphere)	
San Julián (Caraballeda fan)—Continued																		
7–8–17	2.5	–	–	2.0	–	–	–	3.5	–	–	–	–	–	–	–	–	–	Old 1-m-size boulder in matrix of red soil beneath recent debris-flow deposits; local irregular stepped topography.
7–8–18	3.5–4.0	–	–	1.5	–	1.0	–	–	4.3	3.2	2.5	34.4	3.25 (4.04)	–	–	9.2	6.5 (7.2)	–
7–8–19	4.0	–	–	2.0	–	0.3–0.4	–	–	6.1	3.5	2.6	55.5	3.81 (4.73)	–	–	9.6	7.0 (7.8)	Gneissic boulder is largest within deposit, but schistose boulders also present.
7–8–20	2.5–3.0	–	–	2.0	–	–	–	–	7.2	6.1	1.6	70.3	4.13 (5.12)	–	–	12.8	7.3 (8.1)	Site of partially collapsed apartment house on upper part of fan; schistose boulder collapsed into channel, eroded by late-stage flooding; 3.5-m-size boulders deposited on second floor of structure.
7–8–21	4.0	1.0	–	1.0	–	–	–	1.0	–	–	–	–	–	–	–	–	–	–
7–8–22	4.0	–	–	1.5–2.5	183.0	–	–	–	3.5	3.2	1.9	21.3	2.77 (3.44)	–	–	9.2	6.0 (6.7)	–
7–8–23	4.0	–	–	2.0	–	–	–	–	8.2	6.2	4.1	208.4	5.93 (7.36)	–	–	12.7	8.7 (9.8)	Gneissic boulder oriented with long axis parallel to flow direction.
7–8–24	4.0	–	–	–	64.0	–	–	–	–	–	–	–	–	–	–	–	–	Newly constructed channel with cross-sectional area of 238 m².
7–8–25	4.0	–	–	0.4	–	0.1	–	1.0	–	–	–	–	–	–	–	–	–	Fluvial deposition.
7–8–26	–	–	–	–	72.0	–	–	–	–	–	–	–	–	–	–	–	–	Newly constructed channel with cross-sectional area of 261 m².
7–8–27	–	2.3	–	1.6	–	–	–	0.2	–	–	–	–	–	–	–	–	–	Fluvial deposition(?).
7–8–28	4.5	–	–	1.9	–	–	–	0.4	–	–	–	–	–	–	–	–	–	Fine-grained deposition of fluvial origin(?).
7–8–29	2.5–3.0	2.0	–	–	–	–	–	1.4	–	–	–	–	–	–	–	–	–	–
7–8–30	3.5–8.0	–	–	3.0	–	–	–	1.2–1.5	–	–	–	–	–	–	–	–	–	Small boulders deposited on roof of one-story building.
7–8–31	4.5	0.8–1.5	–	–	–	–	–	–	2.3	1.7	1.6	6.3	1.84 (2.29)	–	–	6.7	5.0 (5.5)	Gneissic boulder.
7–8–32	4.5	1.8	–	1.8	–	–	–	2.1	2.8	1.8	1.0	5.0	1.71 (2.13)	–	–	6.9	4.8 (5.3)	–
7–8–33	4.5	–	–	2.0	–	–	1.0	–	–	–	–	–	–	–	–	–	–	–
7–8–34	3.0–4.0	–	–	1.8	–	–	–	1.0	–	–	–	–	–	–	–	–	–	–
7–8–35	3.5–4.0	–	–	3.0	–	–	–	–	3.2	2.2	1.7	12.0	2.29 (2.84)	–	–	7.8	5.5 (6.1)	Gneissic boulder; boulder garden in front yard of house.
7–8–36	4.5–5.0	2.3	–	1.8	–	–	–	1.3–1.5	–	–	–	–	–	–	–	–	–	–
7–8–37	–	1.7–1.8	–	1.3	–	–	–	1.0	–	–	–	–	–	–	–	–	–	–
7–8–38	5.0–7.5	0.6	–	–	–	–	–	–	–	–	–	–	–	–	–	–	–	Flood deposition with a few small boulders; eyewitness reported flow of mostly muddy water with a few boulders.
7–10–1	5.0	3.5	–	3.5	172.0	–	–	–	3.1	2.8	1.0	8.1	2.01 (2.49)	–	–	8.3	5.2 (5.7)	Gneissic boulder.
7–10–1	–	–	–	–	–	–	–	–	3.8	3.0	1.2	13.0	–	–	–	–	–	–
7–10–2	3.0–3.5	–	–	1.7	181.0	–	–	2.5	–	–	–	–	–	–	–	–	–	–
7–10–2	3.0–3.5	–	–	7.0	–	–	–	0.5	–	–	–	–	–	–	–	–	–	Sequence of three old debris-flow deposits with combined thickness of 7 m capped by new deposits.
7–12–1	3.0	2.0	–	1.5	–	–	–	–	1.5	1.2	0.9	1.6	1.17 (1.48)	–	–	5.7	4.0 (4.4)	Round boulder punched through two walls of house; house stopped most of debris flow.
7–12–2	3.0–3.5	1.5	–	–	–	–	–	–	1.8	1.3	0.8	1.4	1.12 (1.40)	–	–	5.9	3.9 (4.4)	–
7–12–3	2.5	2.5	–	–	36.0	–	–	–	2.0	1.5	0.5	1.5	1.14 (1.41)	–	–	6.3	3.9 (4.4)	Extension of street used as channel by flow.
7–12–4	3.0	1.9	–	1.9	–	–	–	1.5–2.0	3.0	2.2	1.9	12.5	2.32 (2.88)	–	–	7.8	5.5 (6.1)	Very thin, coarse-grained, sandy matrix with boulder to boulder contact.
7–12–4	–	–	–	–	–	–	–	–	2.7	2.0	1.9	10.3	2.17 (2.70)	–	–	7.3	5.4 (5.9)	–
7–12–5	4.0–4.5	–	–	–	64.0	–	–	–	4.8	2.4	1.5	16.6	2.55 (3.16)	–	–	8.0	5.8 (6.4)	–

Map no.	Slope, in degrees	Flow depth		Deposit thickness, in m	Channel width, in m	Boulder size, in m			Maximum boulder size, in m					Superelevation		Flow velocity, in m/s		Comments
		left, in m	right, in m			50%	75%	90%	A axis	B axis	C axis	Volume, in m^3	Nom. diam. cube (sphere)	In degrees	velocity, in m/s	Costa, 1983	Clarke, 1996 cube (sphere)	
San Juñón (Carabalieda fan)—Continued																		
7–12–6	6.0	1.8	—	—	—	—	—	—	3.1	2.4	1.7	12.6	2.33 (2.89)	—	—	8.0	5.5 (6.1)	Thickness of deposits decreased as flow moved between houses; some boulders have likely been subsequently removed from streets.
7–12–7	3.5–4.0	1.8	—	0.8	—	—	—	—	—	—	—	—	—	—	—	—	—	Fine-grained deposition along street.
7–12–8	3.0	1.5	—	—	—	—	—	—	2.0	1.2	0.9	2.2	1.29 (1.80)	—	—	5.7	4.2 (4.6)	—
7–12–9	2.5–3.5	1.4	—	—	—	—	—	—	3.2	3.0	2.8	26.9	3.00 (3.72)	—	—	8.9	6.2 (6.9)	Round boulder.
7–12–10	3.5	2.0	—	1.5–2.0	—	—	—	—	2.0	2.0	1.2	4.8	1.69 (2.10)	—	—	7.3	4.7 (5.3)	Boulders supported by matrix.
7–12–11	2.5	2.5	—	1.7	20.0	—	—	—	—	—	—	—	—	—	—	—	—	—
7–12–12	2.5–3.0	—	—	—	37.0	—	—	—	—	—	—	—	—	—	—	—	—	Minimal amount of flow over bridge, but apparently flow filled channel.
7–12–13	3.0	1.7	—	1.2–1.4	—	—	—	—	1.0	0.9	0.7	0.8	0.84 (1.04)	—	—	4.9	3.4 (3.8)	0.7-m-thick, fine-grained fluvial(?) deposit over 1.7-m-thick bouldery, debris-flow deposit.
7–12–14	2.5	—	—	1.8	—	—	—	—	—	—	—	—	—	—	—	—	—	Uniform coarse-grained, sandy deposit.
7–12–15	2.5	1.8	—	1.2	—	—	—	—	—	—	—	—	—	—	—	—	—	All deposits have been removed subsequent to event.
7–12–16	—	—	—	0.7–0.9	—	—	—	—	—	—	—	—	—	—	—	—	—	Deposits decreasing in thickness along length of side street.
7–12–17	1.0–1.5	1.8	—	0.9–1.4	—	—	—	—	—	—	—	—	—	—	—	—	—	Only fine-grained deposits.
7–12–18	1.0	1.0	—	1.0	—	—	—	—	—	—	—	—	—	—	—	—	—	Only fine-grained deposits.
7–12–19	—	—	—	—	—	—	—	1.5–2.0	—	—	—	—	—	—	—	—	—	—
7–12–20	3.0–3.5	1.1	—	0.5	—	—	—	0.5	—	—	—	—	—	—	—	—	—	—
7–12–21	3.0	0.5–1.0	—	0.5–1.0	—	—	—	—	—	—	—	—	—	—	—	—	—	—
7–12–22	—	0.8	—	0.8	—	—	—	—	1.6	1.3	0.8	1.6	1.17 (1.45)	—	—	5.8	4.0 (4.4)	—
7–12–23	4.5	0.2–0.3	—	0.2–0.3	—	—	—	—	—	—	—	—	—	—	—	—	—	Only fine-grained deposits.
7–12–24	3.0–5.0	—	—	0.5	—	—	—	—	—	—	—	—	—	—	—	—	—	Only fine-grained, sandy deposits.
7–12–25	3.0–3.5	1.2–1.5	—	0.8–1.5	71.0	—	—	—	—	—	—	—	—	—	—	—	—	—
7–12–26	3.5	1.0	—	0.4–0.5	—	—	—	—	—	—	—	—	—	—	—	—	—	Sandy deposits.
7–12–27	2.5	—	—	0.8	—	—	—	0.2	—	—	—	—	—	—	—	—	—	Mostly fine-grained deposits.
7–12–28	2.0	0.8–1.1	—	—	—	—	—	1.2	—	—	—	—	—	—	—	—	—	Drilling showed 4.5-m-thick old debris-flow deposits with boulders; only fine-grained deposition in recent deposits at this location.
7–12–29	4.5–5.0	1.1	—	1.0	—	—	—	—	1.3	1.3	0.8	1.4	1.11 (1.37)	—	—	5.9	3.9 (4.3)	Boulders traveled down street which acted like a channel; deposits of imbricated boulders.
7–12–29	—	—	—	—	—	—	—	—	0.9	0.8	0.8	0.5	0.82 (1.01)	—	—	4.7	3.4 (3.7)	—
7–12–30	4.0	1.2	—	0.8	—	—	—	<0.5	1.9	0.8	0.8	1.2	1.07 (1.32)	—	—	4.7	3.8 (4.2)	—
7–12–31	3.5	2.5	—	1.5	—	—	—	—	1.5	0.8	0.7	0.8	0.94 (1.17)	—	—	4.7	3.8 (4.0)	—
7–12–32	3.0–3.5	0.7	—	0.3	—	—	—	—	—	—	—	—	—	—	—	—	—	—
7–12–33	5.0–8.0	—	—	—	—	0.99	—	—	3.8	2.8	1.6	16.1	2.53 (3.13)	—	—	—	—	—

VITA

CORA E. MARTINEZ FRANKLIN

September 19, 1968	Born, Caracas, Venezuela
1991	Mechanical Engineer Universidad Simon Bolivar Caracas, Venezuela
1991-1994	Universidad Simon Bolivar Instructor
1997	M.S., Mechanical Engineering Massachusetts Institute of Technology Boston, Massachusetts
1997- 2004	Universidad Simon Bolivar Assistant Professor
2004-2005	University of Miami Teaching Assistant
2005-2009	Florida International University Teaching Assistant
2009	PhD Candidate, Civil Engineering Florida International University Miami, Florida

PUBLICATIONS AND PRESENTATIONS

Martínez Cora, Goncalves Raúl (2003). *Laying Modeling of Submarine Pipelines using Contact Elements into a Co-rotational Formulation*. Journal of Offshore Mechanics and Artic Engineering. 125:145-152.

Villarraga Junes, Rodriguez José Félix, Martínez, Cora (2004). *Buried Pipe Modeling with Initial Imperfections.* Journal of Pressure Vessel Technology. 126:250-257.

Martinez, C., F.Miralles-Wilhem and R. Garcia-Martinez, (2007). *A 2D finite element debris flow model based on the cross rheology formulation*. Fourth International Conference on Debris-Flow Hazards Mitigation: Mechanics, Chendu, China.

Martinez, C., Miralles-Wilhelm, F. & Garcia, R. (2008). *Verification of a 2D finite element debris flow model using Bingham and Cross rheological formulations*. Debris Flows 2008. Wessex Institute, Ashurst, UK (Invited paper).